Spin-Orbit Coupling, Entanglement, and Topological Structures of the g-Tensor of Crystalline Materials for Spin Qubits

Von der Fakultät für Mathematik, Informatik und Naturwissenschaften der RWTH Aachen University zur Erlangung des akademischen Grades einer Doktorin der Naturwissenschaften genehmigte Dissertation

vorgelegt von

Mira Ramakant Sharma, M.Sc.

aus

Mumbai, Indien

Berichter: Univ.-Prof. i. R. Dr. David Peter Di Vincenzo
Univ.-Prof. Dr. Fabian Hassler

Tag der mündlichen Prüfung: 10.07.2025

This thesis and the work done during this PhD is an offering to the Mother and Sri Aurobindo.
You will always be my guiding light.

Preface

Quantum computing emerged at the intersection of classical computing and quantum mechanics. While Alan Turing laid the foundations for programmable machines in 1936, it was the invention of transistors in 1947 that got computers into our daily lives. In the 1960s, Gordon Moorepredicted that the computational power will double every year for a constant cost. But as the electronics got smaller and smaller, quantum effects began to hinder this progress. To efficiently simulate a quantum process, Richard Feynman proposed using machines that follow the rules of quantum mechanics. David Deutsch formalized the concept of a universal quantum computer. In 1994, Peter Shor developed an algorithm capable of factoring large numbers exponentially faster than classical system. Since then, quantum computing has evolved from theory into a rapidly advancing field, with quantum processors now being developed by leading research institutions and technology companies. This year, nearly a century after Turing's foundational work, we celebrate the International Year of Quantum Science and Technology.

The search for the best quantum computing platform has lead to numerous candidates among which semiconductor spin qubits stand out for their scalability and coherence times. These spins are governed by spin-orbit interaction (SOI) that can be used to manipulate them. The SOI could also turn out to be detrimental for coherence effects. The g-factor is an important quantity which gives us a direct access to the SOI. In this thesis we provide a general introduction to quantum computing in chapter 1. Chapter 2 establishes the basics of semiconductor physics and some crucial concepts of group theory following closely the books 'Fundamentals of Semiconductors' by Yu and Cardona, 'Group Theory and its Applications in Physics' by Inui and 'Group Theory: Application to the Physics of Condensed Matter' by Dresselhaus. Chapter 3 explains the details of semiconductor spin qubit architectures and follows the lecture notes of the Spin Qubit Platforms by University of Basel.

The rest of the thesis is based entirely on the work done during this PhD and summarizes the main results obtained during the course. In chapter 4, we present a theoretical framework for the g-factor which is in fact a tensorial quantity. We show topological effects in bulk groups IV/III-IV semiconductors such as silicon, germanium, gallium-arsenide which are guaranteed by the underlying symmetry in a larger class of materials. Chapter 5 illustrates the figures showing these topological effects. Both chapters 4 and 5 are based on the publication - g-factor symmetry and topology in semiconductor and band states - that resulted from this work. Chapter 6 delves deeper into the orbital effects and illustrates where they come from.

Acknowledgements

"It would not be much of a universe if it wasn't home to the people you love."
– Stephen Hawkings, *A Brief History of Time*

I am grateful to a lot of people who have helped me reach where I am today.

I would like to begin by thanking my supervisor, David DiVincenzo, for giving me this opportunity to learn from you. You represent a Doktorvater in the true sense of the word. You have taught me so many things apart from just science. I admire your wisdom on various facets of life. You have taught me how to be patient and shown me that even negative results hold meaningful lessons. Your encouragement kept me going. I have immense respect for you. I hope that I have imbibed your approach to science and to life in general and that I am able to develop that and carry it further into the future. I would like to thank my second supervisor, Fabian Hassler, for meaningful discussions and for being someone I could approach in David's absence. Your opinions on the different topics that we all discussed in the 'coffee hour' after lunch were always so fascinating.

Through my stay at IQI, some people were there with me for a short while and some others were there throughout. When I first arrived, I met Martin Rymarz, Evangelos Vervelis and Lisa Otten who were around the most post Covid. I would like to thank you all for making me feel comfortable in the new environment. Lorenzo Cardarelli, thank you for making me laugh from day one. Helene Barton also played a big role in taking the bureaucratic workload completely off me. I would also like to thank Uwe Kahlert who helped me with the technical difficulties from the start to te end. Anand Sharma, you were among the first people I met. You always had the support and the advice I needed not only while you were in Aachen but also after you left. I am so grateful for that.

Sascha Heussen, thank you for sharing your PhD experience with me and making me feel like I am not alone. I want to say a very special thanks to David Locher and Lukas Bödekar, the two people who always helped me no matter what. I appreciate that you guys were never bothered by my numerous interrupting knocks on your office door. Lukas and Friedrike Butt, thanks for making sure that I was aware of the Thirsty Thursday events. I loved to hangout with you all.

I want to thank Thiago Lucena Macedo Guedes for sharing his experience as an outsider with me, made me feel less crazy about my experiences. Josias Old, thank you for helping with the German translation of the abstract and for patiently helping me with the visa stuff.Konstantinos, you made us all laugh so often during the 'coffee hours'. I appreciate the 'how are you?' and the brief updates every morning since we were always the first people around. I want to thank Luis Colmenarez, David Scheer, Julius Zeiss, Berat Yenilen, Katerine Bolsmann, Sreejith Sreekumar, Markus Müller, Mario Berta and all the other members of IQI for being such amazing colleagues!

Roshni Singh, you were my first temporary office-mate and I learnt a lot from you. Even though you were around for a very short while, you didn't make it feel that way. I am glad that with Ishan Mankodia and Krish Ramesh I got to experience new sides of Aachen. Krish, thank you for listening patiently to my complaints throughout the years that I have known you. I am grateful to Sergei Blinov and Sajag Kumar for making the depressing, rainy summer of 2024 so much fun. Sergei, I am so glad that I got you hooked on to Malabar, at least you have something to miss from Aachen all your life. Nick Hartmann and Áron Márton, you guys are the office-mates that stayed the longest. I am almost upset that I have to leave before you guys do. Thank you both for making 114 a fun place to work in. Nick, I appreciate you not getting annoyed with me disturbing you with the German documents. Áron, thanks for helping me with the digital mouse-crises near the end.

I would like to thank Professor Rajib Rahman and especially Abu Mohammad Saffat-Ee Huq for spending so much time in helping me understand NEMO-3D. I am also grateful to have known Arnau Sala Cadellans, Malte Neul, Max Beer, Isabelle Sprave, Denny Dütz, Lukas Marcogliese. You guys were so much fun to hangout with. Arnau, thank you for being so encouraging. Mats Volmer, you will not be forgotten especially after we got the Dutch train to bring just the two of us back to the station. Spandan Anupam, thanks for listening to me vent from time to time. I am immensely grateful for your support with the bureaucratic visa process. I hope I can return the favor some time.

Thank you Christian Dickel and Marian Barsoum for making me a part of the ML4Q&A podcast. I enjoyed every moment of it. Marian, your encouragement never failed. Chris, I have a lot to be grateful for to you. You have influenced me in a lot of positive ways. I wish I had more time to learn more from you. Sagnik Ghosh, Maxime Debertolis, Julien Bréhier, Santhosh Surendra, Daniel Roschenbach, Torsten Röper, Luc Janssen, some of the other friends I made through ML4Q who have contributed to the lively times through my PhD, thank you all.

I met some amazing people outside of IQI. Evadokia (Evita) Stefanopoulou, I can't thank you enough! I will always remember the crazy weekends we spent together, trying the weirdest things past midnight, our travels, our love for tea and shows. I loved exploring new places in

and around Aachen with you. Being around you always lightened the mood. Even though we come from different cultures, we had so much in common, which is why you understood me the best. I thank you also for introducing me to Alex and Alan. I always looked forward to meeting them. Tejhas Kapoor, I am glad to have known you as a friend. You taught me a lot on how to live life.

I would like to thank my seniors Pritam Pai and Saptarshi Kotal for sharing their experiences of pursuing PhD abroad. Thanks Sap for making even some daunting tasks seem easy. I could always rely on you whenever I needed an outlet.

I would like to thank Nibal Khudeish for her support. I would like to thank Vittorio Vitale, Alice Pagano, Elena Poli and all the people that I met in the past five years starting from my masters to the different conferences, workshops, schools and other events that I attended. I learnt a lot from each one, even though the meeting was brief.

Michele di, je vous suis éternellement reconnaissante pour votre soutien depuis que je vous connais. Vous avez fait plus pour moi que je n'aurais pu l'espérer. Vous n'avez jamais manqué de m'aider quand j'en avais vraiment besoin.

The people I want to thank the most are my parents. Thanks for always being so supportive. Thank you for encouraging me to follow my interests and my passion. Thank you for always guiding me on the right path. Thank you Papa for always reminding me to smile. Thank you Mom for making me as dedicated as you are. I would also like to thank Maa (my grandma) for passing on the determination in the DNA. Chachaji, Prasanna, thank you so much for believing in me. My brothers Arjun, Kedar and Hari have always shown their support in very different ways. I am grateful to have you three in my life. All of you have always encouraged me to keep going ahead in life and held my hand through the dips and falls. There is nothing more I could have asked me.

"Last but not the least, I wanna thank me. I wanna thank me for believing in me. I wanna thank me for doing this hardwork... I wanna thank me for never quitting" - Snoop Dogg.

Contents

"The task is... not so much to see what no one has yet seen; but to think what nobody has yet thought, about that which everybody sees."

– Schrödinger, *"What Is Life?" (1944)*

1 Quantum Computing

1.1 Introduction

Quantum computing is an emerging field that applies the principles of quantum mechanics to perform difficult computation. It exploits the quantum phenomena of superposition and entanglement to process information in new ways, offering exponential speedups for certain computational tasks. A variety of physical platforms - from superconducting circuits and trapped ions to topological qubits - are being developed to realize these machines, each presenting its own unique advantages and challenges. This chapter introduces the foundational concepts, mathematical framework, and physical architectures that have shaped the rapid development of quantum computing.

1.2 Qubits

Analogous to a classical bit, the fundamental unit of quantum information is the quantum bit, or *qubit*. Unlike a classical bit which can be in only one of two states (0 or 1), a qubit can exist in a linear superposition of the basis states $|0\rangle$ and $|1\rangle$:

$$|\psi\rangle = \alpha\,|0\rangle + \beta\,|1\rangle\,, \tag{1.1}$$

where α and β are complex probability amplitudes satisfying $|\alpha|^2 + |\beta|^2 = 1$. These squared magnitudes represent the probabilities of measuring the qubit in state $|0\rangle$ or $|1\rangle$, respectively. The basis states are orthogonal and correspond to the two levels of a physical quantum system. We

can also define these states on a Bloch sphere,

$$|\psi\rangle = e^{i\gamma}\left(\cos\left(\frac{\theta}{2}\right)|0\rangle + e^{i\phi}\sin\left(\frac{\theta}{2}\right)|1\rangle\right) \tag{1.2}$$

with θ and ϕ are the polar and the azimuthal angles of the vector representing the state. The state $|0\rangle$ is shown in fig.1.1. Eq.1.1 shows a single qubit state. For a system with multiple qubits,

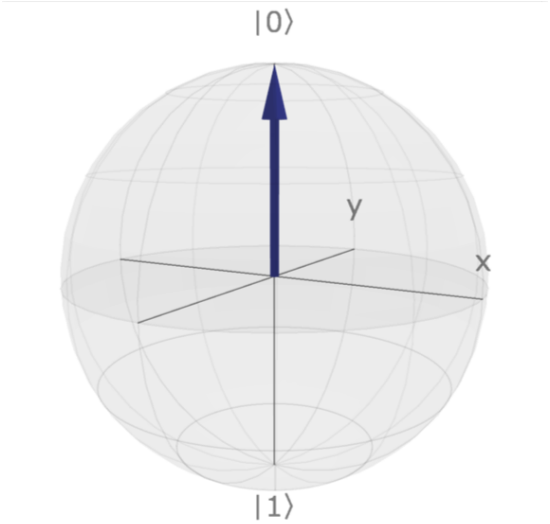

Figure 1.1: The Bloch sphere representation of the state $|0\rangle$. This corresponds to $\theta = 0$. The basis states $|0\rangle$ and $|1\rangle$ lie on the poles of the Bloch sphere. The image was created using a Bloch sphere simulator [1].

the state space is a tensor product of the individual qubit state spaces, $\mathcal{H}_n = \mathrm{C}^{2n}$. For n = 2, $|\psi\rangle = \frac{1}{\sqrt{2}}(|0_1\rangle|0_2\rangle + |1_1\rangle|1_2\rangle) = \frac{1}{\sqrt{2}}(|00\rangle + |11\rangle)$.

The quantum states can also be represented in a matrix form, $\rho = |\psi\rangle\langle\psi|$ such that $\mathrm{Tr}\,\rho = 1$. This is particularly useful for states that are mixtures of pure states. A mixed state can be identified as $\mathrm{Tr}\,\rho^2 < 1$. When two subsystems A and B make up the composite system AB described by the density matrix $\rho_{AB} = \rho_A \otimes \rho_B$, we can find the density matrices of each of the subsystem by partially tracing out the other, $\mathrm{Tr}_B\,\rho_{AB} = \rho_A$ or $\mathrm{Tr}_A\,\rho_{AB} = \rho_B$.

States that cannot be described independently of one another are said to be entangled. Entanglement is an exclusive feature of quantum mechanics. One way to measure the degree of entanglement of a single qubit is using the von Neumann entropy, $S(\rho) = \mathrm{Tr}\,(\rho\log_2(\rho))$. Entanglement in two-qubit and three-qubit systems is quantified using concurrence and tangle, respectively. However, we will not delve into these measures in detail here.

1.3 Quantum Gates and circuits

Quantum gates are the fundamental building blocks of quantum circuits, analogous to classical logic gates but they operate under the principles of quantum mechanics. They manipulate quantum states through unitary operations, as a result they are reversible. Quantum gates can act on one, two, or more qubits, allowing for operations such as superposition, entanglement, and interference. In what follows, we introduce the basic single-, two-, and three-qubit gates that form the basis of quantum computation.

1.3.1 Single qubit gate

Gates can be applied on a single qubit which amount to a rotation of the state. The most common single qubit gates are:

- The X gate, or the NOT gate which rotates the state around the x-axis, $X|0\rangle = |1\rangle$.
- The Y gate is a rotation by π around the y-axis. $Y\left(\frac{1}{\sqrt{2}}(|0\rangle + |1\rangle)\right) = \frac{i}{\sqrt{2}}(|0\rangle - |1\rangle)$.
- The Z gate which rotates the state by π around the z-axis such that, $Z|1\rangle = -|1\rangle$.
- The phase shift gate $P(\phi)$ modifies the phase of a quantum state, $P(\phi)|1\rangle = e^{i\phi}|1\rangle$. Some specific examples of the phase shift gates are the $S = P(\pi/2)$ and $T = P(\pi/4)$ gates.
- An important gate to bring a state in and out of superposition is the Hadamard gate, $H(H|0\rangle) = H\left(\frac{1}{\sqrt{2}}(|0\rangle + |1\rangle)\right) = |0\rangle$. It can be summarized as a rotation around by $\pi/2$ the y-axis followed by a rotation by π around an x-axis.

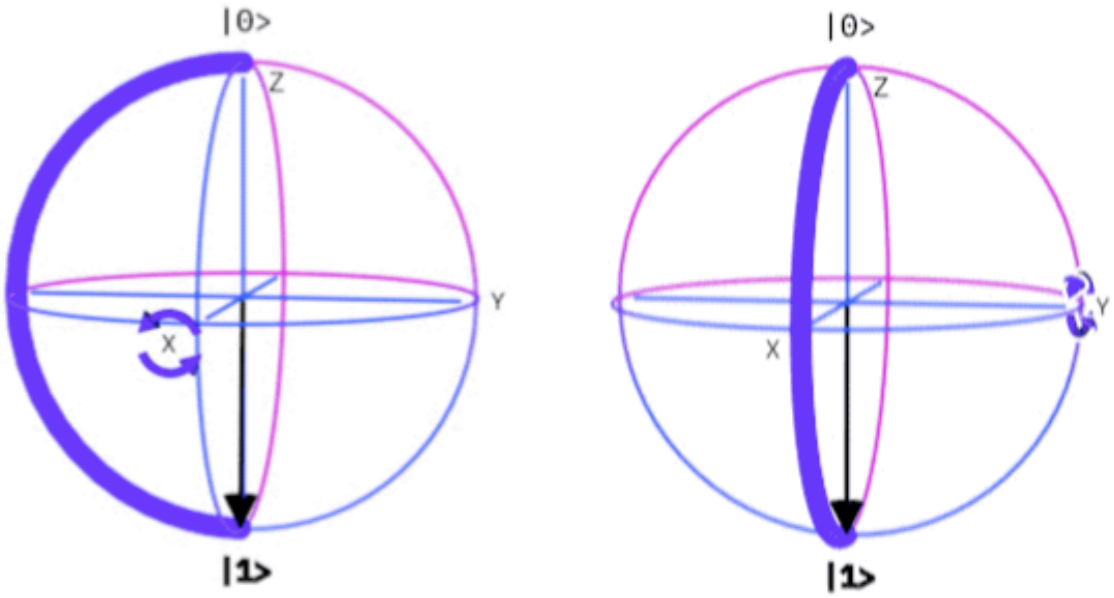

Figure 1.2: The X and Y gate actions on the state $|0\rangle$ along the Bloch sphere (image from [2]).

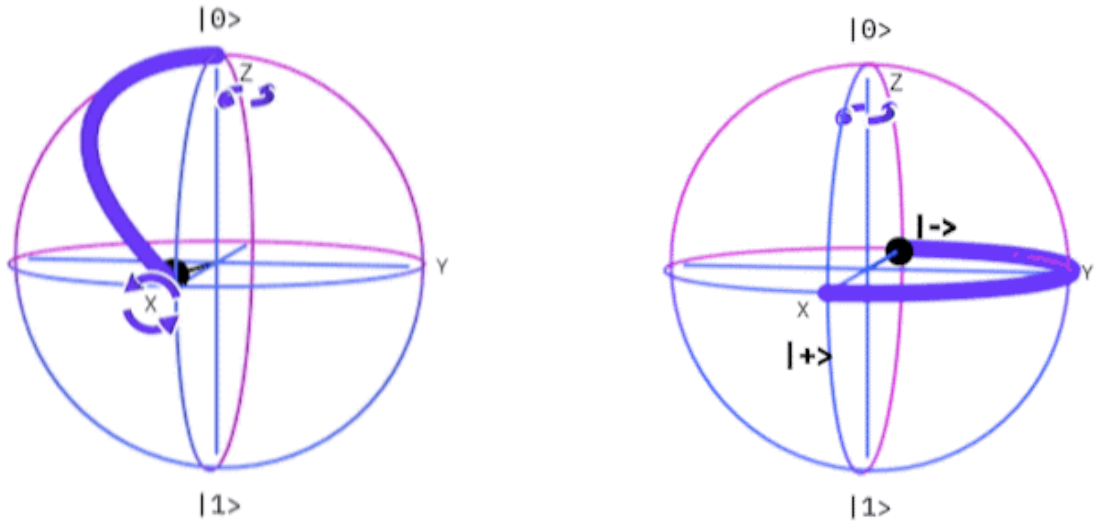

Figure 1.3: The Z and H gate actions on the state $|0\rangle$ along the Bloch sphere (image from [2]).

1.3.2 Two qubit gates

It is not enough to rotate the qubits around the Bloch sphere. To perform useful computation they must also interact. The commonly used two qubit gates are:

- The controlled-NOT gate or the CX gate performs a NOT operation on the second qubit when the first qubit is in the state $|1\rangle$, $CNOT\,|10\rangle = |11\rangle$. The first qubit acts as a control. The CNOT gate creates entanglement between the two states. Consider the control qubit to be in a superposition and the target qubit to be in the 0 state, $|\psi\rangle = \frac{1}{\sqrt{2}}\left(|0_c 0_t\rangle + |1_c 0_t\rangle\right) = \frac{1}{\sqrt{2}}\left(|00\rangle + |10\rangle\right)$, after applying CNOT we get a maximally entangled state also known as a Bell-pair, $CNOT\,|\psi\rangle = \frac{1}{\sqrt{2}}\left(|00\rangle + |11\rangle\right)$.
- The controlled-Z gate or the CZ gate performs a z-rotation on the second qubit when the first qubit is $|1\rangle$, $CZ\,|11\rangle = -\,|11\rangle$.
- The SWAP gate is also an important gate which swaps two qubits, $SWAP\,|10\rangle = |01\rangle$.

1.3.3 Three qubit gates

The quantum Toffoli gate or the CCNOT gate acts as a NOT gate on the third qubit only if the first and the second qubits are in $|1\rangle$ state, $CCNOT\,|110\rangle = |111\rangle$.

A universal gate set consists of quantum gates from which any quantum operation can be constructed. Some commonly used examples of such universal gate sets include,

- The rotations $R_x(\theta), R_y(\theta), R_z(\theta)$, phase shift $P(\phi)$ and $CNOT$.
- The Clifford set of gate + T gate.

- The Toffoli gate + the Hadamard gate.

1.4 Quantum algorithms

A quantum algorithm is a step-by-step computational procedure executed on a quantum computer that uses fundamental quantum phenomena such as superposition and entanglement. These algorithms are typically represented using quantum circuits composed of qubits and quantum gates. Quantum algorithms can be categorized based on the techniques they employ - such as quantum phase estimation, the quantum Fourier transform, quantum walks, or amplitude amplification - or by the classes of problems they aim to solve [3].

The Deustch-Jorzsa algorithm [4] is one of the earliest known quantum algorithm that demonstrates a quantum speed-up [5]. The algorithm address the problem of determining whether a function is constant e.g. for all inputs the function outputs either 0 or 1, or it is balanced i.e half of the inputs are mapped onto 1 and the other half are mapped onto 0. A classical algorithm would require 2^n evaluations for an n-bit function to determine whether it is constant or balanced while the Deutsch-Jorzsa predicts with only one evaluation.

Another example of a quantum algorithm is Shor's algorithm [6] which finds the prime factors of a composite number in polynomial time. It uses a technique called quantum Fourier transform to find the period of a function which, along with other steps, leads to the factorization of the number. It is also one of the earliest examples of computational advantage.

Grover's algorithm [7] searches a database with N entries using only $\mathcal{O}\left(\sqrt{N}\right)$ queries as opposed to $\mathcal{O}\left(N\right)$ that a classical algorithm requires. This algorithm uses amplitude amplification.

1.5 Decoherence

One of the primary challenges in building practical quantum computers is decoherence. It refers to the process by which a quantum system loses its quantum behavior due to interactions with its surrounding environment. It marks the transition from a coherent quantum state to a classical probabilistic mixture destroying the quantum information. There are two typical mechanisms through which decoherence affects the qubits: relaxation and dephasing. Both of these processes are irreversible unlike quantum gate operations.

1.5.1 Dephasing

Dephasing is a process in which a system loses its quantum coherence to the environment. The qubit loses its ability to be in a state of superposition. The characteristic time scale for decoherence

is T_2.

1.5.2 Relaxation

The process by which the qubit spontaneously relaxes from an excited state $|1\rangle$ to the ground state $|0\rangle$ losing energy to the environment. The characteristic time to do so is called T_1 time.

1.6 The DiVincenzo criteria

Before examining the physical implementations of quantum computing, it's important to understand the criteria that a physical device must satisfy. These criteria were outlined by David DiVincenzo in 1996 [8]. DiVincenzo summarized five key conditions for the quantum computer itself, as well as two additional conditions for the implementation of quantum communication, which are as follows (sr. Wikipedia):

1. *A scalable physical system with well characterized qubits*.
2. *The ability to initialize the state of the qubits to a simple fiducial state*.
3. *Long relevant quantum coherence times*.
4. *A "universal" set of quantum gates*.
5. *A reliable measurement capability*.

The other two conditions are:

1. *The ability to interconvert stationary and flying qubits*.
2. *The ability to faithfully transmit flying qubits between specified locations*.

The DiVincenzo criteria provide a comprehensive framework for evaluating whether a system can be a candidate for quantum computing. Meeting these conditions is essential for building reliable quantum computers that can perform meaningful computations on larger scales. While significant progress has been made in implementing these criteria, challenges remain in realizing them in practical applications.

1.7 Physical models

We have come a long way from conceptualising to realising quantum computers. In this section we mention briefly the popular candidates for quantum computation.

1.7.1 Superconducting qubits

In a superconducting quantum computer, the most popular type of qubit is a transmon [9], a Josephson junction in parallel with a capacitance and a current-bias. This acts as an anharmonic oscillator creating a two level system that can be controlled with microwave pulses. The operating temperatures of a transmon are between 10 to 20 mK. Highest achieved T_1 relaxation time is 0.95 ms and T_2 dephasing time is 1.15 ms [10]. The gate execution times for superconducting qubits is tens of nanoseconds. The fast gate operation times make them an attractable platform. This is the architecture adopted by companies like Google, IBM, Rigetti.

1.7.2 Trapped ion quantum computing

There are two predominant ways to form qubits out of trapped ions (usually Ca^+ or Yb^+): a system of two groundstate hyperfine levels; or a system of a ground and an excited states [11]. These are controlled by lasers and operate at micro-Kelvin temperatures. Coherence times for trapped ions can be in the order of a few minutes. But the gates times are slower, they are between a few μs to a few ms. Trapped ions have very high gate fidelities and long coherence times but their gates are slow and scaling a trapped ion system is non-trivial. Companies such as IonQ, Quantinuum and Alpine Quantum Technologies are developing such architectures.

1.7.3 Semiconductor quantum computing

Another way to encode quantum information is using electron/hole spins in semiconductors. These are controlled by microwaves and voltage pulses and operator between 10 and 100 mK. The highest recorded T_1 times are 6.3s and highest recorded spin dephasing times T_2 are 803μs [12]. The gate operation times are about 10-100 ns. Some of the biggest advantages of this system is the potential scalability into CMOS technology which has been advanced to a high level now, and also the long coherence times. Some of the biggest challenges that this architecture faces is bottleneck of control electronics and coupling qubits over larger distances. Intel, along with other start-ups such as Diraq and Quobly are pushing to make it the leading path to quantum computing.

1.7.4 Neutral atom quantum computing

A neutral atom quantum computer is built out of Rydberg states of neutral atoms which are controlled by lasers and optical tweezers. These operate at micro-Kelvin temperatures. Both the T_1 and T_2 times for neutral atoms are in the order of seconds [13]. Neutral atom platforms exhibit a flexible geometry, high connectivity and good gate fidelities. Some of the key challenges faced by this platform are atom loss and the effect of laser noise. Despite these hurdles, companies like QuEra and Cold Quanta are actively pursuing this promising architecture for quantum computing.

1.7.5 Photonic quantum computing

Two level systems formed by the polarization or by the path-encoding of a photon are used as qubits in a photonic quantum computing platform [14]. These can be controlled with linear optics and single-photon detectors. Such qubits operate at room temperatures. The coherence times for photons are long enough not only for computation but also for communication. Photons are easily transmissible and one need not worry about decoherence with them. Photonic quantum computing has an advantage when it comes to integration of quantum communication with quantum computing. Photons can be lost easily and it is hard to build two-qubit gate operations. This architecture has been adopted by companies like Xanadu, PsiQauntum, QuiX.

1.7.6 Topological qubits

Yet another platform which is robust to noise through topology is topological quantum computing which utilizes Majorana zero modes as qubits. This field is still in early stages of research, much remains to be still explored and understood.

1.8 Conclusion

This chapter has provided a brief overview of the current state of quantum computing. Significant progress has been made over the past two decades for each of the quantum computing platforms mentioned earlier. This thesis will focus primarily on semiconductor spin qubits. Other important characteristics, such as qubit and gate fidelities, and measurement times, have been intentionally skipped from this discussion. The following chapters provide a detailed introduction to semiconductors (chapter 2) and spin qubits (chapter 3) which will prepare the reader for the main topic of the thesis which is the g-factors that proves to be an important variable when it comes to manipulation of electron/holes spins.

Bibliography

[1] Konstantin and YDX. Bloch sphere simulator, 2022. URL https://bloch.kherb.io. an online sumlation tool that allows to study an SU2 representation of a qubit and its roations.

[2] IBM. Learning quantum. URL https://lewisla.gitbook.io/learning-quantum/quantum-circuits/single-qubit-gates. IBM Qiskit website discussing the Bloch sphere and gate application.

[3] Andrew M. Childs and Wim van Dam. Quantum algorithms for algebraic problems. *Rev. Mod. Phys.*, 82:1–52, Jan 2010. doi: 10.1103/RevModPhys.82.1. URL https://link.aps.org/doi/10.1103/RevModPhys.82.1.

[4] David Deutsch and Richard Jozsa. Rapid solution of problems by quantum computation. *Proceedings of the Royal Society of London. Series A: Mathematical and Physical Sciences*, 439(1907): 553–558, 1992. URL https://royalsocietypublishing.org/doi/10.1098/rspa.1992.0167.

[5] D.R. Simon. On the power of quantum computation. In *Proceedings 35th Annual Symposium on Foundations of Computer Science*, pages 116–123, 1994. doi: 10.1109/SFCS.1994.365701.

[6] Peter W. Shor. Polynomial-time algorithms for prime factorization and discrete logarithms on a quantum computer. *SIAM Journal on Computing*, 26(5):1484–1509, 1997. doi: 10.1137/S0097539795293172. URL https://doi.org/10.1137/S0097539795293172.

[7] Lov K. Grover. A fast quantum mechanical algorithm for database search, 1996. URL https://arxiv.org/abs/quant-ph/9605043.

[8] David P. DiVincenzo. Topics in quantum computers, 1996. URL https://arxiv.org/abs/cond-mat/9612126.

[9] Jens Koch, Terri M. Yu, Jay Gambetta, A. A. Houck, D. I. Schuster, J. Majer, Alexandre Blais, M. H. Devoret, S. M. Girvin, and R. J. Schoelkopf. Charge-insensitive qubit design derived from the cooper pair box. *Phys. Rev. A*, 76:042319, Oct 2007. doi: 10.1103/PhysRevA.76.042319. URL https://link.aps.org/doi/10.1103/PhysRevA.76.042319.

[10] IQM. Iqm benchmarks, 2024. URL https://www.hpcwire.com/off-the-wire/iqm-quantum-computers-advances-quantum-processor-quality-with-new-benchmarks/.

[11] DJ Wineland, C Monroe, WM Itano, D Leibfried, BE King, and DM Meekhof. Experimental issues in coherent quantum-state manipulation of trapped atomic ions. *J Res Natl Inst Stand Technol.*, 103(3):259-328., 1998. URL doi:10.6028/jres.103.019.

[12] Paul Steinacker, Nard Dumoulin Stuyck, Wee Han Lim, Tuomo Tanttu, MengKe Feng, Andreas Nickl, Santiago Serrano, Marco Candido, Jesus D. Cifuentes, Fay E. Hudson, Kok Wai

Chan, Stefan Kubicek, Julien Jussot, Yann Canvel, Sofie Beyne, Yosuke Shimura, Roger Loo, Clement Godfrin, Bart Raes, Sylvain Baudot, Danny Wan, Arne Laucht, Chih Hwan Yang, Andre Saraiva, Christopher C. Escott, Kristiaan De Greve, and Andrew S. Dzurak. A 300 mm foundry silicon spin qubit unit cell exceeding 99 2024. URL https://arxiv.org/abs/2410.15590.

[13] Simon J Evered, Dolev Bluvstein, Marcin Kalinowski, Sepehr Ebadi, Tom Manovitz, Hengyun Zhou, Sophie H Li, Alexandra A Geim, Tout T Wang, Nishad Maskara, et al. High-fidelity parallel entangling gates on a neutral-atom quantum computer. *Nature*, 622(7982): 268–272, 2023. URL https://www.nature.com/articles/s41586-023-06481-y.

[14] Jong-Moo Lee, Jiho Park, Jeongho Bang, Young-Ik Sohn, Alessio Baldazzi, Matteo Sanna, Stefano Azzini, and Lorenzo Pavesi. Quantum states generation and manipulation in a programmable silicon-photonic four-qubit system with high-fidelity and purity. *APL Photonics*, 9(7), 2024. URL https://inspirehep.net/files/2553b9eef2262e37877731d139f8995e.

2

Semiconductors

2.1 Introduction

Semiconductors possess properties intermediate between conductors and insulators, making them indispensable in modern electronics. They are used in microchips, processors, transistors, diodes, solar cells, lasers, LEDs, and sensors, among many other applications. Their ability to regulate electrical flow is what makes them essential for technological advancements. This chapter explores the physics of semiconductors, providing insight into why they are fundamental to modern technology.

The most well-known semiconductor is silicon (Si). Both silicon and germanium (Ge) crystallize in a diamond-like structure, where each atom is surrounded by four nearest neighbors, forming a tetrahedral arrangement. In addition to elemental semiconductors, compound semiconductors can be formed by combining two or more elements, such as GaAs (gallium arsenide), ZnS (zinc sulfide), HgTe (mercury telluride), and PbS (lead sulfide). Oxides like CuO (copper oxide) are also well-known semiconductors. Furthermore, semiconductors can be composed of organic compounds, such as $(CH_2)_n$, or magnetic elements, as seen in materials like $Cd_{1-x}Mn_xTe$. This thesis primarily focuses on group IV semiconductors (Si, Ge) and the III-V compound semiconductor GaAs. This introductory chapter is based on the books [1, 2] and the first two chapters of [3].

2.2 General theory of semiconductors

To understand the physics of semiconductors, we rely on various mathematical models, some that are semi-empirical such as the tight-binding method, the $\boldsymbol{k}\cdot\boldsymbol{p}$ method, the pseudopotential approach, the orthogonalized plane wave method, and even *ab initio* techniques. In this chapter, we explore the structural properties of semiconductors and introduce key group theory techniques that facilitate the analysis of their optical properties. We also provide a detailed discussion of the tight-binding method, which forms the foundation of the present work. The $\boldsymbol{k}\cdot\boldsymbol{p}$ method, on the other hand, is employed in chapter 4 to analyse the electronic band structure and to derive analytical expressions for the inverse effective mass tensor as well as the $\boldsymbol{g}$-tensor.

The Hamiltonian for a perfect crystal is

$$\mathcal{H} = \underbrace{\sum_i \frac{p_i^2}{2m_i} - \sum_{j,i} \frac{e^2 Z_j}{4\pi\epsilon_0 |\boldsymbol{r}_i - \boldsymbol{R}_j|} + \frac{1}{2}\sum_{i,i'\neq i} \frac{e^2}{4\pi\epsilon_0 |\boldsymbol{r}_i - \boldsymbol{r}_{i'}|}}_{\mathcal{H}_e} + \sum_j \frac{P_j}{2M_j} + \frac{1}{2}\sum_{j,j'\neq j} \frac{e^2 Z_j Z_{j'}}{4\pi\epsilon_0 |\boldsymbol{R}_j - \boldsymbol{R}_{j'}|}, \quad (2.1)$$

where $\boldsymbol{r}_i$ is the position of the i^{th} electron with the momentum p_i and mass m_i, $\boldsymbol{R}_j$ the position of the j^{th} nucleus with the momentum $\boldsymbol{P}_j$, mass M_j and the atomic number Z_j, $-e$ is the electron charge and ϵ_0 is the permittivity of vacuum, we do not consider the spin-orbit interaction yet.

Here, we apply two key approximations. First, we assume that the core electrons (those in filled orbitals) can be grouped together with the nuclei, effectively treating them as a single entity. Second, we invoke the Born-Oppenheimer approximation, which exploits the fact that ions are significantly heavier than electrons and thus move much more slowly. As a result, the electrons perceive the ions as effectively stationary. In a crystalline solid, we further assume that each electron experiences the same average potential $V(\boldsymbol{r})$ which is periodic in nature. This leads to the following Schrödinger equation for individual electrons,

$$\mathcal{H}_{1e}\Phi_n(\boldsymbol{r}) = \left(\frac{p^2}{2m} + V(\boldsymbol{r})\right)\Phi_n = E_n. \quad (2.2)$$

The potential can be obtained either from first-principles calculations or through semi-empirical approaches, where it is parameterised based on experimental data. Given that this potential is periodic, the wavefunction Φ_n can be expressed as a Bloch function,

$$\Phi_{\boldsymbol{k}}(\boldsymbol{r}) = u_{\boldsymbol{k}}(\boldsymbol{r})e^{i\boldsymbol{k}\cdot\boldsymbol{r}}, \quad (2.3)$$

where $\boldsymbol{k}$ are the wave vectors and $u_{\boldsymbol{k}}$ is a periodic function with the periodicity of the crystal. If we translate $\boldsymbol{r}$ with a vector $\boldsymbol{R}$ which corresponds to the periodicity of V,

$$T_{\boldsymbol{R}}\Phi_{\boldsymbol{k}}(\boldsymbol{r}) = \Phi_{\boldsymbol{k}}(\boldsymbol{r}+\boldsymbol{R}) = u_{\boldsymbol{k}}(\boldsymbol{r})e^{i\boldsymbol{k}\cdot(\boldsymbol{r}+\boldsymbol{R})} = \Phi_{\boldsymbol{k}}(\boldsymbol{r})e^{i\boldsymbol{k}\cdot\boldsymbol{R}}. \tag{2.4}$$

Thus, $\Phi_{\boldsymbol{k}}(\boldsymbol{r})$ is also an eigenfunction of $T_{\boldsymbol{R}}$ and $T_{\boldsymbol{R}}$ and $\mathcal{H}_{1e}$ commute.

In periodic crystals, $\boldsymbol{R}$ is expressed in terms of the primitive lattice vectors, which define the positions of all lattice points within the crystal. The primitive lattice vectors of a face-centered cubic (fcc) lattice are,

$$a_1 = \left(\frac{a_0}{2}, \frac{a_0}{2}, 0\right), a_2 = \left(\frac{a_0}{2}, 0, \frac{a_0}{2}\right), a_3 = \left(0, \frac{a_0}{2}, \frac{a_0}{2}\right), \tag{2.5}$$

where a_0 is the length of the unit cell. The reciprocal lattice vectors are defined by,

$$\boldsymbol{b}_i = 2\pi\frac{\boldsymbol{a}_j \times \boldsymbol{a}_k}{(\boldsymbol{a}_1 \times \boldsymbol{a}_2)\cdot \boldsymbol{a}_3}. \tag{2.6}$$

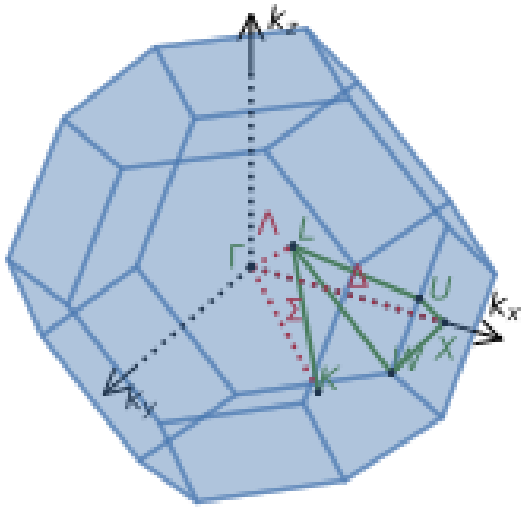

Figure 2.1: Brillouin zone of an fcc lattice. The special points and the special directions (indicated by the Greek letters with the exception of Γ) are shown in the figure.

The wave vector $\boldsymbol{k}$ is represented as a point in reciprocal space. The first Brillouin zone is the smallest polyhedron in $\boldsymbol{k}$-space, defined by the Bragg planes. For an fcc lattice, the special points of the first Brillouin zone are,

- Γ: the center of the Brillouin zone,
- K: the midpoint of an edge connecting two hexagonal faces,
- L: the center of a hexagonal face,
- U: the midpoint of an edge connecting a hexagonal and a square face,
- W: a corner point,
- X: the center of a square face.

The high-symmetry directions in the Brillouin zone include, Δ (between Γ and X), Σ (between Γ and K), Λ (between Γ and L). These directions are significant as they exhibit a high number of symmetry operations and are also known as special directions. Fig.2.1 illustrates these special points and the symmetry directions in the first Brillouin zone of a fcc lattice. If two wave vectors, $\boldsymbol{k}$ and $\boldsymbol{k}'$ are related by a symmetry operation, the eigenenergies must be equal at these points. For example, since an fcc Brillouin zone has six square faces with centers at X, the energy at all six X points is identical.

In the next section, we examine the symmetry operations relevant to the crystal structures of the semiconductors considered in this work. We introduce concepts from group theory, which provide the framework for understanding how wavefunctions and operators transform under the symmetries of the crystal lattice.

2.3 Groups and their representation

To develop a deeper understanding of semiconductors, we first introduce the fundamental concepts of group theory. These group-theoretical methods will be essential in later chapters, where they will be used to establish relationships between the g-factor (or more precisely, the $\boldsymbol{g}$-tensor) and quantum information—the central focus of this thesis. In this chapter, we emphasize the role of underlying symmetries in physical systems.

2.3.1 Groups and symmetry

A symmetry is a transformation that maps an object onto itself preserving all of its structure. A group is a collection of transformations that remains invariant under a set of same symmetric operations. A group must satisfy the following four properties:

1. Closure: let $a, b \in \mathcal{G}$, then any operation 'o' defined on the group must return $aob \in \mathcal{G}$.
2. Associativity: $(a\,o\,b)\,o\,c = a\,o(b\,o\,c)$.
3. Identity: the group must admit an element e such that $e\,o\,a = a, \forall a \in \mathcal{G}$.
4. Inverse element: the group must admit an element such that $a^{-1}\,o\,a = e, \forall a \in \mathcal{G}$.

2.3.2 Cosets and classes of a group

An element B of a group $\mathcal{G}$ is a conjugate element of A if there exist an element G such that $B = GAG^{-1}$. A is also said to be a conjugate of B. The set of all elements that are conjugate to each other is called a class. The unit element E always forms a class by itself.

Similarly, if the elements of the subgroup $\mathcal{H}$ are transformations $G\mathcal{H}G^{-1}$ for an element G of the group $\mathcal{G}$, then $\mathcal{H}$ is called a conjugate subgroup. A subgroup may not contain all mutually conjugate elements but if $G\mathcal{H}G^{-1} = \mathcal{H}$ for all G then $\mathcal{H}$ is an invariant subgroup of $\mathcal{G}$. And therefore, invariant subgroups must consist of classes. Using a subgroup $\mathcal{H}$, one is able to obtain a right (left)-coset of a group $\mathcal{G}$ by multiplying the element G_1 that does not belong to $\mathcal{H}$ to its right (left), $\mathcal{H}G_1$ $(G_1\mathcal{H})$. Multiplying another element G_2 which belongs to neither $\mathcal{H}$ nor $\mathcal{H}G_1$, one can obtain another right (left)-coset. One can thus create a right-coset decomposition,

$$\mathcal{G} = \mathcal{H}G_1 + \mathcal{H}G_2 + ... + \mathcal{H}G_n, \tag{2.7}$$

or a left decomposition,

$$\mathcal{G} = G_1\mathcal{H} + G_2\mathcal{H} + ... + G_n\mathcal{H}. \tag{2.8}$$

If the left and the right cosets of a group are equal to each other $G\mathcal{H} = \mathcal{H}G$, then $\mathcal{H}$ is an invariant subgroup of $\mathcal{G}$.

2.3.3 The SO(3) symmetry group

One of the simplest symmetry groups is the rotation group also denoted as $SO(3)$. A rotation is parametrized by an angle which determines the amount by which an object should be rotated and an axis which passes through the origin around which the rotation must take places. It is isometric, preserves the origin and the orientation of the object. Since rotations are non-commutative, they belong to the non-abelian group (groups whose elements are non-commutative). In other words, the order in which a rotation is applied matters. Rotations are described by 3×3 orthogonal matrices acting on $\mathbb{R}^3$ whose determinant is 1. These are known as special orthogonal matrices, hence the name $SO(3)$. The most general form of a rotation matrix around an axis

$\mathbf{n} = (n_x, n_y, n_z)$ such that $n_x^2 + n_y^2 + n_z^2 = 1$ by an angle θ is [4],

$$R(n,\theta) = \begin{pmatrix} n_x^2(1-cos\,\theta) + cos\,\theta & n_x n_y(1-cos\,\theta) - n_z sin\,\theta & n_x n_z(1-cos\,\theta) + n_y sin\,\theta \\ n_x n_y(1-cos\,\theta) + n_z sin\,\theta & n_y^2(1-cos\,\theta) + cos\,\theta & n_y n_z(1-cos\,\theta) - n_x sin\,\theta \\ n_x n_z(1-cos\,\theta) - n_y sin\,\theta & n_y n_z(1-cos\,\theta) + n_x sin\,\theta & n_z^2(1-cos\,\theta) + cos\,\theta \end{pmatrix}. \tag{2.9}$$

Note that the eigenvalues of the rotation matrices are $\lambda = \pm 1$. The rotation group acts in the spatial subspace of our semiconductors.

2.3.4 The SU(2) symmetry group

Another group acting on the vector space $\mathbb{C}^2$ of an object is the special unitary group $SU(2)$. The action of this group on a complex vector is given by the unitary matrix of determinant 1,

$$U(x,y) = \begin{pmatrix} x & y \\ -y^* & x^* \end{pmatrix}, \tag{2.10}$$

where x, y are two complex numbers with their complex conjugates, x^*, y^*, such that $|x|^2 + |y|^2 = 1$.

We know that any matrix belonging to $SU(2)$ can be written in terms of the Pauli matrices,

$$\sigma_x = \begin{pmatrix} 0 & 1 \\ 1 & 0 \end{pmatrix} \sigma_y = \begin{pmatrix} 0 & -i \\ i & 0 \end{pmatrix} \sigma_z = \begin{pmatrix} 1 & 0 \\ 0 & -1 \end{pmatrix}. \tag{2.11}$$

One can then define a homomorphic mapping $SU(2) \to SO(3) : U\sigma_i U^\dagger = \sigma_j R_{ji}$ [5] such that,

$$\begin{aligned} U(x,y)\sigma_x U(x,y) &= Re(x^2 - y^2)\sigma_x - Im(x^2 - y^2)\sigma_y + 2Re(x\bar{y})\sigma_z, \\ U(x,y)\sigma_y U(x,y) &= Im(x^2 + y^2)\sigma_x + Re(x^2 + y^2)\sigma_y + 2Im(x\bar{y})\sigma_z, \\ U(x,y)\sigma_z U(x,y) &= -2Re(xy)\sigma_x + 2Im(xy)\sigma_y + (|x|^2 - |y|^2)\sigma_z. \end{aligned} \tag{2.12}$$

or,

$$R(U(x,y)) = \begin{pmatrix} Re(x^2 - y^2)\sigma_x & Im(x^2 + y^2)\sigma_x & -2Re(xy)\sigma_x \\ -Im(x^2 - y^2)\sigma_y & Re(x^2 + y^2)\sigma_y & 2Im(xy)\sigma_y \\ 2Re(x\bar{y})\sigma_z & 2Im(x\bar{y})\sigma_z & (|x|^2 - |y|^2)\sigma_z \end{pmatrix}. \tag{2.13}$$

This gives a direct relation between the matrices of $SO(3)$ and $SU(2)$. One can also see this explicitly for a rotation in a Bloch sphere around an axis $\boldsymbol{n} = (n_x, n_y, n_z)$ by an angle θ which is given in terms of the generators of spin ($[\boldsymbol{J}_a, \boldsymbol{J}_b] = i\epsilon_{abc}\boldsymbol{J}_c$) [6]. So for $\mathbf{J} = \boldsymbol{\sigma}/2$, the rotation is given by $U = e^{-i\frac{\theta}{2}(\mathbf{n}\cdot\boldsymbol{\sigma})}$ which, upto the first-order in Taylor expansion, is,

$$U(\mathbf{n},\theta) = \mathbb{1}\cos\frac{\theta}{2} - i(\mathbf{n}\cdot\boldsymbol{\sigma})\sin\frac{\theta}{2} = \begin{pmatrix} \cos\frac{\theta}{2} - in_z\sin\frac{\theta}{2} & -n_y\sin\frac{\theta}{2} - in_x\sin\frac{\theta}{2} \\ n_y\sin\frac{\theta}{2} - in_x\sin\frac{\theta}{2} & \cos\frac{\theta}{2} + in_z\sin\frac{\theta}{2} \end{pmatrix}. \tag{2.14}$$

Recognising $x = \cos\frac{\theta}{2} - in_z \sin\frac{\theta}{2}$ and $y = -(n_y + in_x)\sin\frac{\theta}{2}$, it is easy to recover Eq.2.9 by the mapping defined in Eq.2.13.

2.3.5 Point groups and space groups

A *point group* is a collection of rotational operations that describe the symmetry both on a microscopic level (as for a molecule) and on a macroscopic level (as for a crystal). These operations leave a point fixed and the overall arrangement of a crystal unchanged. The total number of such operations within the group is called the order of the group. Operations of the point group in the Schoenflies notation are generally described as follows:

1. E: identity operation
2. C_n: rotation through an angle $\frac{2\pi}{n}$, the rotation axis is called an n-fold axis.
3. I: space inversion, takes $\boldsymbol{R}$ to -$\boldsymbol{R}$, $\boldsymbol{R}$ is the atom position.
4. σ: mirror reflection, it has three kind of suffixes according to the properties of the mirror plane.
5. σ_h: mirror reflection in the horizontal plane.
6. σ_v: mirror reflection in the vertical plane.
7. σ_d: mirror reflection in the diagonal plane.
8. IC_n: rotary inversion - rotation through $\frac{2\pi}{n}$ followed by inversion.

There are 32 crystallographic point groups in total. In this thesis, we focus on the cubic group, which includes five crystallographic point groups: T, T_d, T_h, O, and O_h. These groups possess the highest degree of symmetry and are particularly relevant to the crystallographic structures of solids that play a crucial role in spin qubit fabrication.

Apart from the local rotation symmetry, crystalline solids also exhibit translational symmetry i.e due to the periodic potential the electrons maintain the same wavefunction with respect to all the lattice translations. The symmetry group of crystalline solids which includes both point group symmetries and translation is known as a *space group*. Space groups can be classified into two types - a *symmorphic group* consists of point group operations combined with primitive lattice translations, a *non-symmorphic group* includes point group operations with fractional lattice translations. The space group of the diamond structure is non-symmorphic as it contains glide planes, which involve a combination of reflection and fractional translation.

2.3.6 Little groups

The little group, $\mathcal{L}$ is a subgroup of the space group associated with a particular wavevector $\boldsymbol{k}$ along a particular direction in the reciprocal lattice space. The operations of this group leave a wavevector invariant (up to a reciprocal lattice vector). These include rotations, reflections and possibly inversions.

2.3.7 Representations: reducible and irreducible.

Let $\mathcal{G}$ be a group with elements $G_1, G_2, ..., G_n$. Then the set of matrices $\hat{\mathbf{D}}(G_1), \hat{\mathbf{D}}(G_2), ..., \hat{\mathbf{D}}(G_n)$ satisfying,

$$\hat{\mathbf{D}}(G_i)\hat{\mathbf{D}}(G_j) = \hat{\mathbf{D}}(G_k) \tag{2.15}$$

for the corresponding relation between the group elements $G_iG_j = G_k$, is called a *representation* of the group $\mathcal{G}$ and $\hat{\mathbf{D}}(G_i)$ is called a *representation matrix*. In other words a representation indicates how the elements of a group act as matrices (or operators) on a vector space.

Representations are not unique. A new representation can be generated for example by a simple unitary transformation $UD(G)U^{-1}$. The representations $D(G)$ and $UD(G)U^{-1}$ are said to be equivalent. Another way of generating a representation is by combining two representations $\hat{D}^{[1]}(G_i)$ and $\hat{D}^{[2]}G_i$ in the following way,

$$\hat{D}(G_i) = \begin{pmatrix} D^{[1]}(G_i) & 0 \\ 0 & D^{[2]}(G_i) \end{pmatrix} = \hat{D}^{[1]}(G_i) \oplus \hat{D}^{[2]}(G_i). \tag{2.16}$$

$\hat{D}(G_i)$ is a reducible representation. Note that the dimensionality of $\hat{D}(G_i)$ is the sum of the dimensionalities of $\hat{D}^{[1]}(G_i)$ and $\hat{D}^{[2]}(G_i)$.

Basis of a representation

$\psi_1, \psi_2, ..., \psi_d$ is called a basis for a representation if

$$G_i\psi_\nu = \sum_{\mu=1}^{d} \psi_\mu D_{\mu\nu}, \quad G_i \in \mathcal{G}, \tag{2.17}$$

where $\psi_1, \psi_2, ..., \psi_d$ are independent elements in a vector space.

Irreducible representations of a group

A representation that cannot be expressed in a block diagonal form, as shown in Eq. 2.16, or reduced through any similarity transformation, is called an irreducible representation. In Eq. 2.16, the left-hand side represents a reducible representation, which has been decomposed into a direct sum of two irreducible representations on the right-hand side. Unlike reducible representations,

an irreducible representation cannot be further decomposed into smaller invariant subspaces.

Over the years, various notations have been adopted for representing group representations. The Table.2.1 from [3] provides an example of the different notations used for the group T_d, In the

Koster notation	BSW notation	Molecular notation
Γ_1	Γ_1	A_1
Γ_2	Γ_2	A_2
Γ_3	Γ_{12}	E
Γ_4	Γ_{15}	T_2
Γ_5	Γ_{25}	T_1

Table 2.1: Conversion of different notations of single group representations from [3].

case of inversion symmetric groups, because of the parity of the wavefunction, sometimes the notations can have a prime index, i.e. Γ'_{12} or a plus or minus sign, Γ_6^+, Γ_7^-. In later chapters, we will work with the Koster notation.

Let us consider the example of the group O_h. At the Γ-point, the representations are labeled as Γ_i, with an additional prime ($'$) or $\pm$ sign indicating the parity of the wavefunction. Moving away from the Γ-point along the Δ-direction, the symmetry is reduced. In this case, the relevant little group is C_{4v}, meaning that the representation of O_h becomes reducible in this direction. It can be decomposed into irreducible representations of C_{4v}, with the resulting representations labeled as Δ_i,

$$\left[\Gamma_{25}^+\right]_{O_h} = \left[\Delta_{2'} + \Delta_5\right]_{C_{4v}}. \tag{2.18}$$

Table.2.2 [1] shows the compatibility relations between these three representations for the group O_h using the BSW notation.

Γ_1^+	Γ_2^+	Γ_{12}^+	Γ_{15}^-	Γ_{25}^+	Γ_1^-	Γ_2^-	Γ_{12}^-	Γ_{15}^+	Γ_{25}^-
Δ_1	Δ_2	$\Delta_1 + \Delta_2$	$\Delta_1 + \Delta_5$	$\Delta_{2'} + \Delta_5$	$\Delta_{1'}$	$\Delta_{2'}$	$\Delta_{1'} + \Delta_{2'}$	$\Delta_{1'} + \Delta_5$	$\Delta_2 + \Delta_5$
Λ_1	Λ_2	Λ_3	$\Lambda_1 + \Lambda_3$	$\Lambda_1 + \Lambda_3$	Λ_2	Λ_1	Λ_3	$\Lambda_2 + \Lambda_3$	$\Lambda_2 + \Lambda_3$
Σ_1	Σ_4	$\Sigma_1 + \Sigma_4$	$\Sigma_1 + \Sigma_3 + \Sigma_4$	$\Sigma_1 + \Sigma_2 + \Sigma_3$	Σ_2	Σ_3	$\Sigma_2 + \Sigma_3$	$\Sigma_2 + \Sigma_3 + \Sigma_4$	$\Sigma_1 + \Sigma_3 + \Sigma_4$

Table 2.2: The representation Γ_i decompose into the representation Δ_i, Λ_i and Σ_i (in the BSW notation) along the respective directions.

Unitarisation of Representations

A finite representation of the group $\mathcal{G}$ can always be transformed into a unitary representation, which can then be used without loss of generality. This result is demonstrated in section 4.5.1 in

the book [2]. Building on this along with the two key lemmas proposed by Schur, one can show that the irreducible representations satisfy the following relation:

$$\sum_G D_{ij}^{(\alpha)}(G)^* D_{kl}^{(\beta)}(G) = \frac{n}{d_\alpha}\delta_{\alpha\beta}\delta_{ik}\delta_{jl}. \tag{2.19}$$

This is known as the "Wonderful Orthogonality Theorem". Here n is the number of elements in the group and d_α is the dimension of the representation $D^{(\alpha)}$. The $\delta_{\alpha\beta}$ on the right hand side shows orthogonality for inequivalent representations as well. For proof, refer to section 4.5.4 [2].

2.3.8 Double group

So far, we have not taken spin into consideration. The double group is an extension of the point group that accounts for half-integer spins (for example, electrons). The spins transform differently under these group operations as they acquire a phase upon a rotation by 2π (c.f. Berry phase). The operations acting on the spin elements of the $SU(2)$ group can be determined by the mapping shown in Eq.2.13. This will become important later on when we look at electrons (holes) of normal semiconductors especially with a finite spin-orbit interactions. All the crystallographic point-groups considered in this thesis are double-groups.

Irreducible representation of the double group

The double-valued representations show how spinors transform under the unitary operations of the point group. The irreducible representation $\mathbf{D}^{(1/2)}$ of the $SU(2)$ rotation group has the matrix form as described in Eq.2.14 of a rotation by an angle θ around the axis $\boldsymbol{n}$. A rotation $\mathcal{R}$, by an angle θ and a rotation $\bar{\mathcal{R}}$ by an angle $\theta + 2\pi$ are physically the same but the two representations are,

$$\hat{\mathbf{D}}^{(1/2)}(\bar{\mathcal{R}}) = -\hat{\mathbf{D}}^{(1/2)}(\mathcal{R}), \tag{2.20}$$

since a rotation by 2π changes the sign of the spin function as mentioned earlier. Hence this representation is called *double-valued representation*. The unit element in this case is the pair $\{E, \bar{E}\}$. The group has twice the number of elements half of which are denoted by $\bar{R} = R\bar{E}$ where R are the elements of the original single group.

2.3.9 Characters and character tables

The character of a representation $\mathbf{D}$ is the trace of the representation matrix,

$$\chi(G) = \mathrm{Tr}\{\hat{\boldsymbol{D}}(G)\} = \sum_{i=1}^{d} \boldsymbol{D}_{ii}(G). \tag{2.21}$$

For example, the unit element is represented by the unit matrix, E. So its character $\chi(E)$ is the dimension of E. Due to its cyclic property, the trace remains invariant with respect to similarity

transformations,

$$\hat{\boldsymbol{D}}(G)\hat{\boldsymbol{D}}(G_i)\hat{\boldsymbol{D}}(G)^{-1} = \hat{\boldsymbol{D}}(G_j),$$
$$\chi(G_i) = \chi(G_j). \tag{2.22}$$

As a result, the characters of equivalent irreducible representations are equal. Moreover, all representations within the same equivalence class have the same characters. Characters of representations also obey the following orthogonality rules, the proof of which can be found in section 4.6.1 in the book [2].

1. For the characters $\chi^{(\alpha)}(G), \chi^{(\beta)}(G)$ of the irreducible representations $\mathbf{D}^{(\alpha)}, \mathbf{D}^{(\beta)}$ respectively with n group elements,
$$\sum_G \chi^{(\alpha)}(G)^* \chi^{(\beta)}(G) = n\delta_{\alpha\beta}. \tag{2.23}$$
One may also generalize this to h_k elements in the class $\mathcal{C}_k$, where n_c is total number of classes,
$$\sum_{k=1}^{n_c} h_k \chi^{(\alpha)}(\mathcal{C}_k)^* \chi^{(\beta)}(\mathcal{C}_k) = n\delta_{\alpha\beta}. \tag{2.24}$$

2. The second orthogonality relation is for the character of the same representation but different classes,
$$\sum_{\alpha=1}^{n_r} \chi^{(\alpha)}(\mathcal{C}_i)^* \chi^{(\alpha)}(\mathcal{C}_j) = \delta_{ij}\frac{n}{h_i}. \tag{2.25}$$

The trace of a reducible representation, $\mathbf{D} = \sum_\alpha q_\alpha \mathbf{D}^{(\alpha)}$ is $\chi(G) = \sum_\alpha q_\alpha \chi^{(\alpha)}(G)$. n_r is the number of representations in the group and q_α is the multiplicity such that $q_{alpha} = d_\alpha$, the dimenion of the representation $D^{(\alpha)}$.

A character table is formed with j columns which contain j number of symmetry classes and j rows for j inequivalent irreducible representations of a group. Table.2.3 is the character table of the double group T_d. The above Eq.2.23, Eq.2.24, Eq.2.25 can be easily verified for the Table.2.3. The character table has all the information needed for the discussion of the symmetries of representation of a group. One can find the character tables for all other symmetry groups in [7].

2.4 Group representations in Quantum Mechanics

In the following, we explore quantum mechanical examples involving solids such as silicon, germanium, and gallium arsenide to illustrate the group theory concepts introduced so far.

T_d	$\{E\}$	$\{\bar{E}\}$	$\{8C_3\}$	$\{8\bar{C}_3\}$	$3\{C_2\}$	$\{6S_4\}$	$\{6\bar{S}_4\}$	$\{6\sigma_d\}$	Bases
Γ_1	1	1	1	1	1	1	1	1	R or xyz
Γ_2	1	1	1	1	1	-1	-1	-1	$S_xS_yS_z$
Γ_3	2	2	-1	-1	2	0	0	0	$(2z^2-x^2-y^2)$
Γ_4	3	3	0	0	-1	1	1	-1	$\sqrt{3}(x^2-y^2)$
Γ_5	3	3	0	0	-1	-1	-1	1	S_x, S_y, S_z
Γ_6	2	-2	1	-1	0	$\sqrt{2}$	$-\sqrt{2}$	0	$\phi(1/2,-1/2)$, $\phi(1/2,1/2)$
Γ_7	2	-2	1	1	0	$-\sqrt{2}$	$\sqrt{2}$	0	$\Gamma_6 \times \Gamma_2$
Γ_8	4	-4	-1	1	0	0	0	0	$\phi(3/2,-3/2)$, $\phi(3/2,-1/2)$ $\phi(3/2,1/2)$ $\phi(3/2,3/2)$

Table 2.3: Character table for the double group T_d.

2.4.1 Examples of group elements and little groups

We show here the group elements of the point groups of silicon, germanium (O_h) and gallium-arsenide (T_d) in 2.4.1. Along the high-symmetry directions, the basis functions of T_d transform according to the representations of the corresponding little groups:

- Δ-direction: The basis functions belong to the little group C_{4v}.
- Λ-direction: The basis functions transform according to the little group C_{3v}.
- Σ-direction: The basis functions follow the symmetry of the little group C_{2v}.

These little groups dictate the allowed symmetries of the electronic states along each direction.

The diamond and the zinc-blende structures

We will briefly outline the properties of the groups O_h and T_d. The zinc-blende structure consists of an fcc where atoms of two different types are arranged alternately. This structure is illustrated

in Fig.2.2, with the two atomic species represented as black and white atoms. The lattice constant

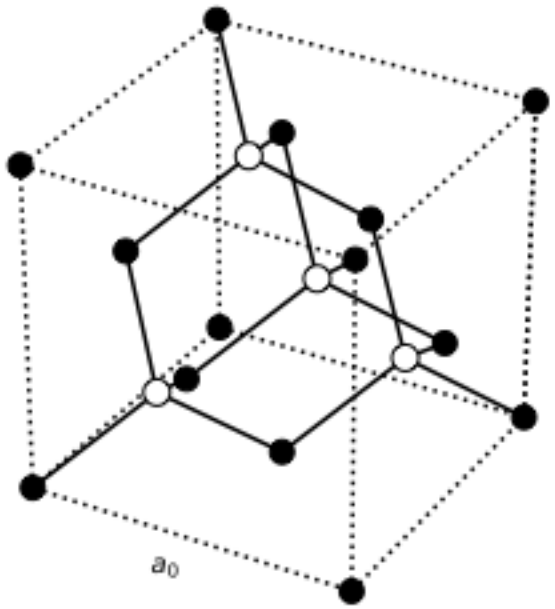

Figure 2.2: Zinc-blende lattice with two types of atoms based on the four neighboring vectors.

is denoted by a_0. We characterize the atom arrangements based on the four nearest neighbor vectors. For the black atoms, the four neighbors are located at

$$\boldsymbol{n}_1^b = \left(\frac{a_0}{4}, \frac{a_0}{4}, \frac{a_0}{4}\right), \boldsymbol{n}_2^b = \left(-\frac{a_0}{4}, -\frac{a_0}{4}, \frac{a_0}{4}\right), \boldsymbol{n}_3^b = \left(-\frac{a_0}{4}, \frac{a_0}{4}, -\frac{a_0}{4}\right), \boldsymbol{n}_4^b = \left(\frac{a_0}{4}, -\frac{a_0}{4}, -\frac{a_0}{4}\right). \quad (2.26)$$

Similarly for the white atoms, the four neighbors are positioned at

$$\boldsymbol{n}_1^w = \left(-\frac{a_0}{4}, -\frac{a_0}{4}, -\frac{a_0}{4}\right), \boldsymbol{n}_2^w = \left(\frac{a_0}{4}, \frac{a_0}{4}, -\frac{a_0}{4}\right), \boldsymbol{n}_3^w = \left(\frac{a_0}{4}, -\frac{a_0}{4}, \frac{a_0}{4}\right), \boldsymbol{n}_4^b = \left(-\frac{a_0}{4}, \frac{a_0}{4}, \frac{a_0}{4}\right). \quad (2.27)$$

The two atoms on every lattice site are separated by a quarter of the body-diagonal [111] relative to each other. They form a unit cell which is then repeated at every lattice site. Each atom is surrounded by four nearest neighbors, this forms the tetrahedron. This crystal structure is adopted by materials like gallium-arsenide. The point group symmetry of such structures, T_d, has the twenty-four symmetry operations described below. These operations are defined with respect to the origin placed at one of the atoms.

1. E: identity.
2. $8C_3$: rotation by $2\pi/3$ around the eight axes $[111], [\bar{1}11], [1\bar{1}1], [11\bar{1}], [\bar{1}\bar{1}\bar{1}], [1\bar{1}\bar{1}], [\bar{1}1\bar{1}], [1\bar{1}\bar{1}]$ respectively.
3. $3C_2$: rotation by π around the $[100], [010], [001]$ axes respectively.
4. $6S_4$: improper rotations of $\pi/2$ around $[100], [010], [001], [\bar{1}00], [0\bar{1}0], [00\bar{1}]$ axes.
5. 6σ: reflections with respect to $(110), (1\bar{1}0), (101), (10\bar{1}), (011), (01\bar{1})$ planes respectively.

The diamond structure is the same as the zinc-blende structure but the two atoms in the primitive unit cell are identical. This crystal structure is adopted by materials like silicon and germanium. The point group symmetry of such structures is O_h with four-eight symmetry operations that are described below. These operations are also defined with respect to the origin placed at one of the atoms.

1. E: identity.
2. $6C_4$: rotation by $\pi/2$ around $[001], [010], [100], [\bar{1}00], [0\bar{1}0], [00\bar{1}]$ axes.
3. $8C_3$: rotation by $2\pi/3$ around the eight axes $[111], [\bar{1}11], [1\bar{1}1], [11\bar{1}], [\bar{1}\bar{1}\bar{1}], [1\bar{1}\bar{1}], [\bar{1}1\bar{1}], [1\bar{1}\bar{1}]$ respectively.
4. $6C_2$: rotation by π around the $[100], [010], [001], [\bar{1}00], [0\bar{1}0], [00\bar{1}]$ axes respectively.
5. $3C_2'$: rotation by π around the axes passing through the edges of the octahedron.
6. $6S_4$: improper rotations, rotation by $\pi/2$ around $[100], [010], [001], [\bar{1}00], [0\bar{1}0], [00\bar{1}]$ axes followed by reflections around planes perpendicular to each of them respectively.
7. $8S_6$: rotation by $\pi/4$ around $[111], [\bar{1}11], [1\bar{1}1], [11\bar{1}], [\bar{1}\bar{1}\bar{1}], [1\bar{1}\bar{1}], [\bar{1}1\bar{1}], [1\bar{1}\bar{1}]$ axes followed by reflection around planes perpendicular to them respectively.
8. $6\sigma_d$: reflections with respect to $(110), (1\bar{1}0), (101), (10\bar{1}), (011), (01\bar{1})$ planes respectively.
9. $3\sigma_h$: reflections with respect to the three planes perpendicular to the C_4 axes.
10. i: inversion $(\boldsymbol{R} \rightarrow -\boldsymbol{R} + \left(\frac{a}{4} + \frac{a}{4} + \frac{a}{4}\right))$

where a is the lattice constant.

Representation	Wavefunction
L_1	$\sqrt{8}\cos\left(\frac{2\pi x}{a_0}\right)\cos\left(\frac{2\pi y}{a_0}\right)\cos\left(\frac{2\pi z}{a_0}\right)$
L_1	$\sqrt{8}\sin\left(\frac{2\pi x}{a_0}\right)\sin\left(\frac{2\pi y}{a_0}\right)\sin\left(\frac{2\pi z}{a_0}\right)$
L_4	$\sqrt{8}\sin\left(\frac{2\pi x}{a_0}\right)\sin\left(\frac{2\pi y}{a_0}\right)\cos\left(\frac{2\pi z}{a_0}\right)$; $\sqrt{8}\sin\left(\frac{2\pi x}{a_0}\right)\cos\left(\frac{2\pi y}{a_0}\right)\sin\left(\frac{2\pi z}{a_0}\right)$; $\sqrt{8}\cos\left(\frac{2\pi x}{a_0}\right)\sin\left(\frac{2\pi y}{a_0}\right)\sin\left(\frac{2\pi z}{a_0}\right)$
L_4	$\sqrt{8}\sin\left(\frac{2\pi x}{a_0}\right)\cos\left(\frac{2\pi y}{a_0}\right)\cos\left(\frac{2\pi z}{a_0}\right)$; $\sqrt{8}\cos\left(\frac{2\pi x}{a_0}\right)\sin\left(\frac{2\pi y}{a_0}\right)\cos\left(\frac{2\pi z}{a_0}\right)$; $\sqrt{8}\cos\left(\frac{2\pi x}{a_0}\right)\cos\left(\frac{2\pi y}{a_0}\right)\sin\left(\frac{2\pi z}{a_0}\right)$

Table 2.4: A set of symmetrized wavefunctions of the group T_d.

2.4.2 Symmetrisation of the wavefunctions

Consider a *nearly free electron* in a zinc-blende crystal meaning that the crystal potential that localizes it is almost negligible. Its energy is $E = \frac{\hbar^2 k^2}{2m}$. At the L point, $\boldsymbol{k} = \left(\frac{2\pi}{a_0}\right)(\pm 1, \pm 1, \pm 1)$ the wavefunctions[1] are [3],

The linear combination of wavefunctions that transform according to the respective irreducible representations can be obtained by using the projection operator as described in the following section.

2.4.3 Projection operator

One can obtain the representation matrices from the basis functions, provided they are available. Conversely, extracting the basis functions from the representation matrices requires a different approach. This is where the *projector operator* proves to be invaluable, offering a powerful and systematic formalism. The projection operator is defined as,

$$\hat{P}^{\Gamma_n}_{kl} \left|\Gamma_n l\right\rangle \equiv \left|\Gamma_n k\right\rangle, \tag{2.28}$$

where the operator $\hat{P}^{\Gamma_n}_{kl}$ transforms one basis vector $\left|\Gamma_n l\right\rangle$ into another basis vector $\left|\Gamma_n k\right\rangle$. We can rewrite this operator as a linear combination of the symmetry operators $\hat{P}_R$ with some coefficients A_{kl}, $\hat{P}^{\Gamma_n}_{kl} \left|\Gamma_n l\right\rangle = \sum_R A_{kl}(R)\hat{P}_R \left|\Gamma_n l\right\rangle = \left|\Gamma_n k\right\rangle$. Then $\hat{P}^{\Gamma_n}_{kl}$ is,

$$\hat{P}^{\Gamma_n}_{kl} = \frac{n}{h}\sum_R D^{\Gamma_n}(R)^*_{kl}\hat{P}_R. \tag{2.29}$$

[1] It is also common to denote the representations of these wavefunctions by Γ_i instead of L_i.

If $|\Gamma_n k\rangle$ is a basis state of the representation Γ_n then the projection operator acts trivially, $\hat{P}^{\Gamma_n}_{kk} |\Gamma_n k\rangle = |\Gamma_n k\rangle$. The projection operator can project the k^{th} partner of the irreducible representation Γ_n from an arbitrary function $F = \sum_{\Gamma_{n'}} \sum_j f_j^{\Gamma_{n'}} |\Gamma_{n'} j\rangle$,

$$\begin{aligned}\hat{P}^{\Gamma_n}_{kk} F &= \frac{n}{h} \sum_R \sum_{\Gamma_{n'}} \sum_j f_j^{\Gamma_{n'}} D^{\Gamma_n}(R)^*_{kk} \hat{P}_R |\Gamma_{n'} j\rangle \\ &= \frac{n}{h} \sum_{\Gamma_{n'}} \sum_j f_j^{\Gamma_{n'}} \underbrace{\sum_R D^{\Gamma_n}(R)^*_{kk} D^{\Gamma_{n'}}(R)_{jj'}}_{\frac{h}{n}\delta_{\Gamma_n\Gamma_{n'}}\delta_{jk}\delta j'k} |\Gamma_{n'} j\rangle = f_k^{\Gamma_n} |\Gamma_n k\rangle . \end{aligned} \tag{2.30}$$

An example of this appears in Chapter 4, where the projector, as defined in Eq.2.29, is used to extract the basis states of the little groups C_{2v} and C_{3v} from the eigenfunction $|\xi\rangle$ and $|\bar{\xi}\rangle$ of a crystal of the group T_d. This allows us to derive the relationship between the degenerate band states of T_d along Δ ans Λ, the two high-symmetry directions.

2.4.4 Representations, operators and eigenfunctions

Electric-dipole interactions are crucial to understand the optical transitions of semiconductors. These are governed by selection rules. We can define the selection rules in terms of the representations as explained in this section.

Let $\boldsymbol{p}$ be the momentum operator and $|\Psi_1\rangle$ be the wavefunction belonging to the representation Γ_4 in the group T_d. The action of the operator on the wavefunction $\boldsymbol{p}|\Psi_1\rangle$ generate a set of nine wavefunctions $|\Psi_3\rangle$ with nine dimensional representation which can be reduced to the irreducible representation $\Gamma_5 \oplus \Gamma_4 \oplus \Gamma_3 \oplus \Gamma_1$. We can look at the matrix element $\langle\Psi_2|\boldsymbol{p}|\Psi_1\rangle$ with another wavefunction $|\Psi_2\rangle$ belonging to a representation B not in $\Gamma_5 \oplus \Gamma_4 \oplus \Gamma_3 \oplus \Gamma_1$. Since the basis functions of different representations are orthogonal to each other, this matrix element is zero. This matrix element will be non-zero only when the direct product of the representation of $\boldsymbol{p}$ and $|\Psi_1\rangle$ contains the irreducible representation of $|\Psi_2\rangle$, this is the *matrix element theorem*. This defines the selection rules for the crystal. The set of selection rules for the representation Γ_4 are shown below using the direct products and direct sums of the representations of T_d [3],

$$\begin{aligned}&\Gamma_4 \otimes \Gamma_1 \to \Gamma_4, \\ &\Gamma_4 \otimes \Gamma_2 \to \Gamma_5, \\ &\Gamma_4 \otimes \Gamma_3 \to \Gamma_4 \oplus \Gamma_5, \\ &\Gamma_4 \otimes \Gamma_4 \to \Gamma_4 \oplus \Gamma_5 \oplus \Gamma_3 \oplus \Gamma_1, \\ &\Gamma_4 \otimes \Gamma_4 \to \Gamma_4 \oplus \Gamma_5 \oplus \Gamma_3 \oplus \Gamma_2. \end{aligned} \tag{2.31}$$

2.4.5 The pseudpotential method

We discussed the nearly free electron model but this does not predict the band gaps and the complexities of the band structure well. The *pseduopotential method* captures this better. In silicon, the $3s$ and $3p$ shells are partially filled with valence electrons. These electrons are not affected by the nucleus, but the core formed by the electrons in the $1s, 2s, 2p$ orbitals causes the wavefunction of the valence electrons to oscillate rapidly. Using this method, the true potential is replaced by a weaker potential that acts as a small perturbation overall and does not have an effect on the smooth part of the electron wavefunction. A small number of the Fourier components of the pseudopotential (also known as the pseudopotential form factors) help determine the band structure. We also include the spin-orbit interaction in this calculation. This thesis does not include other details of this method but the reader can find them in [3].

2.4.6 $\boldsymbol{k \cdot p}$ method

The $\boldsymbol{k} \cdot \boldsymbol{p}$ method is useful for interpreting optical spectra. However, we will not discuss it in detail here, as this method is detailed in chapter 4 where it is used to calculate analytical forms of the momentum matrix elements, the inverse effective mass, and the g-factor.

2.4.7 The tight binding method

In the *tight-binding method* we assume that the electrons are tightly bound to the nucleus. The wavefunctions of such electrons overlap when the atoms come close together. Therefore it is also known as *linear combination of atomic orbitals* (LCAO) method. This results in the formation of bonding states (symmetric with respect to interchange of orbitals) and anti-bonding states (asymmetric with respect to interchange of orbitals). Additionally, when the p-orbitals overlap along their axis, they form σ bonds. When they overlap perpendicular to their axis, they form π bonds. These interactions give rise to four linearly independent parameters, $\langle s|H|s\rangle = V_{ss\sigma}, \langle s|H|p_z\rangle = V_{sp\sigma}, \langle p_z|H|p_z\rangle = V_{pp\sigma}, \langle p_x|H|p_x\rangle = V_{pp\pi}$. Table 1 in [8] shows the necessary parameters. With this we can determine all the Hamiltonian matrix elements for a zinc-blende crystal lattice. The following equation shows the matrix element between the $s1$ and $s2$ Bloch-state basis functions,

$$H_{s1,s2} = \left(e^{i\boldsymbol{k}\cdot\boldsymbol{d}_1} + e^{i\boldsymbol{k}\cdot\boldsymbol{d}_2} + e^{i\boldsymbol{k}\cdot\boldsymbol{d}_3} + e^{i\boldsymbol{k}\cdot\boldsymbol{d}_4}\right) \langle s1|H_{int}|s2\rangle\,, \tag{2.32}$$

where $\boldsymbol{d}_1 = \left(\frac{a_0}{4}, \frac{a_0}{4}, \frac{a_0}{4}\right), \boldsymbol{d}_2 = \left(\frac{a_0}{4}, -\frac{a_0}{4}, -\frac{a_0}{4}\right), \boldsymbol{d}_3 = \left(-\frac{a_0}{4}, \frac{a_0}{4}, -\frac{a_0}{4}\right), \boldsymbol{d}_4 = \left(-\frac{a_0}{4}, -\frac{a_0}{4}, \frac{a_0}{4}\right)$ are the positions of the four nearest neighbors. The four parameters,

$$\begin{aligned} g_0 &= e^{i\boldsymbol{k}\cdot\boldsymbol{d}_1} + e^{i\boldsymbol{k}\cdot\boldsymbol{d}_2} + e^{i\boldsymbol{k}\cdot\boldsymbol{d}_3} + e^{i\boldsymbol{k}\cdot\boldsymbol{d}_4}, \\ g_1 &= e^{i\boldsymbol{k}\cdot\boldsymbol{d}_1} + e^{i\boldsymbol{k}\cdot\boldsymbol{d}_2} - e^{i\boldsymbol{k}\cdot\boldsymbol{d}_3} - e^{i\boldsymbol{k}\cdot\boldsymbol{d}_4}, \\ g_2 &= e^{i\boldsymbol{k}\cdot\boldsymbol{d}_1} - e^{i\boldsymbol{k}\cdot\boldsymbol{d}_2} + e^{i\boldsymbol{k}\cdot\boldsymbol{d}_3} - e^{i\boldsymbol{k}\cdot\boldsymbol{d}_4}, \\ g_3 &= e^{i\boldsymbol{k}\cdot\boldsymbol{d}_1} - e^{i\boldsymbol{k}\cdot\boldsymbol{d}_2} - e^{i\boldsymbol{k}\cdot\boldsymbol{d}_3} + e^{i\boldsymbol{k}\cdot\boldsymbol{d}_4}. \end{aligned} \tag{2.33}$$

arise from the direction cosines of the neighbors. We also include the spin-orbit parameters. The have a non-zero contributions only between the $|p_i\rangle$ states with the appropriate spins (details in section 5.2). This is the Chadi-Cohen model [9].

This model can be easily extended to use $sp^3d^5s^*$ orbitals. The energy bands are the eigenenergies of the Hamiltonian thus obtained form the above parameters and the eigenvectors are a linear combination of the atomic $sp^3d^5s^*$ orbitals. The band structure is shown in Fig.5.1.

The time-reversal operator

Time reversal symmetry plays a crucial role in quantum mechanical systems [1, 2], particularly in semiconductors with spin-orbit interaction. It is therefore essential to examine its properties and understand its impact on the representations.

The time reversal operator describes an inverse time evolution, effectively reversing the direction of time, $t \to -t$ and altering the sequence of events. While some physical quantities remain

Reversed	Preserved
Momentum: $\boldsymbol{p} \to -\boldsymbol{p}$	Position: $\boldsymbol{q} \to \boldsymbol{q}$
Magnetic field: $\boldsymbol{B} \to -\boldsymbol{B}$	Electric Field: $\boldsymbol{E} \to \boldsymbol{E}$
Spin: $\boldsymbol{\sigma} \to -\boldsymbol{\sigma}$	Kinetic energy: $\frac{p^2}{2m} \to \frac{p^2}{2m}$
Position wavefunction: $\psi(\boldsymbol{r}) \to \psi(\boldsymbol{r})^*$	Transition probability: $\lvert\langle\psi\rvert\phi\rangle\rvert^2 \to \lvert\langle\psi\rvert\phi\rangle\rvert^2$

Table 2.5: Quantities that change and do not change under time-reversal operation.

unchanged under the time reversal operation, others change signs [10], summarized in Table.2.5. In some literature, the operator is denoted as $\hat{\boldsymbol{\theta}}$ or $\hat{\boldsymbol{T}}$ with $\hat{\boldsymbol{\theta}}(\hat{\boldsymbol{T}}) = i\sigma_y\kappa$, where κ denotes complex conjugation. In this work, we adopt the former notation. $\hat{\boldsymbol{\theta}}$ always acts towards the right. This operator has the following properties:

1. *Commutation relation*: $\left[\hat{\boldsymbol{\theta}}, \mathcal{H}\right] = 0$ when $\boldsymbol{B} = 0$. This means that the eigenstates of the time reversal operator are also the eigenstates of the hamiltonian.

2. *Anti-linear or Anti-unitary*: $\hat{\boldsymbol{\theta}} i = -i\hat{\boldsymbol{\theta}}$ or $\hat{\boldsymbol{\theta}}^2 = -1$ for fermions.

3. *Complex conjugation*: since $\hat{\boldsymbol{\theta}}$ is anti-linear, $\hat{\boldsymbol{\theta}}\psi(x) = \psi(x)^*$.

It's effect on the energies of a Hamiltonian $\mathcal{H}$ with the eigenstates $\left|\psi_{n,k\uparrow}(\boldsymbol{r})\right\rangle$ is as follow,

$$\begin{aligned} \hat{\boldsymbol{\theta}}\mathcal{H}\left|\psi_{n,k\uparrow}(\boldsymbol{r})\right\rangle &= \mathcal{H}\hat{\boldsymbol{\theta}}\left|\psi_{n,k\uparrow}(\boldsymbol{r})\right\rangle = \mathcal{H}\left|\psi_{n,-k\downarrow}(\boldsymbol{r})\right\rangle \\ \implies E_{n,\uparrow}(\boldsymbol{k}) &= E_{n,\downarrow}(-\boldsymbol{k}). \end{aligned} \tag{2.34}$$

In this context, the representations are not necessarily real. The representations of the extended group which contain unitary as well as anti-unitary operations are called corepresentations. They are more generalized forms of representations as described so far. The time reversal operator splits degenerate bands with high symmetries into sets of bands that may not be degenerate. The following conditions determine the effect of the time reversal operator on the irreducible corepresentation of these bands,

1. The corepresentation matrices $\hat{\boldsymbol{D}}$ are real or can be made real by a unitary transformation. The time reversal operator will leave these representation matrices unchanged and not cause any extra degeneracies in $E(\boldsymbol{k})$.

2. If the corepresentation matrices $\hat{\boldsymbol{D}}$ and $\hat{\boldsymbol{D}}^*$ are not related by a unitary transformation, then they will form a time reversal symmetric pair and lead to a double degeneracy.

3. If the corepresentation matrices $\hat{\boldsymbol{D}}$ and $\hat{\boldsymbol{D}}^*$ are related by a unitary transformation but are not real, then also there is a double degeneracy causing these to be time reversal related.

The transformations of the representations of certain high symmetry bands for the crystallographic groups O, O_h, T, T_d and T_h is shown in Table.4.1 in chapter 4. The properties above describe the transformation of an irreducible corepresentation with respect to the anti-unitary operation, θ. We can generalize this to study the transformation of irreducible corepresentations under a non-unitary transformation. This is discussed in section 13.2 of [2]. We will apply this general formalism to the case of groups T and O (Appendix A).

Many other properties of semiconductors can be explored using the techniques introduced in this chapter. By building on these foundations, one can study various interactions, including electron-phonon coupling, defects, electrical transport, optical properties, and spectroscopy. We will not delve into these topics further, interested readers may refer to comprehensive sources such as [3]. However, we will now focus on the quantum confinement of electrons. In the next chapter, we provide an overview of spin qubits, a technology that bridges quantum computing and semiconductors.

Bibliography

[1] M.S. Dresselhaus, G. Dresselhaus, and A. Jorio. *Group Theory: Application to the Physics of Condensed Matter*. Springer Berlin Heidelberg, 2007. ISBN 9783540328971. URL https://books.google.de/books?id=sKaH8vrfmnQC.

[2] Teturo Inui, Yukito Tanabe, and Yositaka Onodera. *Group theory and its applications in physics*, volume 78. Springer Science & Business Media, 2012. See sections 13.2 and 13.3.

[3] Peter Y Yu and Manuel Cardona. *Fundamentals of semiconductors*, volume 619. Springer, 2005.

[4] Rotation matrix, 2004. URL https://en.wikipedia.org/wiki/Rotation_matrix. See section: Rotation matrix from axis and angle.

[5] DB Westra. Su (2) and so (3), 2008. URL https://www.mat.univie.ac.at/~westra/so3su2.pdf.

[6] Thomas L. Curtright. A compact formula for rotations as spin matrix polynomials. *Symmetry, Integrability and Geometry: Methods and Applications*, August 2014. ISSN 1815-0659. doi: 10.3842/sigma.2014.084. URL http://dx.doi.org/10.3842/SIGMA.2014.084.

[7] George F. Koster, John O. Dimmock, and Robert G. Wheeler. *The Properties of the Thirty-Two Point Groups*. MIT Press, 1963. URL https://babel.hathitrust.org/cgi/pt?id=mdp.39015022422318&view=1up&seq=7.

[8] J. C. Slater and G. F. Koster. Simplified lcao method for the periodic potential problem. *Phys. Rev.*, 94:1498–1524, Jun 1954. doi: 10.1103/PhysRev.94.1498. URL https://link.aps.org/doi/10.1103/PhysRev.94.1498.

[9] D. J. Chadi and Marvin L. Cohen. Tight-binding calculations of the valence bands of diamond and zincblende crystals. *Physica Status Solidi B-basic Solid State Physics*, 68:405–419, 1975. URL https://api.semanticscholar.org/CorpusID:12495144.

[10] Robert G Littlejohn. Time reversal, 2019. URL https://bohr.physics.berkeley.edu/classes/221/1112/notes/timerev.pdf.

3

Spin Qubits

3.1 Introduction

Spin qubits form a two-level system of electrons with spins up and down that is naturally defined. Among various physical realizations of qubits, spin qubits stand out because of their potential scalability which results from their compatibility with semiconductor technology and longer coherence. The coherence times in purified silicon can extend to milliseconds [1] which is longer than the coherence times of superconducting qubits. However, as we will see in this chapter, controlling the spins, readout, spin-orbit interactions make it challenging to realize them experimentally.

3.2 Physical implementation of spin qubits

Consider a GaAs/AlGaAs heterostructure where AlGaAs is grown over GaAs using molecular beam epitaxy (MBE). We dope the ALGaAs layer with silicon which causes free electrons to accumulate in a thin sheet in the GaAs layer just below the interface. These electrons all have the properties of GaAs. This sheet is called a two-dimensional electron gas (2DEG) and is filled with the spin states that we require as carriers of information in our spin-based quantum computer. A similar 2DEG can be formed by sandwiching a layer of Si between layers of SiGe. Since the bulk Si has an indirect band gap, it admits a sixfold degeneracy in the Δ-direction. This degeneracy is lifted by heterostructure and electrostatic confinement. Doping is not needed in this type of heterostructures as carriers can be accumulated using gates. In all three structures Si/SiGe, Ge/SiGe and GaAs/AlGaAs, the charges carriers are confined in the out-of-plane (growth) directions [2–4].

By applying negative gate voltage we are able to deplete regions in the 2DEG thus isolating certain number of electrons. These regions that trap the electrons are known as quantum dots (QDs) [2, 5, 6]. They behave as artificial atoms as they admit occupied and unoccupied energy levels [7]. Spin qubits are the spins of these trapped electrons. We classify them based on the number of spins that are confined together to represent them.

3.2.1 Loss-DiVincenzo qubit

The Loss-DiVincenzo qubit was the first ever proposal of a semiconductor spin-qubit [8]. The confinement of one electron per quantum dot is described by the Heisenberg exchange Hamiltonian,

$$\mathcal{H}(t) = \frac{1}{4}\sum_{\{ij\}} \boldsymbol{J}_{ij}(t)\sigma_i \cdot \sigma_j + \frac{1}{2}\sum_i g_i \mu_B \boldsymbol{B}_i \cdot \sigma_i, \tag{3.1}$$

where $\boldsymbol{B}_i, g_i$ are the effective magnetic field and the g-factor at site i. Initialization and spin measurements for such qubits is carried out by spin-selective tunneling effects using sensitive charge sensors. Single-qubit gates can be applied using static or oscillate magnetic fields [9–11] along with the time-dependent control of $\boldsymbol{B}_i$ or g_i. Two-qubit gates can be implemented by adjusting exchange interactions [12, 13]. These will be elaborated further on.

3.2.2 Donor based qubit

Another proposal made by Kane [14] involves the spin of an electron bound to a phosphorous donor in silicon. Such spins can have exceptionally long coherence times as the electron is shielded from external noise sources and is more localized. One of the major challenges of this type of qubit is the placement of the donor atoms in the silicon lattice.

3.2.3 Charge qubit

Consider a single electron shared between two quantum dots. This is called a charge qubit. When the dots are far apart, the electron can be either on the left dot, Q_L or on the right dot, Q_R. The ground states of these two dots are $|L\rangle, |R\rangle$ with the energies ϵ_L, ϵ_R respectively. The tunneling rate between the two dots is t, the detuning between the two dots is $\epsilon = \epsilon_L - \epsilon_R$ with the Hamiltonian,

$$H_{1e} = \frac{\epsilon}{2}\underbrace{\left(|L\rangle\langle L| - |R\rangle\langle R|\right)}_{\tau_z} - t\underbrace{\left(|L\rangle\langle R| + |R\rangle\langle L|\right)}_{\tau_x}. \tag{3.2}$$

The charge qubit is very sensitive to charge noise and is therefore not such a good qubit.

3.2.4 Singlet-triplet qubits

A multi-spin qubit can also be created by confining two electrons in two quantum dots (a double quantum dot, DQD) [15, 16]. Since the overall wavefunction must be anti-symmetric, we have

the following basis states,

$$|S_0\rangle = \frac{|LR\rangle + |RL\rangle}{\sqrt{2}} \otimes \frac{|\uparrow\downarrow\rangle - |\downarrow\uparrow\rangle}{\sqrt{2}}, |S_{LL}\rangle = |LL\rangle \otimes \frac{|\uparrow\downarrow\rangle - |\downarrow\uparrow\rangle}{\sqrt{2}}, |S_{RR}\rangle = |RR\rangle \otimes \frac{|\uparrow\downarrow\rangle - |\downarrow\uparrow\rangle}{\sqrt{2}},$$
$$|T_0\rangle = \frac{|LR\rangle - |RL\rangle}{\sqrt{2}} \otimes \frac{|\uparrow\downarrow\rangle + |\downarrow\uparrow\rangle}{\sqrt{2}}, |T_{\uparrow\uparrow}\rangle = \frac{|LR\rangle - |RL\rangle}{\sqrt{2}} \otimes |\uparrow\uparrow\rangle, |T_{\downarrow\downarrow}\rangle = \frac{|LR\rangle - |RL\rangle}{\sqrt{2}} \otimes |\downarrow\downarrow\rangle. \tag{3.3}$$

Here, the state $|S_0\rangle$ has unpolarized spin and is de-localized in the two dots whereas the states $|S_{LL}\rangle$ and $|S_{RR}\rangle$ have unpolarized spins but they are localized in left and the right dots respectively. The states $|T_0\rangle, |T_{\uparrow\uparrow}\rangle, |T_{\downarrow\downarrow}\rangle$ are de-localized in the two dots and the states $|T_{\uparrow\uparrow}\rangle, |T_{\downarrow\downarrow}\rangle$ have polarized spins.

The Hamiltonian describing the orbital interactions in the $\{S_{LL}, S_{RR}, S_0, T_{\uparrow\uparrow}, T_{\downarrow\downarrow}, T_0\}$ basis is,

$$H_{orb} = H_{1e}^{(1)} + H_{1e}^{(2)} = \epsilon\Big(|S_{LL}\rangle\langle S_{LL}| - |S_{RR}\rangle\langle S_{RR}| \Big) - \sqrt{2}t\Big(|S_{LL}\rangle\langle S_0| + |S_{RR}\rangle\langle S_0| \Big) + h.c., \tag{3.4}$$

where t is the tunneling parameter and $\langle S_i|H_{orb}|T_j\rangle = 0$ because either their spin parts or their orbitals are orthogonal. There is also a Coulomb interaction between the electrons sitting in the same dots,

$$H_{Cou} = U|S_{LL}\rangle\langle S_{LL}| + U|S_{RR}\rangle\langle S_{RR}|, \tag{3.5}$$

where U describes the potential that the electrons is subjected to. The dots are weakly coupled so the largest contribution comes from U, also known as *addition energy*. The DQD has the following Zeeman interaction,

$$\begin{aligned} H_{Zeeman} &= g\mu_B B_z\Big(|T_{\uparrow\uparrow}\rangle\langle T_{\uparrow\uparrow}| - |T_{\downarrow\downarrow}\rangle\langle T_{\downarrow\downarrow}| \Big) + g\mu_B \frac{B_x - iB_y}{2} |T_{\uparrow\uparrow}\rangle\langle T_0| + g\mu_B \frac{B_x + iB_y}{2} |T_{\downarrow\downarrow}\rangle\langle T_0| + h.c. \\ &\sim g\mu_B B_z\Big(|T_{\uparrow\uparrow}\rangle\langle T_{\uparrow\uparrow}| - |T_{\downarrow\downarrow}\rangle\langle T_{\downarrow\downarrow}| \Big), \end{aligned} \tag{3.6}$$

we rotate the magnetic field to be aligned with the z-direction.
Hence, the Hamiltonian of the full system in the basis $\{S_{LL}, S_{RR}, S_0, T_{\uparrow\uparrow}, T_{\downarrow\downarrow}, T_0\}$ is,

$$H_{DQD} = \begin{pmatrix} U+\epsilon & 0 & -\sqrt{2}t & 0 & 0 & 0 \\ 0 & U-\epsilon & -\sqrt{2}t & 0 & 0 & 0 \\ -\sqrt{2}t & -\sqrt{2}t & 0 & 0 & 0 & 0 \\ 0 & 0 & 0 & g\mu_B B_z & 0 & 0 \\ 0 & 0 & 0 & 0 & -g\mu_B B_z & 0 \\ 0 & 0 & 0 & 0 & 0 & 0 \end{pmatrix}. \tag{3.7}$$

The states $|S_{LL}\rangle$ and $|S_{RR}\rangle$ are higher in energy. We consider only the states which are de-localized in the two dots. This is equivalent to considering the block of Hamiltonian corresponding to the

basis $\{S_0, T_{\uparrow\uparrow}, T_{\downarrow\downarrow}, T_0\}$. This is the regime where the magnetic field is small, the tunneling, t, and the detuning, ϵ, are much smaller than U. In this case, the energy of the state $|S_0\rangle$ is reduced by $J \approx \frac{4t^2}{U}\left[1 + \frac{\epsilon^2}{U^2} + \mathcal{O}\left(\frac{\epsilon^4}{U^4}\right)\right]$,

$$H_{ST} = \begin{pmatrix} -J & 0 & 0 & 0 \\ 0 & g\mu_B B_z & 0 & 0 \\ 0 & 0 & -g\mu_B B_z & 0 \\ 0 & 0 & 0 & 0 \end{pmatrix}. \tag{3.8}$$

J is the exchange interaction parameter. We re-write the Hamiltonian in the computational basis,[1]

$$H_{2Q} = \begin{pmatrix} g\mu_B B_z & 0 & 0 & 0 \\ 0 & -J/2 & J/2 & 0 \\ 0 & J/2 & -J/2 & 0 \\ 0 & 0 & 0 & -g\mu_B B_z \end{pmatrix} = \frac{g\mu_B B_z}{2}\sigma_z^{(1)} + \frac{g\mu_B B_z}{2}\sigma_Z^{(2)} + \frac{J}{4}\boldsymbol{\sigma}^{(1)} \cdot \boldsymbol{\sigma}^{(2)} - \frac{J}{4}. \tag{3.9}$$

3.3 g-factor renormalization

Consider an electron in $1D$ with a Rashba-type spin-orbit interaction, $\alpha_R E_x p_z \sigma_y$ [17] with a characteristic length scale, l_{SO} which is inversely proportional to the strength of the spin-orbit parameter, α_R. We can define a local spin rotation,

$$U(z) = e^{i\sigma_y z/l_{SO}} = \begin{pmatrix} \cos(z/l_{SO}) & \sin(z/l_{SO}) \\ -\sin(z/l_{SO}) & \cos(z/l_{SO}) \end{pmatrix} \tag{3.10}$$

whose effect on spin is,

$$\begin{aligned} \tilde{\sigma}_x &= U^\dagger(z)\sigma_x U(z) = \sigma_x \cos(2z/l_{SO}) - \sigma_z \sin(2z/l_{SO}), \\ \tilde{\sigma}_y &= U^\dagger(z)\sigma_y U(z) = \sigma_y, \\ \tilde{\sigma}_z &= U^\dagger(z)\sigma_z U(z) = \sigma_z \cos(2z/l_{SO}) + \sigma_x \sin(2z/l_{SO}). \end{aligned} \tag{3.11}$$

When we take into account the complete Hamiltonian, including the spin-orbit interaction, the Zeeman term and a harmonic confinement in the lab frame,

$$H_{1D} = \frac{p^2}{2m} - \alpha_R E_x p_z \sigma_y + \frac{g\mu_B B_z}{2}\sigma_z + \frac{m\omega_z^2}{2}z^2, \tag{3.12}$$

[1] The basis change of H_{ST} involves first rearranging the Hamiltonian in the basis $\{T_{\uparrow\uparrow}, S_0, T_0, T_{\downarrow\downarrow}\}$ then applying the matrix $M = \begin{pmatrix} 1 & 0 & 0 & 0 \\ 0 & 1/\sqrt{2} & -1/\sqrt{2} & 0 \\ 0 & 1/\sqrt{2} & 1/\sqrt{2} & 0 \\ 0 & 0 & 0 & 1 \end{pmatrix}$, $H_{2Q} = M^T H_{ST} M$.

the application of the local unitary operation, as shown in Eq.3.10, gives it the following spin-independent form,

$$\tilde{H}_{1D} = \frac{p^2}{2m} - \alpha_R E_x p_z \sigma_y + \frac{g\mu_B B_z}{2}\left[\cos\left(\frac{2z}{l_{SO}}\right)\sigma_z + \sin\left(\frac{2z}{l_{SO}}\right)\sigma_x\right] + \frac{m\omega_z^2}{2}z^2. \tag{3.13}$$

The groundstate for the harmonic oscillator is $|\psi_0(z)\rangle = \frac{e^{-z^2/2l_z^2}}{\sqrt{l_z\sqrt{\pi}}}$ with $E_0 = \hbar\omega_z/2$ and characteristic length l_z, and therefore,

$$\langle \tilde{H}_{1D} \rangle = E_0 - E_{SO} + \frac{\mu_B B_z \sigma_z}{2} g e^{-l_z^2/l_{SO}^2}, \tag{3.14}$$

where the g-factor has been renormalized, $g \rightarrow g e^{-l_z^2/l_{SO}^2}$ [18–21]. Note that in this frame of reference, the spin is no longer rotating as was the case in the lab frame but the magnetic field seems to be rotating with respect to the static spin.

3.4 Readout

Consider a single electron transistor (SET) where a quantum dot with capacitance C is weakly coupled to source and drain contacts via tunnel barriers. The source and the drain have chemical potentials μ_S and μ_D respectively with a bias $\mu_S - \mu_D$. If the dot has N electrons and its chemical potential does not lie in the bias window then the energy required to add a dot will be $\Delta E = \frac{e^2}{C} + \Delta_{N+1}$ where Δ_{N+1} is the difference between the energy levels of electrons in level N and $N+1$. At low temperatures ($k_B T << e^2/C$), the transport of electrons is blocked. By apply-

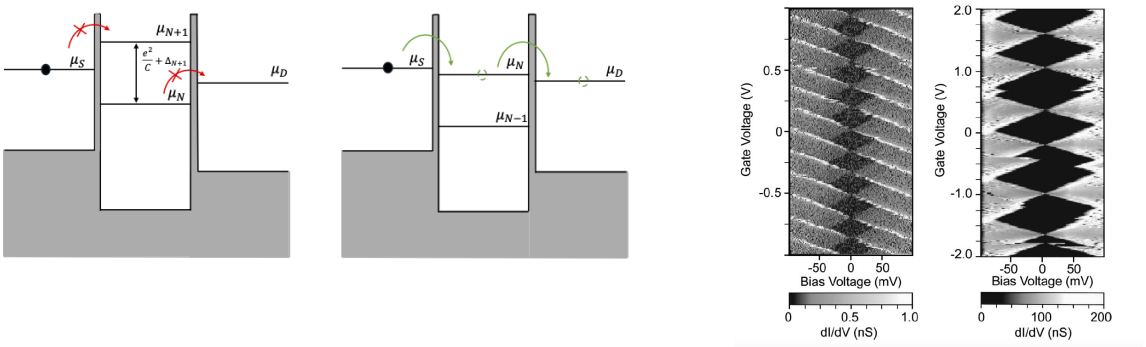

Figure 3.1: The images show the transport of a charge thorough a single electron transistor and a resulting Coulomb diamond from [22].

ing a negative voltage, the chemical potential of the dot can be raised at the level of or above μ_D so that one electron can tunnel out. In addition, if $\mu_S \gtrsim \mu_N \gtrsim \mu_D$ then the population of the dot fluctuates between N and $N-1$ and a current flows. This is called the Coulomb blockade, shown

in Fig.3.1. This results in a Coulomb diamond (Fig.3.1) where current is blocked inside the dark diamonds. The conductance peaks occur at the points where the diamonds connect (shown along the direction of the gate voltage axis). This is where the transition from N to $N+1$ occurs.

When we have a DQD with two spins, because of the Pauli exclusion principle, electron transport becomes spin-dependent. Fig.3.2 shows examples of possible spin transport. For a small tunnel coupling between the two dots, the charge stability diagram looks like a checker box pattern rather than the simple diamond shape observed in the case of a single electron quantum dot. Because of the capacitive coupling between the dots and the plunger gates, the charge stability diagrams become a honeycomb. For strong coupling, we see parallel diagonal lines.

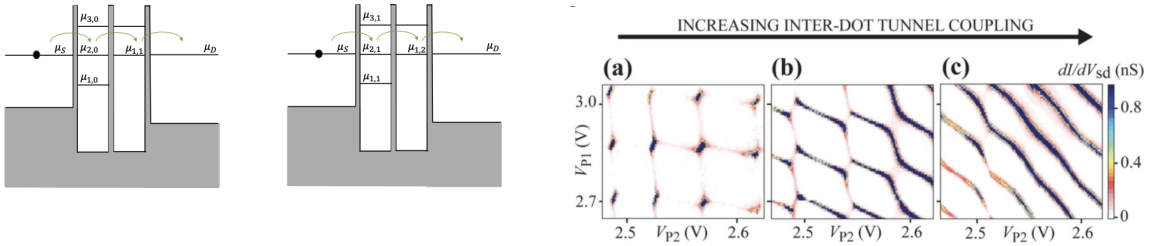

Figure 3.2: Pauli spin blockade and its charge stability diagrams as the tunnel coupling is increased (from left to right, [23]).

3.5 Quantum control of spin qubits

Once spin qubits have been created and initialized, the next step is to implement gate operations to manipulate them. As discussed in section 1.6, a functional quantum computer must at least support a universal set of gate operations. In this section, we explore the physical realizations of single- and two-qubit gates, as well as measurement schemes for spin qubits. As we will see, these operations can be implemented using combinations of electric and magnetic fields.

A gate operation can be represented by a unitary time-evolution, $|\psi(t)\rangle = U(t)\,|\psi(0)\rangle$, where $|\psi(0)\rangle$ is an initial quantum mechanical state and $U(t)$ is a unitary time-dependent operator.

3.5.1 Time-evolution using a static magnetic field

A simple way of physically implementing a single qubit rotation is by applying a static external magnetic field. Recall the time-dependent Schrödinger equation, $i\hbar\frac{d}{dt}\,|\psi(t)\rangle = H(t)\,|\psi(t)\rangle$, where $H(t)$ is the Hamiltonian that describes the system with eigenstates $|\psi(t)\rangle$. Consider the qubit to

be in a static magnetic field, B_z, applied in the z-direction described by the Hamiltonian,

$$H = \frac{\Delta}{2}\sigma_z = \frac{\Delta}{2}\left(|0\rangle\langle 0| - |1\rangle\langle 1|\right). \tag{3.15}$$

The σ_z operation is a Pauli-Z operator with eigenstates $|0\rangle, |1\rangle$ and eigenenergies $E_\pm = \pm\frac{\Delta}{2}$. The magnetic field splits the spin-degenerate states with a splitting $\Delta = g\mu_B B_z$. The initial state at $t = 0$ is $|\psi(0)\rangle = \alpha|0\rangle + \beta|1\rangle$, such that $|\alpha|^2 + |\beta|^2 = 1$. The state at time t is,

$$|\psi(t)\rangle = \alpha e^{-\frac{i\Delta t}{2\hbar}}|0\rangle + \beta e^{\frac{i\Delta t}{2\hbar}}|1\rangle = \begin{pmatrix} \alpha e^{-\frac{i\Delta t}{2\hbar}} \\ \beta e^{\frac{i\Delta t}{2\hbar}} \end{pmatrix}. \tag{3.16}$$

We identity the unitary time-evolution as,

$$\begin{pmatrix} \alpha e^{-\frac{i\Delta t}{2\hbar}} \\ \beta e^{\frac{i\Delta t}{2\hbar}} \end{pmatrix} = \underbrace{\begin{pmatrix} e^{-\frac{i\Delta t}{2\hbar}} & 0 \\ 0 & e^{\frac{i\Delta t}{2\hbar}} \end{pmatrix}}_{U(t)} \begin{pmatrix} \alpha \\ \beta \end{pmatrix} = e^{-\frac{i\Delta t}{2\hbar}} \begin{pmatrix} 1 & 0 \\ 0 & e^{\frac{i\Delta t}{\hbar}} \end{pmatrix} \begin{pmatrix} \alpha \\ \beta \end{pmatrix}. \tag{3.17}$$

The time evolution of our initial state in the Bloch-vector form is,

$$|\psi(t)\rangle = U(t)|\psi(0)\rangle = e^{i\left(\gamma - \frac{\Delta t}{2\hbar}\right)} \begin{pmatrix} \cos\left(\frac{\theta}{2}\right) \\ e^{i\left(\phi - \frac{\Delta t}{2\hbar}\right)} \sin\left(\frac{\theta}{2}\right) \end{pmatrix}. \tag{3.18}$$

This is essentially a rotation of the Bloch state around the z-axis by angle θ and a change in phase to $\phi - \frac{\Delta t}{2\hbar}$. Similar examples can be shown for σ_x and σ_y rotations.

A general Hamiltonian for a magnetic field, B, applied in a direction given by the vector $\boldsymbol{n}$ is, $H = B\left(n_x\sigma_x + n_y\sigma_y + n_z\sigma_z\right) = B\boldsymbol{n}\cdot\boldsymbol{\sigma}$ and its time-evolution operator is, $U(t) = e^{-\frac{iBt}{\hbar}\boldsymbol{n}\cdot\boldsymbol{\sigma}}$. Even though this is a pretty straight-forward application of rotations, it is practically not feasible. We mentioned in chapter 1 that the gate operations must be much faster than the decoherence times of the states. In this case, it is not possible to turn large magnetic fields on and off quickly enough.

3.5.2 Electron spin resonance (ESR)

One way to avoid switching of large magnetic fields is by applying oscillating fields such as microwaves to qubits in a static external field. The Hamiltonian has two parts,

$$H = \frac{\Delta}{2}\sigma_z + B\cos\left(\omega_{ac}t + \phi_{ac}\right)\sigma_x, \tag{3.19}$$

with an oscillation frequency, ω_{ac}. We get a set of differential equations which do not have a simple analytical solution,

$$\begin{aligned} i\hbar\dot{\alpha}(t) &= \frac{\Delta}{2}\alpha(t) + B\cos\left(\omega_{ac}t + \phi_{ac}\right)\beta(t), \\ i\hbar\dot{\beta}(t) &= B\cos\left(\omega_{ac}t + \phi_{ac}\right)\alpha(t) - \frac{\Delta}{2}\beta(t). \end{aligned} \tag{3.20}$$

Using the initial condition $\alpha(0) = 1, \beta(0) = 0, \phi_{ac} = 0, \hbar = \Delta = 1$, we can vary B and $\hbar\omega_{ac}$. We observe clean oscillations when,

- $|\frac{B}{\Delta}| << 1$: oscillating coupling is much weaker than the splitting,
- $\hbar\omega_{ac} \sim \Delta$: oscillating frequency is near or at resonance with the splitting, also known as the resonance condition.

This is explained by the rotating wave approximation (RWA) where the fast oscillating terms can be neglected.

Consider that we are working in the rotating frame with frequency ω. We go to this reference-frame using $U = e^{\omega t\sigma_z/2}$. The Hamiltonian in this reference-frame is,

$$\begin{aligned} \tilde{H}(t) &= U_R^\dagger(t)H(t)U_R(t) - i\hbar\left(U_R^\dagger(t)\frac{d}{dt}U_R(t)\right) \\ &= \frac{1}{2}\begin{pmatrix} \Delta - \hbar\omega & B\left(e^{i(\omega+\omega_{ac})t} + e^{i(\omega-\omega_{ac})t}\right) \\ B\left(\underbrace{e^{-i(\omega+\omega_{ac})t}}_{fast\ term} + \underbrace{e^{-i(\omega-\omega_{ac})t}}_{slow\ term}\right) & -(\underbrace{\Delta - \hbar\omega}_{energy\ shift}) \end{pmatrix}. \end{aligned} \tag{3.21}$$

Neglecting the fast terms and choosing the frame $\omega = \omega_{ac}$,

$$\tilde{H}(t) = \frac{1}{2}\begin{pmatrix} \delta & B \\ B & -\delta \end{pmatrix} = \frac{\hbar}{2}\Omega_{RWA}\boldsymbol{n}_R \cdot \boldsymbol{\sigma}, \tag{3.22}$$

where $\delta = \Delta - \hbar\omega_{ac}, \Omega_R = \frac{\sqrt{\delta^2+B^2}}{\hbar}, \boldsymbol{n}_R = \left(\frac{B}{\hbar\Omega_{RWA}}, 0, \frac{\delta}{\hbar\Omega_{RWA}}\right)$. Setting detuning to 0, $\alpha(0) = 0$, the probability of $|0\rangle$ is, $p_0(t) = |\alpha(t)|^2 = sin^2\left(\frac{B}{2\hbar}t\right)$. One can define a time $T_{flip} = \frac{\pi}{\Omega_R}$ where this probability is 1. Thus applying a microwave pulse for the time T_{flip} one can switch states thus completing a rotation. Similarly, away from resonance one observes a Chevron pattern as shown in Fig.3.3.

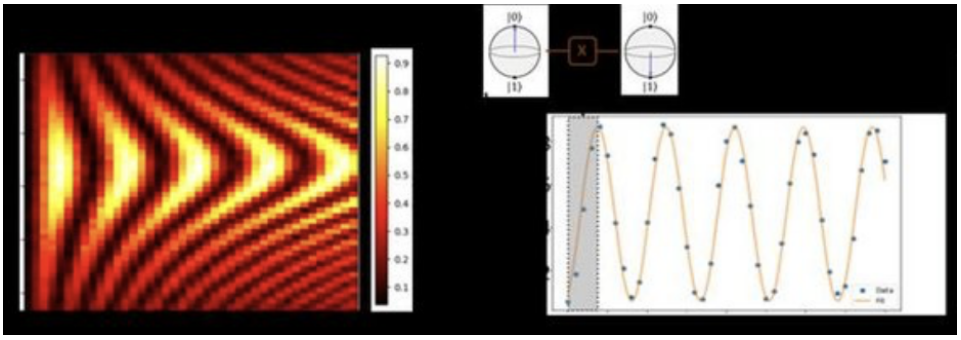

Figure 3.3: Chevron pattern of a single qubit measurement with Rabi-oscillations on application of X gate from [24].

3.5.3 Electron dipole spin resonance (EDSR)

Consider the $1D$ Hamiltonian of an electron with spin-orbit and Zeeman interactions trapped in a harmonic potential as described in section 3.3 with a time dependent electric field, $E_z(t)$[2],

$$H_{1D} = \frac{p_z^2}{2m} - \alpha_R E_x p_z \sigma_y + \frac{g\mu_B B_z}{2}\sigma_z + \frac{m\omega_z^2}{2}z^2 - eE_z(t)z = \frac{p^2}{2m} - \alpha_R E_x p_z \sigma_y + \frac{g\mu_B B_z}{2}\sigma_z + \frac{m\omega_z^2}{2}\left[z - d(t)\right]^2, \tag{3.23}$$

where $d(t) = \frac{eE_z(t)}{m\omega_z^2}$. The Hamiltonian in the orbital rest frame given by a time-dependent translation operator, $T_z\left[d(t)\right] = exp(-ip_z d(t)/\hbar)$,

$$H_{orb,rest} = \frac{p_z^2}{2m} - \alpha_R E_x p_z \sigma_y + \frac{g\mu_B B_z}{2}\sigma_z + \frac{m\omega_z^2}{2}z^2 - p_z\frac{d}{dt}d(t). \tag{3.24}$$

Moving to the spin-rest frame (by a transformation as described in section 3.3), the Hamiltonian is,

$$H_{spin,rest} = \frac{p_z^2}{2m} + \frac{g\mu_B B_z}{2}\left[\cos\left(\frac{2z}{l_{SO}}\right)\sigma_z + \sin\left(\frac{2z}{l_{SO}}\right)\sigma_x\right] + \frac{m\omega_z^2}{2}z^2 - \left[p_z + \frac{\hbar}{l_{SO}}\sigma_y\right]\frac{d}{dt}d(t), \tag{3.25}$$

where l_{SO} is the characteristic spin-orbit length. When the Zeeman and the driving frequencies are much smaller than ω_z, the average of $H_{spin,rest}$ over the groundstate of the harmonic oscillator with the characteristic length, l_z, gives an effective Hamiltonian[3],

$$H_{eff} = E_0 - \sigma_y\frac{\hbar}{l_{SO}}\frac{d}{dt}d(t) + \sigma_z\frac{g\mu_B B_z}{2}e^{l_z^2/l_{SO}^2}. \tag{3.26}$$

In Eq.3.26, we see the appearance of the renormalized g-factor with a dynamic energy term. Essentially, because of the spin-orbit coupling the electron's motion gets coupled to its spin. On applying an electric field we shake the quantum dot and thus the trapped electron, following which the spin flips. At resonance, $\omega_{ac} = g\mu_B B_z exp(l_z^2/l_{SO}^2)/\hbar$, the shaking of the dot induces

[2]Here we "complete the square" and drop the resulting energy term which is equivalent to an overall energy shift.

[3]The order of first going to orbital rest frame and then to the spin rest frame is important otherwise the driving term would not show and it would seem like there is no EDSR.

Rabi oscillations[25, 26],

$$H_{res} = E_0 + \frac{\mu_B}{2} g e^{l_z^2/l_{SO}^2} \left[B_z \sigma_z - B_{SO} \cos\left(\omega_{ac} t\right) \sigma_y \right]. \tag{3.27}$$

This is known as electron dipole spin resonance (EDSR) [25, 27, 28]. The Rabi frequencies in silicon are typically small due to its weak spin-orbit coupling. However, effective spin-orbit interactions can be engineered by introducing magnetic field gradients into the system, often by using micromagnets.

3.6 Two qubit gates

Two qubit gates can be described as a time-evolution of the Hamiltonian, H_{ST}, from Eq.3.8 which describes the singlet-triplet system in a DQD with the unitary[4],

$$U_{2Q} = M^T e^{-iH_{ST}t/\hbar} M = \begin{pmatrix} e^{-i\frac{g\mu_B B_z t}{\hbar}} & 0 & 0 & 0 \\ 0 & e^{i\frac{Jt}{2\hbar}} \cos\left(Jt/2\hbar\right) & -ie^{i\frac{Jt}{2\hbar}} \sin\left(Jt/2\hbar\right) & 0 \\ 0 & -ie^{i\frac{Jt}{2\hbar}} \sin\left(Jt/2\hbar\right) & e^{i\frac{Jt}{2\hbar}} \cos\left(Jt/2\hbar\right) & 0 \\ 0 & 0 & 0 & e^{i\frac{g\mu_B B_z t}{\hbar}} \end{pmatrix}, \tag{3.28}$$

with the exchange interaction, J, where,

$$e^{-iH_{ST}t/\hbar} = \begin{pmatrix} e^{-\frac{g\mu_B B_z t}{\hbar}} & 0 & 0 & 0 \\ 0 & e^{-i\frac{Jt}{\hbar}} & 0 & 0 \\ 0 & 0 & 1 & 0 \\ 0 & 0 & 0 & e^{i\frac{g\mu_B B_z}{\hbar}} \end{pmatrix}. \tag{3.29}$$

3.6.1 SWAP gate

From Eq. 3.28, it becomes clear that a pure SWAP gate cannot be directly applied to two qubits. However, by turning on the exchange interaction J for a duration $t = T_{SWAP} = \frac{\pi\hbar}{J}$, the resulting unitary evolution,

$$U_{2Q}(T_{SWAP}) = \begin{pmatrix} e^{-i\frac{g\mu_B B_z t}{\hbar}} & 0 & 0 & 0 \\ 0 & 0 & 1 & 0 \\ 0 & 1 & 0 & 0 \\ 0 & 0 & 0 & e^{i\frac{g\mu_B B_z t}{\hbar}} \end{pmatrix} = e^{-i\frac{g\mu_B B_z T_{SWAP}}{2\hbar}\sigma_z^{(1)}} e^{-i\frac{g\mu_B B_z T_{SWAP}}{2\hbar}\sigma_z^{(2)}} SWAP, \tag{3.30}$$

is closely related to a SWAP operation, effectively acting like a π-pulse, up to some single-qubit rotations.

[4]The basis transformation using M has been described in section 3.2.4.

Similarly, $\sqrt{SWAP}$ operator can also be implemented by turning on the interaction J for $T_{\sqrt{SWAP}} = \frac{\pi\hbar}{2J}$, such that $U_{2Q}(T_{\sqrt{SWAP}}) = e^{-i\frac{g\mu_B B_z T_{\sqrt{SWAP}}}{2\hbar}\sigma_z^{(1)}} e^{-i\frac{g\mu_B B_z T_{\sqrt{SWAP}}}{2\hbar}\sigma_z^{(2)}} \sqrt{SWAP}$. The exchange interaction naturally leads to a $SWAP/\sqrt{SWAP}$ gate. One needs to keep in mind that the exchange interaction cannot be switched on and off instantaneously. The error caused by this can be minimized by correcting the shape of the pulse [29]. Calibrating gate times can also minimize non-adiabatic effects [30].

3.6.2 CZ gate

The unitary evolution for $CNOT$ and CZ gates can be written in terms of the $SWAP$ gates,

$$\begin{aligned} &e^{-i\frac{\pi}{4}\sigma_z^{(1)}} e^{i\frac{\pi}{4}\sigma_z^{(2)}} U_{\sqrt{SWAP}} e^{-i\frac{\pi}{2}\sigma_z^{(1)}} U_{\sqrt{SWAP}} = -iU_{CZ}, \\ &e^{i\frac{\pi}{4}\sigma_z^{(1)}} e^{-i\frac{\pi}{4}\sigma_z^{(2)}} U^3_{\sqrt{SWAP}} e^{i\frac{\pi}{2}\sigma_z^{(1)}} U^3_{\sqrt{SWAP}} = iU_{CZ}, \\ &e^{-i\frac{\pi}{4}\sigma_z^{(2)}} U_{CZ} e^{i\frac{\pi}{4}\sigma_z^{(1)}} = U_{CNOT}. \end{aligned} \tag{3.31}$$

But since two qubit gate fidelities are lower than single qubit gate fidelity, we would like to minimize the number of two qubit gates to 1.

Consider the Ising type of interaction, $H_{Ising} = -\frac{J}{4}\sigma_z^{(1)}\sigma_z^{(2)} + \frac{J}{4}$. The unitary evolution for this Hamiltonian is,

$$U_{ising}(t) = \begin{pmatrix} 1 & 0 & 0 & 0 \\ 0 & e^{i\frac{J}{2\hbar}t} & 0 & 0 \\ 0 & 0 & e^{i\frac{J}{2\hbar}t} & 0 \\ 0 & 0 & 0 & 1 \end{pmatrix}. \tag{3.32}$$

Then we can get the CZ gate by applying a single two-qubit unitary [31],

$$CZ = e^{-i\frac{3\pi}{2}} e^{-i\frac{\pi}{4}\sigma_z^{(1)}} e^{-i\frac{\pi}{4}\sigma_z^{(2)}} U_{Ising}(\pi\hbar/J). \tag{3.33}$$

3.6.3 CNOT gate

One way to apply the CNOT gate is by creating a g-factor difference between the two dots such that the two qubits have different Zeeman energies rather than applying many $SWAP$ gates [32–36],

$$H^{\omega}_{2Q} = \frac{E_z^{(1)}}{2}\sigma_z^{(1)} + \frac{E_z^{(2)}}{2}\sigma_z^{(2)} + \frac{J}{4}\left(\boldsymbol{\sigma^{(1)}} \cdot \boldsymbol{\sigma^{(2)}} - 1\right) + \nu^{(2)}\cos(\omega t)\sigma_x^{(2)}. \tag{3.34}$$

In the limit where, $J << |E_z^{(1)} - E_z^{(2)}|$,

$$H_{2Q}^{\omega} = \begin{pmatrix} \frac{E_z^{(1)}+E_z^{(2)}}{2} & \nu^{(2)}\cos(\omega t) & 0 & 0 \\ \nu^{(2)}\cos(\omega t) & \frac{E_z^{(1)}-E_z^{(2)}-J}{2} & 0 & 0 \\ 0 & 0 & \frac{-E_z^{(1)}+E_z^{(2)}+J}{2} & \nu^{(2)}\cos(\omega t) \\ 0 & 0 & \nu^{(2)}\cos(\omega t) & \frac{-E_z^{(1)}-E_z^{(2)}}{2} \end{pmatrix}. \tag{3.35}$$

The upper and the lower blocks of H_{2Q}^{ω} have different resonant condisiton:

$$\begin{aligned} \hbar\omega &= \frac{-E_z^{(1)} + E_z^{(2)} + J}{2} - \frac{-E_z^{(1)} - E_z^{(2)}}{2} = \frac{E_z^{(2)} - J}{2} : lower, \\ \hbar\omega &= \frac{E_z^{(1)} + E_z^{(2)}}{2} - \frac{E_z^{(1)} - E_z^{(2)} - J}{2} = \frac{E_z^{(2)} + J}{2} : upper. \end{aligned} \tag{3.36}$$

So we drive on resonance in the lower block 3.36 and remain off-resonant in the upper one, we see the $CNOT$ gate emerging. Turning on $\nu^{(2)}$ for a time $T_\pi = \frac{\pi\hbar}{\nu^{(2)}}$, we get the $CNOT$ gate.

In the previous approach, the effect of spin-orbit interaction was not included. The spin-orbit interaction induces a strong anisotropy in the exchange interaction. We maintain that the two dots have different g-factors, $g_{L,R} = g \pm \delta g$. This leads to the following single electron Hamiltonian (recall this is an extension of the charge qubit Hamiltonian from Eq.3.2),

$$H_{1e} = \frac{\epsilon}{2}\tau_z - t_0\tau_x + \frac{g\mu_B B_z}{2}\sigma_z + \frac{\delta g\mu_B B_z}{2}\tau_z\sigma_z - t_{SO}\tau_y\sigma_y. \tag{3.37}$$

with tunneling rate t_0, the detuning between the dots ϵ and the spin-orbit strength t_{SO}. From this, we extract the double dot Hamiltonian, H_{DQD}, as done at the start of this section. As shown in section 3.3, we apply a local spin rotation $U = exp(iL\tau_z\sigma_y/2l_{SO})$, $\tilde{H}_{DQD} = U^\dagger H_{DQD} U$ with the inter-dot distance L. Identifying and eliminating the high energy states that involve both the electrons on the same QD and writing this Hamiltonian in the computational basis,

$$H_{2Q} = \frac{E_z^{(1)}}{2}\sigma_z^{(1)} + \frac{E_z^{(2)}}{2}\sigma_z^{(2)} + \frac{J}{4}\boldsymbol{\sigma}^{(1)} \cdot R_y\left(-\frac{2L}{l_{SO}}\right)\boldsymbol{\sigma}^{(2)}. \tag{3.38}$$

The term $\frac{J}{4}\boldsymbol{\sigma}^{(1)} \cdot R_y\left(-\frac{2L}{l_{SO}}\right)\boldsymbol{\sigma}^{(2)}$ shows the anisotropy in the exchange interaction [36]. This allows for more direct application of the controlled gates and we can avoid the $SWAP$ and $\sqrt{SWAP}$ gates altogether.

3.7 Coherence and noise in spin-qubits

One of the major challenges in realizing large scale quantum computers is noise. The effects of noise on spin qubits is characterized by two phenomena: dephasing and relaxation. In this section we explore the effects of dephasing in depth and discuss possible ways to mitigate them.

3.7.1 Dephasing

The dephasing of a qubit can be determined by letting the qubit evolve freely in time. We start with a qubit in the $|0\rangle$ (or $|1\rangle$) state. We bring it into a superposition $|+\rangle = \frac{1}{2}(|0\rangle + |1\rangle)$ $\left(\text{or}|-\rangle = \frac{1}{2}(|0\rangle - |1\rangle)\right)$ by applying a $\pi/2$-pulse for $T_{\pi/2} = \frac{\pi}{2\Omega_R}$ using a microwave. We then let the state time evolve freely,

$$|\psi(t)\rangle = e^{-i\frac{\Delta t}{2\hbar}\sigma_z}|+\rangle = \cos\left(\frac{\Delta t}{2\hbar}\right)|+\rangle - i\sin\left(\frac{\Delta t}{2\hbar}\right)|-\rangle = e^{-i\frac{\Delta t}{2\hbar}}\frac{|0\rangle + e^{i\frac{\Delta t}{\hbar}}|1\rangle}{\sqrt{2}}. \tag{3.39}$$

In the ideal case the probability of finding state in one or the other state oscillates and must be a cosine or a sine function, $P_1 = \cos\left(\frac{\Delta t}{2\hbar}\right)^2$. But in reality we see that the probability decays [37]. This is due to the fluctuations in the splitting Δ with time which can be caused by other effects such as charge noise, phonons or nuclear spins. Since we are averaging over many measurements to obtain the fidelity, we see a decay over the average of the oscillations.

We can model these time-dependent random contributions to the energy gap into the Hamiltonian,

$$H = \frac{\Delta + R(t)}{2}\sigma_z, \tag{3.40}$$

such that $\langle R(t)\rangle = 0$ but the correlation function $G_{RR}(t-t') = \langle R(t)R(t')\rangle \neq 0$. The form of this correlation function determines the kind of decay that the probability suffers. We generally look at the spectral function which is a Fourier transform of the correlation function,

$$S_{RR}(\omega) = \int_{-\infty}^{+\infty} dt e^{i\omega t} G_{RR}(t) = \int_{-\infty}^{+\infty} dt e^{i\omega t}\langle R(t)R(0)\rangle \tag{3.41}$$

because it is the spectral function that can be experimentally measured. We consider the noise to be classical $S_{RR}(\omega) = S_{RR}(-\omega)$. The time-evolved state would then have the coefficients,

$$\begin{aligned}\alpha(t) &= \alpha_0 \exp\left(-i\frac{\Delta t}{2\hbar} - \frac{i}{2\hbar}\int_0^t dt' R(t')\right),\\ \beta(t) &= \beta_0 \exp\left(i\frac{\Delta t}{2\hbar} + \frac{i}{2\hbar}\int_0^t dt' R(t')\right),\end{aligned} \tag{3.42}$$

where $\delta\phi = \frac{1}{\hbar}\int_0^t dt' R(t')$. This changes the probability,

$$P_1 = \frac{1}{2} + \frac{1}{2}\cos\left(\frac{\Delta t}{\hbar} + \delta\phi\right). \tag{3.43}$$

This is the probability for a single-shot measurement. We assume that over a large set of measurements the phase $\delta\phi$ is normally distributed with the distribution $p_{\delta\phi} = \frac{1}{\sqrt{2\pi\sigma_{\delta\phi}}} e^{-\frac{\delta\phi^2}{2\sigma_{\delta\phi}}}$. The expectation value of the probability over many measurements is,

$$\begin{aligned} P_1 &= \frac{1}{2} + \frac{1}{2} e^{-\frac{\sigma_{\delta\phi}}{2}} \cos\left(\frac{\Delta t}{\hbar}\right), \\ \sigma_{\delta\phi} &= \frac{1}{2\pi\hbar^2} \underbrace{\int_0^t dt' \int_0^t dt'' \int_{-\infty}^{+\infty} d\omega e^{-i\omega(t'-t'')} S_{RR}(\omega)}_{F(\omega t) = \int_{-\infty}^{+\infty} d\omega \frac{4\sin^2(\omega t/2)}{\omega^2}}. \end{aligned} \tag{3.44}$$

$F(\omega t)$ is called a filter function and depends on the experiment (in the case of Ramsey, it is free evolution). This function peaks at zero frequency and is close to maximum for low frequencies. The table below 3.1 shows the correlation functions of a set of noise commonly considered, Quasi-static noise arises primarily from hyperfine interactions, pink noise typically originates

Type of noise	Correlation function
Quasi-static noise	$S_{RR}(\omega) = \frac{2\pi\hbar^2}{(T_2^*)^2}\delta(\omega)$
Pink noise	$S_{RR}(\omega) = \frac{\hbar^2}{(T_2^*)^2\lvert\omega\rvert^2}$
White noise	$S_{RR}(\omega) = \frac{\hbar^2}{T_2^*}$

Table 3.1: Types of noise and their correction functions.

from charge fluctuations, and white noise represents uncorrelated noise. T_2^* is called the dephasing time or the time at which the decay envelop reaches $1/e$ of its original value. It is usually much larger than the $T_2^* << T_2$ decoherence time since it is almost an average of the latter over large number of experiments. The decoherence rate is $\frac{1}{T_2} = \frac{1}{2T_1} + \frac{1}{T_2^*}$ where T_1 relaxation time is the time a higher energy state takes to relax to a lower energy one), $T_2 << 2T_1$.

There are several strategies to mitigate the effects of noise in spin qubits. Quasi-static noise arising from hyperfine interactions can be significantly reduced in materials like silicon and germanium by isotopic purification. Another effective approach is to operate the system at "sweet spots" which are specific regimes where the energy splitting Δ loses sensitivity to fluctuations in control parameters, thus enhancing coherence. Additionally, since the filter function depends on

the experimental pulse sequence, noise can be suppressed by shaping this function to minimize sensitivity at low frequencies. This technique, known as dynamical decoupling, is particularly effective against slow noise.

The Hahn experiment allows to obtain such a filter function. In this experiment, similar to Ramsey, we bring the initial state $|0\rangle$ into a superposition $\frac{1}{\sqrt{2}}(|0\rangle + |1\rangle)$ using a $\pi/2$-pulse. Now, instead of waiting for the state to evolve, we apply a π-pulse. This pulse refocuses the state. We then let the system freely evolve and apply a $\pi/2$-pulse to measure the outcome.

$$|\psi(0)\rangle = \frac{1}{\sqrt{2}}(|0\rangle + |1\rangle) \rightarrow |\psi(t<\tau)\rangle = \frac{1}{\sqrt{2}}\left(|0\rangle + e^{\frac{i\Delta t}{\hbar}}|1\rangle\right) \rightarrow |\psi(t=\tau)\rangle = \frac{1}{\sqrt{2}}\left(|1\rangle + e^{\frac{i\Delta t}{\hbar}}|0\rangle\right)$$
$$\rightarrow |\psi(t>\tau\rangle = \frac{1}{\sqrt{2}}\left(e^{\frac{i\hbar(t-\tau)}{\hbar}}|1\rangle + e^{\frac{i\Delta\tau}{\hbar}}|0\rangle\right) = \frac{1}{\sqrt{2}}\left(|0\rangle + e^{\frac{i\Delta(t-2\tau)}{\hbar}}|1\rangle\right) \rightarrow |\psi(2\tau)\rangle = \frac{1}{\sqrt{2}}(|0\rangle + |1\rangle), \tag{3.45}$$

with the probability, $\langle P_1\rangle = \frac{1}{2} + \frac{1}{2}\exp\left(-\frac{\sigma_{\delta\phi}}{2}\cos\left(\frac{2\Delta\tau}{\hbar}\right)\right)$ and $\sigma_{\delta\phi} = \frac{1}{2\pi\hbar}\int_{-\infty}^{+\infty} d\omega \frac{F_{Hahn}}{\omega^2}(\omega\tau)S_{RR}(\omega)$ where $F_{Hahn}(\omega) = 16\sin^4\left(\frac{\omega\tau}{4}\right)$ which is zero at zero-frequency. A list of other filter functions that can be used is given in [38].

3.8 Challenges and future perspectives

Spin qubits face several technical challenges when it comes to scaling. One of the major issues for silicon is the valley degeneracy where the electrons in silicon occupy multiple conduction band valley states which have the same energies. The confinement of electrons lifts this degeneracy in a way that the amount of valley splitting depends on the length of the confinement. But the splitting between these states is similar to the size of the Zeeman splitting and could interfere with the spin-degree of freedom and cause decoherence [39]. Small valley splitting also makes it difficult to read out the qubits. Furthermore, it can thermally excite the qubits [40] and also results in valley dependent g-factor. One way around this problem is by using strain and electric fields together to induce larger valley splitting [41]. By introducing a certain concentration of germanium in the silicon sandwiched between the two other layers, one creates a wiggle well architecture which makes it possible to couple different valley states in the z-direction together [42].

Other challenges faced in scaling up spin qubits is the amount of control electronics needed for each qubit. This can be countered by using a crossbar architecture which involves using horizontal and vertical control lines where qubits can be addressed at the intersection. This allows for a parallel control and readout. One needs to be careful of crosstalk between the lines and of reaching the intended qubit. This, along with the CMOS architecture, that leverages the way in which the classical chips are currently mass-produced, makes it easier to adopt to large scale industry

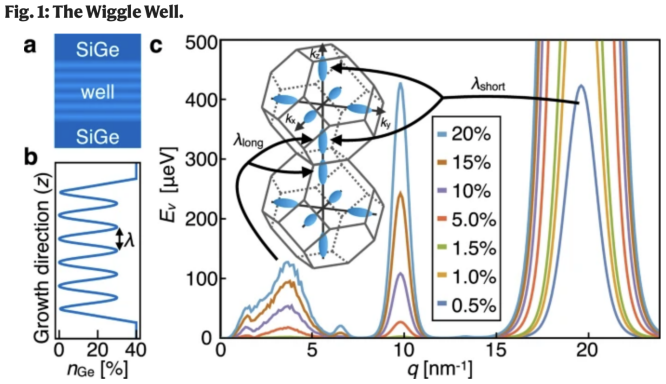

Figure 3.4: The figure shows the wiggle well architecture. a) shows a Si/SiGe heterostructure with 15% Ge concentration in the Si layer, b) shows the appearance of wiggles in the quantum well with a wavelength λ due to the 15% Ge, c) shows the coupling of the valley states in the z-direction for the respective wavevector $q = 2\pi/\lambda$: for a short wavevector the valley states in different BZ are coupled whereas for a long wavevector valley states in the same BZ are coupled. Image from [42]

fabrication. But it is challenging to maintain qubit coherence and control. With the crossbar technology, a 16 qubit array has also been demonstrated [43].

No doubt that semiconductor spin qubits are the leading candidate for scalable quantum computing, but before implementing advanced quantum algorithms, it is important to develop a robust and high-performing qubit architecture. Among the parameters that influence the performance of these qubits is the electron g-factor. As seen so far, it plays a significant role in gate operations, qubit control, and sensitivity to noise. In this thesis, and in the following chapters, we focus on developing a comprehensive understanding of the g-factor and its microscopic origins, so that informed strategies can be implemented to optimize device performance.

Bibliography

[1] Paul Steinacker, Nard Dumoulin Stuyck, Wee Han Lim, Tuomo Tanttu, MengKe Feng, Andreas Nickl, Santiago Serrano, Marco Candido, Jesus D. Cifuentes, Fay E. Hudson, Kok Wai Chan, Stefan Kubicek, Julien Jussot, Yann Canvel, Sofie Beyne, Yosuke Shimura, Roger Loo, Clement Godfrin, Bart Raes, Sylvain Baudot, Danny Wan, Arne Laucht, Chih Hwan Yang, Andre Saraiva, Christopher C. Escott, Kristiaan De Greve, and Andrew S. Dzurak. A 300 mm foundry silicon spin qubit unit cell exceeding 99 2024. URL https://arxiv.org/abs/2410.15590.

[2] Tsuneya Ando, Alan B. Fowler, and Frank Stern. Electronic properties of two-dimensional systems. *Rev. Mod. Phys.*, 54:437–672, Apr 1982. doi: 10.1103/RevModPhys.54.437. URL https://link.aps.org/doi/10.1103/RevModPhys.54.437.

[3] Richard Arthur Abram and Milan Jaros. *Band Structure Engineering in Semiconductor Microstructures*, volume 189. Springer Science & Business Media, 2012.

[4] Gérald Bastard, JA Brum, and R Ferreira. Electronic states in semiconductor heterostructures. In *Solid State Physics*, volume 44, pages 229–415. Elsevier, 1991.

[5] Leo P Kouwenhoven, DG Austing, and Seigo Tarucha. Few-electron quantum dots. *Reports on progress in physics*, 64(6):701, 2001.

[6] Wilfred G Van der Wiel, Silvano De Franceschi, Jeroen M Elzerman, Toshimasa Fujisawa, Seigo Tarucha, and Leo P Kouwenhoven. Electron transport through double quantum dots. *Reviews of modern physics*, 75(1):1, 2002.

[7] Marc A Kastner. The single-electron transistor. *Reviews of modern physics*, 64(3):849, 1992.

[8] Daniel Loss and David P. DiVincenzo. Quantum computation with quantum dots. *Phys. Rev. A*, 57:120–126, Jan 1998. doi: 10.1103/PhysRevA.57.120. URL https://link.aps.org/doi/10.1103/PhysRevA.57.120.

[9] F. H. L. Koppens, K. C. Nowack, and L. M. K. Vandersypen. Spin echo of a single electron spin in a quantum dot. *Phys. Rev. Lett.*, 100:236802, Jun 2008. doi: 10.1103/PhysRevLett.100.236802. URL https://link.aps.org/doi/10.1103/PhysRevLett.100.236802.

[10] Jarryd J Pla, Kuan Y Tan, Juan P Dehollain, Wee H Lim, John JL Morton, David N Jamieson, Andrew S Dzurak, and Andrea Morello. A single-atom electron spin qubit in silicon. *Nature*, 489(7417):541–545, 2012.

[11] M Veldhorst, JCC Hwang, CH Yang, AW Leenstra, Bob de Ronde, JP Dehollain, JT Muhonen, FE Hudson, Kohei M Itoh, A t Morello, et al. An addressable quantum dot qubit with fault-tolerant control-fidelity. *Nature nanotechnology*, 9(12):981–985, 2014.

[12] KC Nowack, M Shafiei, M Laforest, GEDK Prawiroatmodjo, LR Schreiber, C Reichl, W Wegscheider, and LMK Vandersypen. Single-shot correlations and two-qubit gate of solid-state spins. *Science*, 333(6047):1269–1272, 2011.

[13] Menno Veldhorst, CH Yang, JCCea Hwang, W Huang, JP Dehollain, JT Muhonen, S Simmons, A Laucht, FE Hudson, Kohei M Itoh, et al. A two-qubit logic gate in silicon. *Nature*, 526(7573):410–414, 2015.

[14] Bruce E Kane. A silicon-based nuclear spin quantum computer. *nature*, 393(6681):133–137, 1998.

[15] Jeremy Levy. Universal quantum computation with spin-1/2 pairs and heisenberg exchange. *Phys. Rev. Lett.*, 89:147902, Sep 2002. doi: 10.1103/PhysRevLett.89.147902. URL https://link.aps.org/doi/10.1103/PhysRevLett.89.147902.

[16] Semiconductor Quantum Dots. Coherent manipulation of coupled electron spins in. *condensed-matter physics*, 5:6. URL https://qudev.phys.ethz.ch/static/content/courses/QSIT10/pdfs/Petta2005.pdf.

[17] Yu A Bychkov and E I Rashba. Oscillatory effects and the magnetic susceptibility of carriers in inversion layers. *Journal of Physics C: Solid State Physics*, 17(33):6039, nov 1984. doi: 10.1088/0022-3719/17/33/015. URL https://dx.doi.org/10.1088/0022-3719/17/33/015.

[18] Olesia Dmytruk, Denis Chevallier, Daniel Loss, and Jelena Klinovaja. Renormalization of the quantum dot g-factor in superconducting rashba nanowires. *Phys. Rev. B*, 98:165403, Oct 2018. doi: 10.1103/PhysRevB.98.165403. URL https://link.aps.org/doi/10.1103/PhysRevB.98.165403.

[19] F. N. M. Froning, M. J. Rančić, B. Hetényi, S. Bosco, M. K. Rehmann, A. Li, E. P. A. M. Bakkers, F. A. Zwanenburg, D. Loss, D. M. Zumbühl, and F. R. Braakman. Strong spin-orbit interaction and g-factor renormalization of hole spins in ge/si nanowire quantum dots. *Phys. Rev. Res.*, 3:013081, Jan 2021. doi: 10.1103/PhysRevResearch.3.013081. URL https://link.aps.org/doi/10.1103/PhysRevResearch.3.013081.

[20] M. A. Toloza Sandoval, J. E. Leon Padilla, A. Ferreira da Silva, E. A. de Andrada e Silva, and G. C. La Rocca. Mesoscopic g-factor renormalization for electrons in iii-v interacting nanolayers. *Phys. Rev. B*, 98:075312, Aug 2018. doi: 10.1103/PhysRevB.98.075312. URL https://link.aps.org/doi/10.1103/PhysRevB.98.075312.

[21] E. A. Zhukov, V. N. Mantsevich, D. R. Yakovlev, N. E. Kopteva, E. Kirstein, A. Waag, G. Karczewski, T. Wojtowicz, and M. Bayer. Renormalization of the electron g factor in the degenerate two-dimensional electron gas of znse- and cdte-based quantum wells. *Phys. Rev. B*, 102:125306, Sep 2020. doi: 10.1103/PhysRevB.102.125306. URL https://link.aps.org/doi/10.1103/PhysRevB.102.125306.

[22] K. I. Bolotin, F. Kuemmeth, A. N. Pasupathy, and D. C. Ralph. Metal-nanoparticle single-electron transistors fabricated using electromigration. *Applied Physics Letters*, 84(16):3154–3156, 04 2004. ISSN 0003-6951. doi: 10.1063/1.1695203. URL https://doi.org/10.1063/1.1695203.

[23] NS Lai, WH Lim, CH Yang, FA Zwanenburg, WA Coish, F Qassemi, A Morello, and AS Dzurak. Pauli spin blockade in a highly tunable silicon double quantum dot. *Scientific reports*, 1(1):110, 2011. URL https://www.nature.com/articles/srep00110.

[24] Thorsten Last, Nodar Samkharadze, Pieter Eendebak, Richard Versluis, Xiao Xue, Amir Sammak, Delphine Brousse, Kelvin Loh, Henk Polinder, Giordano Scappucci, Menno Veldhorst, Lieven Vandersypen, Klara Maturova, Jeremy Veltin, and Garrelt Alberts. Quantum inspire: Qutech's platform for co-development and collaboration in quantum computing. page 17, 03 2020. doi: 10.1117/12.2551853.

[25] Vitaly N. Golovach, Massoud Borhani, and Daniel Loss. Electric-dipole-induced spin resonance in quantum dots. *Phys. Rev. B*, 74:165319, Oct 2006. doi: 10.1103/PhysRevB.74.165319. URL https://link.aps.org/doi/10.1103/PhysRevB.74.165319.

[26] Erika Kawakami, Pasquale Scarlino, Daniel R Ward, FR Braakman, DE Savage, MG Lagally, Mark Friesen, Susan N Coppersmith, Mark A Eriksson, and LMK Vandersypen. Electrical control of a long-lived spin qubit in a si/sige quantum dot. *Nature nanotechnology*, 9(9):666–670, 2014. URL https://www.nature.com/articles/nnano.2014.153.

[27] Emmanuel I. Rashba. Theory of electric dipole spin resonance in quantum dots: Mean field theory with gaussian fluctuations and beyond. *Phys. Rev. B*, 78:195302, Nov 2008. doi: 10.1103/PhysRevB.78.195302. URL https://link.aps.org/doi/10.1103/PhysRevB.78.195302.

[28] Julian D. Teske, Friederike Butt, Pascal Cerfontaine, Guido Burkard, and Hendrik Bluhm. Flopping-mode electron dipole spin resonance in the strong-driving regime. *Phys. Rev. B*, 107:035302, Jan 2023. doi: 10.1103/PhysRevB.107.035302. URL https://link.aps.org/doi/10.1103/PhysRevB.107.035302.

[29] Ming Ni, Rong-Long Ma, Zhen-Zhen Kong, Xiao Xue, Sheng-Kai Zhu, Chu Wang, Ao-Ran Li, Ning Chu, Wei-Zhu Liao, Gang Cao, Gui-Lei Wang, Guang-Can Guo, Xuedong Hu, Hong-Wen Jiang, Hai-Ou Li, and Guo-Ping Guo. A swap gate for spin qubits in silicon, 2023. URL https://arxiv.org/abs/2310.06700.

[30] Stefano Bosco, Pasquale Scarlino, Jelena Klinovaja, and Daniel Loss. Fully tunable longitudinal spin-photon interactions in si and ge quantum dots. *Phys. Rev. Lett.*, 129:066801, Aug 2022. doi: 10.1103/PhysRevLett.129.066801. URL https://link.aps.org/doi/10.1103/PhysRevLett.129.066801.

[31] David P. DiVincenzo. Topics in quantum computers, 1996. URL https://arxiv.org/abs/cond-mat/9612126.

[32] David M Zajac, Anthony J Sigillito, Maximilian Russ, Felix Borjans, Jacob M Taylor, Guido Burkard, and Jason R Petta. Resonantly driven cnot gate for electron spins. *Science*, 359(6374): 439–442, 2018. URL https://www.science.org/doi/full/10.1126/science.aao5965.

[33] Luca Petit, HGJ Eenink, M Russ, WIL Lawrie, NW Hendrickx, SGJ Philips, JS Clarke, LMK Vandersypen, and M Veldhorst. Universal quantum logic in hot silicon qubits. *Nature*, 580 (7803):355–359, 2020. URL https://www.nature.com/articles/s41586-020-2170-7.

[34] Nico W Hendrickx, William IL Lawrie, Maximilian Russ, Floor van Riggelen, Sander L de Snoo, Raymond N Schouten, Amir Sammak, Giordano Scappucci, and Menno Veldhorst. A four-qubit germanium quantum processor. *Nature*, 591(7851):580–585, 2021. URL https://www.nature.com/articles/s41586-021-03332-6.

[35] Akito Noiri, Kenta Takeda, Takashi Nakajima, Takashi Kobayashi, Amir Sammak, Giordano Scappucci, and Seigo Tarucha. Fast universal quantum gate above the fault-tolerance threshold in silicon. *Nature*, 601(7893):338–342, 2022. URL https://www.nature.com/articles/s41586-021-04182-y.

[36] Simon Geyer, Bence Hetényi, Stefano Bosco, Leon C. Camenzind, Rafael S. Eggli, Andreas Fuhrer, Daniel Loss, Richard J. Warburton, Dominik M. Zumbühl, and Andreas V. Kuhlmann. Anisotropic exchange interaction of two hole-spin qubits. *Nature Physics*, 20(7): 1152–1157, May 2024. ISSN 1745-2481. doi: 10.1038/s41567-024-02481-5. URL http://dx.doi.org/10.1038/s41567-024-02481-5.

[37] Dohun Kim, Daniel R Ward, Christie B Simmons, Don E Savage, Max G Lagally, Mark Friesen, Susan N Coppersmith, and Mark A Eriksson. High-fidelity resonant gating of a silicon-based quantum dot hybrid qubit. *Npj Quantum Information*, 1(1):1–6, 2015. URL https://www.nature.com/articles/npjqi20154.

[38] Łukasz Cywiński, Roman M. Lutchyn, Cody P. Nave, and S. Das Sarma. How to enhance dephasing time in superconducting qubits. *Phys. Rev. B*, 77:174509, May 2008. doi: 10.1103/PhysRevB.77.174509. URL https://link.aps.org/doi/10.1103/PhysRevB.77.174509.

[39] F. Borjans, D.M. Zajac, T.M. Hazard, and J.R. Petta. Single-spin relaxation in a synthetic spin-orbit field. *Phys. Rev. Appl.*, 11:044063, Apr 2019. doi: 10.1103/PhysRevApplied.11.044063. URL https://link.aps.org/doi/10.1103/PhysRevApplied.11.044063.

[40] Chih Heng Yang, RCC Leon, JCC Hwang, Andre Saraiva, Tuomo Tanttu, Wister Huang, Julien Camirand Lemyre, Kok Wai Chan, KY Tan, Fay E Hudson, et al. Operation of a silicon quantum processor unit cell above one kelvin. *Nature*, 580(7803):350–354, 2020. URL https://www.nature.com/articles/s41586-020-2171-6.

[41] Floris A. Zwanenburg, Andrew S. Dzurak, Andrea Morello, Michelle Y. Simmons, Lloyd C. L. Hollenberg, Gerhard Klimeck, Sven Rogge, Susan N. Coppersmith, and Mark A. Eriksson. Silicon quantum electronics. *Rev. Mod. Phys.*, 85:961–1019, Jul 2013. doi: 10.1103/RevModPhys.85.961. URL https://link.aps.org/doi/10.1103/RevModPhys.85.961.

[42] Thomas McJunkin, Benjamin Harpt, Yi Feng, Merritt P Losert, Rajib Rahman, JP Dodson, MA Wolfe, DE Savage, MG Lagally, SN Coppersmith, et al. Sige quantum wells with oscillating ge concentrations for quantum dot qubits. *Nature Communications*, 13(1):7777, 2022. doi: 10.1038/s41467-022-35510-z. URL https://doi.org/10.1038/s41467-022-35510-z.

[43] Francesco Borsoi, Nico W Hendrickx, Valentin John, Marcel Meyer, Sayr Motz, Floor Van Riggelen, Amir Sammak, Sander L De Snoo, Giordano Scappucci, and Menno Veldhorst. Shared control of a 16 semiconductor quantum dot crossbar array. *Nature Nanotechnology*, 19 (1):21–27, 2024. URL https://www.nature.com/articles/s41565-023-01491-3#citeas.

4

The Theory of g-factors

4.1 Introduction

For a charged particle such as an electron, the intrinsic spin along with the charge contribute to its magnetic moment. The magnetic moment helps determine the strength and direction of the magnetic field of the particle, thus giving an insight into its behavior in an external field. The g-factor helps quantify the coupling of the particle's intrinsic spin to an external field. In particle physics, it is known that the Standard Model theory is incomplete. The magnetic moment (g-factor) is precisely measured and is one of the accurately verified predictions of the standard model. These measurements are exciting because they have a potential role in the search of theories beyond the Standard Model [1].

In solid state physics also the electron g-factor is an important quantity which can predict the behavior of electrons in specific quantum setups and to some extent even help control its spin. In section.3.5 of chapter 3, we saw that in spin-qubit quantum computer, single qubit gates can be implemented using static fields and oscillating fields [2–4]. The effect of this can be directly noted by measuring the g-factor. The modulation of the g-factor leads directly to spin-manipulation [5]. In the case of a double quantum dot (DQD) as well, single-qubit gates involves the g-factor difference between the two dot [6–9]. The sensitivity of the g-factor to the shape of a quantum dot (QD) can help understand the QD properties, the device physics and thus the qubit performance [10]. We saw in chapter 3 that the g-factor can also be informative about the noise.

In this chapter, we discuss a general theory of the $\boldsymbol{g}$-tensor and provide explicit analytical methods to obtain the $\boldsymbol{g}$-tensor and thereby the g-factor. We start by considering the bulk case of the

usual semiconductors (silicon, germanium and gallium-arsenide) and highlight the effects of the spin-orbit interaction on the g-factor. We also show that the underlying symmetries of our crystals lead to certain quantum information implications. In the subsequent chapters we will show the implementation of our theory.

4.2 The g-tensor formalism

In relativistic quantum mechanics, one may use the Dirac equation,

$$\left(i\hbar\gamma^{\mu}\partial_{\mu} - \frac{e}{c}\gamma^{\mu}A_{\mu} - mc\right)\Psi(x) = 0, \tag{4.1}$$

to describe an electron in an electromagnetic field with a four-potential $A_{\mu} = (\phi, -\boldsymbol{A})$. $\Psi : \mathcal{R}^{1,3} \rightarrow \mathcal{C}^4$ represents a field and γ^{μ} with $\mu = 1, 2, 3, 4$ are the complex matrices,

$$\gamma^0 = \begin{pmatrix} \mathbb{I}_2 & 0 \\ 0 & \mathbb{I}^2 \end{pmatrix}, \gamma^i = \begin{pmatrix} 0 & \sigma^i \\ -\sigma^i & 0 \end{pmatrix}, \tag{4.2}$$

where σ^i are the usual Pauli matrices.
In the non-relativistic limit, we consider the free-electron wavefunctions,

$$\Psi = \begin{pmatrix} e^{-iEt/\hbar}\Psi_+ \\ e^{-iEt/\hbar}\Psi_- \end{pmatrix} \tag{4.3}$$

which gives rise to the coupled equations,

$$\begin{aligned} \left(E - mc - \frac{e}{c}\phi\right)\Psi_+ + \sigma \cdot \left(i\nabla + \frac{e}{c}\right)\Psi_- = 0, \\ \left(E + mc - \frac{e}{c}\phi\right)\Psi_+ + \sigma \cdot \left(i\nabla + \frac{e}{c}\right)\Psi_- = 0. \end{aligned} \tag{4.4}$$

Making the approximation $E - mc - \frac{e}{c}\phi \approx 2m$ and solving for Ψ_-, one gets a time-independent Schrödinger equation,

$$\left[\frac{1}{2m}\left(-i\nabla + \frac{e}{c}\boldsymbol{A}\right)^2 + \frac{e}{c}\phi - \frac{e}{2m}\sigma \cdot \boldsymbol{B}\right]\Psi_+ \approx (E - mc)\,\Psi_+, \tag{4.5}$$

by replacing $\boldsymbol{B} = \nabla \times \boldsymbol{A}$. The term $-\frac{e}{2m}\sigma \cdot \boldsymbol{B}$ can be re-written with the spin-angular momentum operator $\boldsymbol{S} = \frac{\sigma}{2}$ as $-\frac{e}{m}\boldsymbol{S} \cdot \boldsymbol{B} = -\boldsymbol{\mu} \cdot \boldsymbol{B}$ describing the energy of the interaction of the magnetic moment $\boldsymbol{\mu}$ with the external field $\boldsymbol{B}$. Since $\boldsymbol{\mu} = g_s\frac{e}{2m}\boldsymbol{S}, g_s = 2$ is the vacuum value of the g-factor.

The relativistic Dirac equation predicts the value of the g-factor as 2. But corrections to this value, seemingly of a universal nature, arise from the interaction of the electron with virtual particles

(quantum fluctuations),

$$g = 2\left(1 + \frac{\alpha}{2\pi} + \left(\frac{197}{144} + \frac{\pi^2}{12} - \frac{\pi^2}{2}\log(2) + \frac{3}{4}\zeta(3)\right)\left(\frac{\alpha}{\pi}\right)^2 + ...\right), \tag{4.6}$$

where α is the fine structure constant.

We proceed to show that in solid-state physics the corrections to the g-factor are much larger and have origins in the spin-orbit interaction. Consider a crystal electron in an external magnetic field. It is described by the following Schrödinger equation:

$$H(\boldsymbol{B}) = \frac{1}{2m}\left[\boldsymbol{p} - \frac{e\boldsymbol{A}}{c}\right]^2 + V(\boldsymbol{r}) + \frac{\hbar}{4c^2m^2}(\nabla V(\boldsymbol{r}) \times \boldsymbol{p}) \cdot \boldsymbol{\sigma} + \frac{1}{2}g\mu_B\boldsymbol{\sigma} \cdot \boldsymbol{B}. \tag{4.7}$$

The first term is the kinetic term part of the energy. The next term, $V(\boldsymbol{r})$, is the crystal potential and does not directly cause any changes to the g-factor. But as will be shown below, some other factors do cause the g-factor to deviate from its value of 2.
We identify the spin-orbit Hamiltonian,

$$H_{SO} = \frac{\hbar}{4c^2m^2}(\nabla \boldsymbol{V} \times \boldsymbol{p}) \cdot \boldsymbol{\sigma} = \frac{\alpha^2}{4}(\nabla \boldsymbol{V} \times \boldsymbol{p}) \cdot \boldsymbol{\sigma}. \tag{4.8}$$

The last part is written in atomic units where the base units are the electron rest mass, the magnitude of the electron charge, the Planck constant and the permittivity, introducing the fine structure constant α. The spin-orbit interaction causes a splitting of degenerate energy bands. In certain cases, as will also be shown later, when inversion operation is involved, this splitting is forbidden. When spin-orbit interaction is involved, a wavefunction and its time reversed partner will have the same energy (sec.2.4.7),

$$E(\boldsymbol{k}, \uparrow) = E(-\boldsymbol{k}, \downarrow)^1. \tag{4.9}$$

When inversion is involved,

$$E(\boldsymbol{k}, \uparrow) = E(-\boldsymbol{k}, \uparrow);\ E(\boldsymbol{k}, \downarrow) = E(-\boldsymbol{k}, \downarrow). \tag{4.10}$$

Combining Eq.4.9 and Eq.4.10, $E(\boldsymbol{k}, \uparrow) = E(\boldsymbol{k}, \downarrow)$.

Note that the momentum operator in the presence of spin-orbit interaction takes on additional

[1]Here the states $|\uparrow\rangle$ *and* $|\downarrow\rangle$ are not pure spin-up and spin-down states but are used to indicate pseudo-spins.

terms

$$
\begin{aligned}
[\boldsymbol{r}_i, H(0)] &= \left[\boldsymbol{r}_i, \frac{\boldsymbol{p}_i^2}{2m} + V(\boldsymbol{r}) + \frac{\hbar}{4c^2m^2}\left(\boldsymbol{\sigma}\times\nabla V\right)_i \boldsymbol{p}_i\right] \\
&= \left[\boldsymbol{r}_i, \frac{\boldsymbol{p}_i^2}{2m} + V(\boldsymbol{r})\right] + \frac{\hbar}{4c^2m^2}\left(\boldsymbol{\sigma}\times\nabla V\right)_i \left[\boldsymbol{r}_i, \boldsymbol{p}_i\right].
\end{aligned}
$$

$$
[\boldsymbol{r}_i, \boldsymbol{p}_i] \implies [\boldsymbol{r}_i, -i\hbar\partial_{\boldsymbol{r}_i}]\,\psi = -i\hbar\boldsymbol{r}_i\partial_{\boldsymbol{r}_i}\psi + i\hbar\partial_{\boldsymbol{r}_i}\left(\boldsymbol{r}_i\psi\right) = -i\hbar\boldsymbol{r}_i\partial_{\boldsymbol{r}_i}\psi + i\hbar\boldsymbol{r}_i\partial_{\boldsymbol{r}_i}\psi + i\hbar\psi = i\hbar\psi
$$

$$
\left[\boldsymbol{r}_i, \frac{\boldsymbol{p}_i^2}{2m}\right] = [\boldsymbol{r}_i, \boldsymbol{p}_i]\frac{\boldsymbol{p}_i}{2m} - \frac{\boldsymbol{p}_i}{2m}[\boldsymbol{p}_i, \boldsymbol{r}_i] = [\boldsymbol{r}_i, \boldsymbol{p}_i]\frac{\boldsymbol{p}_i}{2m} + \frac{\boldsymbol{p}_i}{2m}[\boldsymbol{r}_i, \boldsymbol{p}_i] = \frac{i\hbar}{m}\boldsymbol{p}_i
$$

$$
\begin{aligned}
\implies [\boldsymbol{r}_i, H(0)] &= \left[\boldsymbol{r}_i, \frac{\boldsymbol{p}^2}{2m} + \frac{\hbar}{4c^2m^2}(\nabla V\times\boldsymbol{\sigma})_i\boldsymbol{p}_i\right] \\
&= \frac{i\hbar}{m}\boldsymbol{p}_i + \frac{i\hbar^2}{4c^2m^2}(\nabla V\times\boldsymbol{\sigma})_i \\
&= \frac{i\hbar}{m}\left(\boldsymbol{p}_i + \frac{\hbar}{4c^2m}(\nabla V\times\boldsymbol{\sigma})_i\right) \\
&= \frac{i\hbar}{m}\boldsymbol{\pi}_i. \qquad (4.11)
\end{aligned}
$$

$$
\boldsymbol{\pi} = \boldsymbol{p} + \frac{\hbar}{4mc^2}\left(\boldsymbol{\sigma}\times\nabla V(\boldsymbol{r})\right).^{2} \qquad (4.12)
$$

The spin-orbit term, which correspond to relativistic effects, causes changes to the g-factor from the value of 2. Since this term is dependant on the crystal potential and the moment, the deviation of the g-factor value from 2 is crystal specific and band specific. This deviation can be quite large, as we shall see. In this chapter we will revisit the analytical form of the g-factor as a tensorial quantity and quantify the deviation from its vacuum value for semiconductors of our interest.

Luttinger [11] first described the charged particles in the topmost valence band. An electron in a periodic potential of a crystal moves as a free electron in vacuum with a wave-vector $\boldsymbol{k}$ and an effective mass m^*. The effects of the forces acting on it are captured by this effective mass. The effective mass is a tensorial quantity as it described by the curvature of the energy bands. In certain semiconductors such as silicon, this curvature is not symmetric and has a significant dependence on the x-, y- and z-directions. The wave-vector or the quasi-momentum of the electron takes a gauge-invariant form as can be seen in Eq.4.7, $\boldsymbol{p} = \hbar\boldsymbol{k} \rightarrow \pi = \hbar\boldsymbol{k} = \boldsymbol{p} - \frac{e\boldsymbol{A}}{c}$. The wavevector no

[2] In general, $\langle\boldsymbol{\pi}\rangle \approx \langle\boldsymbol{p}\rangle$ is a good approximation as the matrix element of $\frac{\hbar}{4mc^2}\boldsymbol{\sigma}\times\nabla V(\boldsymbol{r})$, for many materials of interest, is quite small. We, therefore, use these two inter-changeably.

longer commutes,

$$\begin{aligned}
[k_i, k_j]\psi &= -i[k_i, \partial_{r_j}]\psi - \frac{eB}{\hbar c}[k_i, r_i]\psi \\
&= -i\underbrace{(k_i\partial_{r_j}(\psi) - \partial_{r_j}(k_i)\psi - k_i\partial_{r_j}(\psi))}_{0} - \frac{eB}{\hbar c}(-i\partial_{r_i}(r_i)\psi \underbrace{-ir_i\partial_{r_i}(\psi) + ir_i\partial_{r_i}(\psi)}_{0}) \\
&= i\frac{eB}{\hbar c}\psi. \\
\implies [k_i, k_j] &= \frac{ie}{\hbar c}(\hat{\boldsymbol{i}} \times \hat{\boldsymbol{j}}) \cdot \boldsymbol{B}.
\end{aligned} \tag{4.13}$$

Consequently, the effective mass has a non-vanishing asymmetric part,

$$\left(\frac{1}{m^*}\right)^{AS} = \frac{1}{2}\left[\frac{1}{m^*_{ij}} - \frac{1}{m^*_{ji}}\right], \tag{4.14}$$

and is proportional to B. For any band n, the asymmetric term has the operator form [12, 13]

$$\left(\frac{1}{m^*}\right)^{AS}_{ij} = \frac{1}{m^2}\sum_{n' \neq n}\frac{\pi_i \left|u_{n'\boldsymbol{k}}\right\rangle\!\left\langle u_{n'\boldsymbol{k}}\right| \pi_j}{E_n - E_{n'}} - \frac{1}{m^2}\sum_{n' \neq n}\frac{\pi_j \left|u_{n'\boldsymbol{k}}\right\rangle\!\left\langle u_{n'\boldsymbol{k}}\right| \pi_i}{E_n - E_{n'}}, \tag{4.15}$$

where $|u_{n\boldsymbol{k}}\rangle$ is the Bloch wavefunction of the band electron. This operator acts within the space of two (spin-degenerate) Bloch wave-functions $|u_{n\boldsymbol{k}}\rangle$ of band n. The Zeeman splitting of band state at energy E_{nk} in magnetic field $\mathbf{B}$ is given by the eigenvalues of the 2×2 spin Hamiltonian

$$H_{nk} = E_{nk} + \frac{\hbar^2}{2}\epsilon_{ijl}\left(\frac{1}{m^*}\right)^{AS}_{ij}\left(\frac{ieB_l}{\hbar c}\right) + \mu_B \boldsymbol{\sigma} \cdot \mathbf{B} \tag{4.16}$$

(using the Einstein summation convention). The splitting of the spin-degenerate eigenvalues around the zero-field value E_{nk} has the form

$$\Delta E_{nk} = \mu_B \sqrt{B_i G_{ij} B_j}. \tag{4.17}$$

This defines the symmetric tensor G_{ij}, from which the band g-tensor is obtained [3]:

$$\boldsymbol{G} = \boldsymbol{g} \cdot \boldsymbol{g}^T. \tag{4.18}$$

Note that the definition of $\boldsymbol{g}$ is not unique, leaving open the question of whether it should be considered symmetric or not. Later on, we define $\boldsymbol{g}$ in terms of the magnetization of the band state, but the non-uniqueness in that case arises from the choice of basis of the pair of band states $|u_{nk}\rangle$. Some previous work has used the non-symmetric form of the g-tensor [15, 16]. We will

[3] Note that we use the convention of Abragam and Bleaney [14] in Eq.4.18; other, more recent work (e.g., [15]) uses a transposed convention, i.e., $G = g^T g$.

adopt a convention for which $\boldsymbol{g}$ is not necessarily symmetric; but our discussion will depend on certain invariants such as the singular values of $\boldsymbol{g}$ or the determinant of $\boldsymbol{g}$, which are uniquely determined by definition Eq.4.18.

In Eq.4.16 one may notice that $\boldsymbol{g}$ has two distinct contributions, $\boldsymbol{g} = \boldsymbol{g}_L + \boldsymbol{g}_S$. If spin orbit is zero, only the last, pure spin term will contribute, in this case with the value 2. For finite spin orbit its contribution, which we denote $\boldsymbol{g}_S$, will be modified. There will also be a nonzero orbital magnetization contribution $\boldsymbol{g}_L$ from the middle term of Eq.4.16. Further, $\boldsymbol{g}_L$ is directly determined by the antisymmetric part of the inverse effective mass tensor. We proceed to define the two contributions, $\boldsymbol{g}_S$ and $\boldsymbol{g}_L$, separately.

4.2.1 The spin g-tensor, g_s

As mentioned earlier, the Bloch-state $|u_{n\boldsymbol{k}}\rangle$ of band n has two orthogonal partners which we denote as $|\xi\rangle$ and $|\bar{\xi}\rangle$. These states are spin-degenerate at wavevector $\boldsymbol{k}$ in the limit of no spin-orbit interaction. They may have different energies when the spin-orbit interaction is non-zero. In some cases, as will be seen later on, these states are related by time-reversal followed by a unitary operation, u that takes $\boldsymbol{k}$ to $-\boldsymbol{k}$ (for example, u can be inversion),

$$|\bar{\xi}\rangle = i\sigma_y \kappa u \, |\xi\rangle \,, \tag{4.19}$$

where κ is a complex conjugation followed by a σ_y Pauli rotation. We refer to these states "pseudo-Kramers".

We can then write the spin-matrix,

$$S_i = \frac{1}{2} \begin{pmatrix} \langle \xi | \sigma_i | \xi \rangle & \langle \xi | \sigma_i | \bar{\xi} \rangle \\ \langle \bar{\xi} | \sigma_i | \xi \rangle & \langle \bar{\xi} | \sigma_i | \bar{\xi} \rangle \end{pmatrix}, \tag{4.20}$$

and a simple expression for the spin contribution to the g-tensor,

$$g_{Sij} = \frac{1}{2} \operatorname{Tr}\left(2 S_i \tilde{\sigma}_j\right). \tag{4.21}$$

Note that we are working with atomic units. From the usual magnetic moment formula, $\boldsymbol{M} = \boldsymbol{L} + 2\boldsymbol{S}$, the appearance of $2\boldsymbol{S}_i$ is correct. $\tilde{\sigma}_j$ is a Pauli-operator acting on the subspace of $|\xi\rangle$, $|\bar{\xi}\rangle$ and is not the same as σ above that acts on the electron-spin Hilbert space $|\uparrow\rangle$, $|\downarrow\rangle$.

4.2.2 The orbital moment contribution to the g-tensor, g_L

A different point of view about the magnetic moment of band electrons has emerged much later. Consider the electron state as the coherent transport of a localized wave-packet moving in $\boldsymbol{k}$-space

[17–19]. The wave-packet is considered to be spread over a small portion of the Brillouin zone and is affected only by the local band properties. The rotation around its center of mass causes this wavepacket to have an orbital magnetic moment given by[4]

$$L(\boldsymbol{k}) = i\frac{e}{2\hbar}\left\langle \nabla_{\boldsymbol{k}} u_n \right| \times \left[H(\boldsymbol{k}) - \epsilon_n(\boldsymbol{k})\right] \left|\nabla_{\boldsymbol{k}} u_m\right\rangle, \tag{4.22}$$

where we see the appearance of the Berry curvature $|\nabla_{\boldsymbol{k}} u_m\rangle$. Though at first it may seem dif-

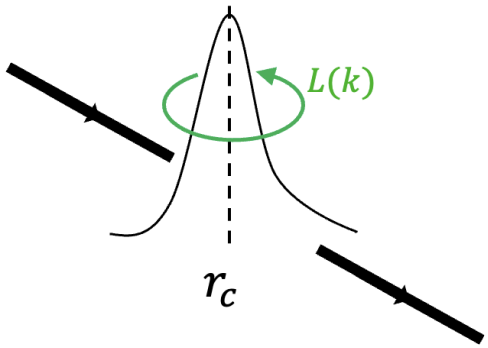

Figure 4.1: Orbital angular momentum, $L(\boldsymbol{k})$, of a wave-packet around its center of mass along $\boldsymbol{r}_c$.

ferent, this alternative formulation is completely equivalent to the Luttinger result Eq.4.15. The gradient of the Bloch wave-function can equivalently be written using the position-Hamiltonian commutator [20],

$$\left|\partial_j u_m\right\rangle = -\frac{i}{\hbar}\sum_{l\neq m} \left|u_l\right\rangle \frac{\left\langle u_l\right|\left[x_j, H\right]\left|u_m\right\rangle}{E_l - E_m}. \tag{4.23}$$

The orbital magnetic moment operator takes the form

$$\hat{L}_i(\boldsymbol{k}) = \frac{ie}{2\hbar^3}\sum_{\substack{j,k,\\ p\neq n,m}} \epsilon_{ijk}\frac{\left[x_j, H\right]\left|u_p\right\rangle\left\langle u_p\right|\left[x_k, H\right]}{\bar{E}_{nm} - E_p}. \tag{4.24}$$

L_i is an operator acting on the states $|u_n\rangle$ and $|u_m\rangle$. Recall that these are assumed to be degenerate if the spin-orbit interaction is zero, but in general may not be exactly degenerate with finite spin orbit interaction[19]. Here $\bar{E}_{nm} = \frac{E_n+E_m}{2}$.

If bands n and m are degenerate, so that $\frac{E_n+E_m}{2} = E_n = E_m$, then indeed the asymmetric mass

[4]The sign of Eq.4.22 is the opposite of the sign found in the general literature. The sign of Eq.4.25 corresponds to the atomic limit of the Landé g.

term is the magnetization operator; since $\frac{i\hbar}{m}\pi_j = [x_j, H]$ $\left(\sim \frac{i\hbar}{m}\boldsymbol{p}\right)$,

$$\hat{L}_i = \frac{-ie}{2\hbar m^2} \sum_{\substack{j,k,\\ p\neq n,m}} \epsilon_{ijk} \frac{\pi_j |u_p\rangle\langle u_p| \pi_k}{\bar{E}_{nm} - E_p} = \frac{-ie}{\hbar}\epsilon_{ijk}\left(\frac{1}{m^*}\right)^{AS}_{jk}. \tag{4.25}$$

A similar expression as to Eq.4.20 can be written for the orbital angular momentum matrix for states $|\xi\rangle$ and $|\bar{\xi}\rangle$,

$$L_i = \sum_{jkl} \frac{\epsilon_{ijk}}{\bar{E}_{\xi\bar{\xi}} - E_l} \begin{pmatrix} \langle\xi|\pi_j|u_l\rangle\langle u_l|\pi_k|\xi\rangle & \langle\xi|\pi_j|u_l\rangle\langle u_l|\pi_k|\bar{\xi}\rangle \\ \langle\bar{\xi}|\pi_j|u_l\rangle\langle u_l|\pi_k|\xi\rangle & \langle\bar{\xi}|\pi_j|u_l\rangle\langle u_l|\pi_k|\bar{\xi}\rangle \end{pmatrix}. \tag{4.26}$$

Note this is in atomic units, $e = \hbar = m = 1$. Then, similarly to Eq.4.21,

$$g_{Lij} = \frac{1}{2}\,\mathrm{Tr}\big(L_i\tilde{\sigma}_j\big). \tag{4.27}$$

4.3 Topological and entanglement properties of the g-tensor

For materials where the spin-orbit coupling is weak, such as silicon, one might expect $\boldsymbol{g}_S$ to be 2 and $\boldsymbol{g}_L$ to have negligible contribution. We find that this is true for certain bands in certain parts of the Brillouin zones. In other parts of the Brillouin zones, this is far from true. In the following sections we show that symmetry guarantees that the eigenvalues of $\boldsymbol{g}$ or the singular values of $\boldsymbol{G}$ must differ from 2 and cross regions of maximal spin-orbit entanglement. We first present the necessary tools to understand this and then discuss the connection to entanglement.

4.3.1 Linear algebra of the g-tensor

From the definition of $\boldsymbol{g}$ (Eq.4.17. and Eq.4.18), the eigenvalues of $\boldsymbol{G}$ are the square of the singular values of $\boldsymbol{g}$. The singular value decomposition of $\boldsymbol{g}$ is,

$$\boldsymbol{g} = U\,\Sigma\,V. \tag{4.28}$$

Since $\boldsymbol{g}(\boldsymbol{k})$ is a real matrix, U and V are also two $\boldsymbol{k}$-dependent real orthogonal symmetric matrices, unique except sign changes columnwise for U and rowwise for V. Σ, a positive semidefinite diagonal matrix of the singular values of $\boldsymbol{g}$, also $\boldsymbol{k}$-dependent, has three scalar elements on its diagonal $\Sigma_{xx} \geq \Sigma_{yy} \geq \Sigma_{zz}$ arranged in descending order. These three scalars are commonly know as g-factors.

The columns of U give the principle axes of the external $\boldsymbol{B}$ field, so the Zeeman splitting can

be re-written using the singular values as,

$$\Delta E = \mu_{\boldsymbol{B}} \sqrt{\Sigma_{xx}^2 B_x^2 + \Sigma_{yy}^2 B_y^2 + \Sigma_{zz}^2 B_z^2}. \tag{4.29}$$

The magnetic moment vector of the ground state is,

$$M_i^{ground} = \frac{\mu_B^2 \Sigma_{ii}^2 B_i}{2\Delta E}. \tag{4.30}$$

4.3.2 The relation to entanglement

The expression for the g-tensor, (formed using Eq.4.21 and Eq.4.27) involves the eigenvectors of the Hamiltonian, $H(\boldsymbol{k})$. Since $H(\boldsymbol{k})$ can be chosen to vary continuously with the wavevector $\boldsymbol{k}$, the eigenvectors can also be chosen to be continuous in $\boldsymbol{k}$. Thus the g-tensor must be a continuous quantity with respect to $\boldsymbol{k}$ and consequently, its determinant $det(\boldsymbol{g}_S)$ must also be continuous.

We provide a proof of why the g-tensor must differ from 2 in Theorem.1 using the linear algebra of this quantity that has been discussed above. But before that we must define the band pair, $\mathcal{B}(\boldsymbol{k})$ and $\bar{\mathcal{B}}(\boldsymbol{k})$ for which any accidental degeneracy is absent and to which this theorem applies.

Recall the expression for the spin-orbit Hamlitonian in Eq.4.8 in Hartree atomic units,

$$H_{SO}(\boldsymbol{k}) = \frac{\alpha^2}{4} (\nabla \boldsymbol{V} \times \boldsymbol{p}) \cdot \boldsymbol{\sigma}. \tag{4.31}$$

Here α is the fine structure constant but for the sake of definition 1 and theorem. 1, we treat it as a running constant.

Consider the table 4.1 as shown below. For no spin-orbit interaction, the bands that we will focus on are labeled according to the irreducible representations in blue as shown in table 4.1. When the spin-orbit interaction is turned on ($\alpha > 0$), the bands with the blue labels split into bands with the double group irreducible representations in red and black. The bands in red have two-fold degeneracy whereas the bands in black may have a different degeneracy.

T	$\Gamma_4 \otimes D_{1/2} = \Gamma_5 \oplus \Gamma_6 \oplus \Gamma_7$	–
T_h	$\Gamma_4^+ \otimes D_{1/2} = \Gamma_5^+ \oplus \Gamma_6^+ \oplus \Gamma_7^+$ $\Gamma_4^- \otimes D_{1/2} = \Gamma_5^- \oplus \Gamma_6^- \oplus \Gamma_7^-$	$\forall \overrightarrow{OA}$
T_d	$\Gamma_4 \otimes D_{1/2} = \Gamma_6 \oplus \Gamma_8$ $\Gamma_5 \otimes D_{1/2} = \Gamma_7 \oplus \Gamma_8$	$\overrightarrow{OA} \vert \boldsymbol{A} \in \{(0,0,k_z),$ $(k_x,0,0),(0,k_y,0),$ $(k_x,k_y,k_z)\}$
O	$\Gamma_4 \otimes D_{1/2} = \Gamma_6 \oplus \Gamma_8$ $\Gamma_5 \otimes D_{1/2} = \Gamma_7 \oplus \Gamma_8$	–
O_h	$\Gamma_4^+ \otimes D_{1/2} = \Gamma_6^+ \oplus \Gamma_8^+$ $\Gamma_5^+ \otimes D_{1/2} = \Gamma_7^+ \oplus \Gamma_8^+$ $\Gamma_4^- \otimes D_{1/2} = \Gamma_6^- \oplus \Gamma_8^-$ $\Gamma_5^- \otimes D_{1/2} = \Gamma_7^- \oplus \Gamma_8^-$	$\forall \overrightarrow{OA}$

Table 4.1: Band labels for which $det(\boldsymbol{g}_S)$ is guaranteed to pass through 0 along the ray $\overrightarrow{OA}$. Groups of bands are labeled according the irreducible representations of the states in the set of bands at $\mathbf{k} = 0$ as given in [21],[22]. The left-most column of this table indicates the points groups. In the central columns, the bands denoted in blue are bands without spin-orbit interactions. These bands split into the red and black bands when spin-orbit couplings are taken into account. The red bands are the bands with Kramers degeneracy at $\mathbf{\Gamma}$ for which $det(\boldsymbol{g}_S)$ changes its sign along any ray $\overrightarrow{OA}$. The right-most column of the table contains the directions in which a maximal spin-orbit entanglement is guaranteed for the degenerate red bands of the corresponding symmetry group.

It is required that there be no accidental degeneracies involving the band pair $\mathcal{B}(\boldsymbol{k}), \bar{\mathcal{B}}(\boldsymbol{k})$ dispersing from the states belonging to irrep. Γ_i (red irreps. from Table.4.1). This pair is degenerate at $\boldsymbol{k} = 0$, and sometimes degenerate elsewhere (for some point groups and some directions in $\boldsymbol{k}$-space). Furthermore, this pair of bands is degenerate as $\alpha \to 0$ with the other bands $\mathcal{B}_{mult}(\boldsymbol{k})$ associated with the accompanying irrep Γ_j in the table, i.e., in the pair $\Gamma_i \oplus \Gamma_j$. Besides these, it is required that no other degeneracies occur, as captured by this definition ($\alpha_* > 0$ is some fixed

spin-orbit strength):

Definition 1. *Non-degeneracy of Bands.*
Band pair $\mathcal{B}(\boldsymbol{k}), \bar{\mathcal{B}}(\boldsymbol{k})$ is non-degenerate if $\forall\alpha$ such that $0 < \alpha < \alpha_*$, $\exists k_{ND}$ and $\Delta E > 0$ and all three conditions are true: 1) $\forall \boldsymbol{k}, |\boldsymbol{k}| \leq k_{ND}, \forall \mathcal{B}'(\boldsymbol{k}) \notin \{\mathcal{B}(\boldsymbol{k}), \bar{\mathcal{B}}(\boldsymbol{k}), \mathcal{B}_{mult}(\boldsymbol{k})\}, \forall \mathcal{B}''(\boldsymbol{k}) \in \{\mathcal{B}(\boldsymbol{k}), \bar{\mathcal{B}}(\boldsymbol{k}), \mathcal{B}_{mult}(\boldsymbol{k})\}$, $|\mathcal{B}'(\boldsymbol{k}) - \mathcal{B}''(\boldsymbol{k})| > \Delta E$. 2) $\forall \boldsymbol{k}, |\boldsymbol{k}| \leq k_{ND}$, $\mathcal{B}(\boldsymbol{k})$ and $\bar{\mathcal{B}}(\boldsymbol{k})$ are nowhere degenerate with $\mathcal{B}_{mult}(\boldsymbol{k})$. 3) $\forall \boldsymbol{k}, |\boldsymbol{k}|{=}k_{ND}$, $|\mathcal{B}(\boldsymbol{k}) - \mathcal{B}_{mult}(\boldsymbol{k})| > \Delta E$ and $|\bar{\mathcal{B}}(\boldsymbol{k}) - \mathcal{B}_{mult}(\boldsymbol{k})| > \Delta E$.

The conditions of our definition can be easily checked for any band-pair in a particular crystal, and are seen to be true for the materials studied later in the paper. We can now proceed directly with the first main result:

Theorem 1. *Given a crystal with any of the cubic point group symmetries: O, O_h, T, T_h or T_d. Consider any pair of energy bands belonging to the irreducible representations of the symmetry group of the crystal, indicated in red from Table.4.1, which have come from states with the blue irreducible representation for zero spin-orbit coupling. We consider band pairs that are nondegenerate in the sense of Definition 1. Then for sufficiently small spin-orbit coupling, there exists a surface in k-space, enclosing the Γ point, on which $det(\boldsymbol{g}_S(\boldsymbol{k})) = 0$, where $\boldsymbol{g}_S(\boldsymbol{k})$ is the spin contribution to the g-tensor.*

Proof. Consider the bands that occur in the band structure of crystals with the point groups O, O_h, T, T_h, T_d, that belong to the irreducible representations in red in Table.4.1 at $\boldsymbol{k} = 0$. The condition that the spin-orbit interaction is nonzero implies that these states are only doubly degenerate, and not higher (accidental degeneracies are excluded by assumption). This two-fold degeneracy is precisely the Kramers degeneracy. We denote these Kramers-degenerate pairs as $|\xi_\Gamma\rangle, |\bar{\xi}_\Gamma\rangle$ where Γ is any of the red labels of Table.4.1.

Using Eqs.4.20,4.21, we calculate the spin g-tensor of these doubly degenerate bands. At $\mathbf{k} = 0$ and infinitesimal spin-orbit coupling $\alpha = 0^+$ the eigenvectors of these bands belonging to red irrep Γ_i are built up from the so-called [13] "p-like states" $|X\rangle, |Y\rangle, |Z\rangle$, mutually orthogonal, normalized orbital states. The term "p-like" refers to the orbital states often being predominantly composed of atomic p-orbital states. Due to symmetry (cf. [13], and spin harmonics tabulated in [21]), the eigenstates of all the red irreducible representations Γ have the form

$$
\begin{aligned}
|\xi_\Gamma\rangle &= \left|\frac{1}{2}, \frac{1}{2}\right\rangle = \frac{1}{\sqrt{3}} \left(|Z\rangle |\uparrow\rangle + |X\rangle |\downarrow\rangle + i |Y\rangle |\downarrow\rangle\right), \\
|\bar{\xi}_\Gamma\rangle &= \left|\frac{1}{2}, -\frac{1}{2}\right\rangle = \frac{1}{\sqrt{3}} \left(|Z\rangle |\downarrow\rangle - |X\rangle |\uparrow\rangle + i |Y\rangle |\uparrow\rangle\right).
\end{aligned} \tag{4.32}
$$

For a finite non-zero α all states of irrep Γ_i are mixed. Some may not have the form of (4.32) because they arise from different non-relativistic states, e.g.. for group T_d, one has $\Gamma_1 \otimes D_{1/2} = \Gamma_6$. For $\alpha = 0^+$ these additional states always have the simple form $|S\rangle |\uparrow\rangle$, $|S\rangle |\downarrow\rangle$. These states could

be mixed and so the eigenstates will have the more general form

$$|\xi_\Gamma\rangle = \left|\frac{1}{2},\frac{1}{2}\right\rangle + |\delta\xi_\Gamma\rangle\,,$$
$$|\bar{\xi}_\Gamma\rangle = \left|\frac{1}{2},-\frac{1}{2}\right\rangle + |\delta\bar{\xi}_\Gamma\rangle\,. \tag{4.33}$$

But because of the non-degeneracy condition, these corrections $|\delta\xi\rangle$ can be calculated using perturbation theory[5]. The denominators $E^{(0)}_{n'} - E^{(0)}_{n}$ are guaranteed to have a magnitude no less than a finite constant ΔE by definition 1. We conclude from this that $\text{norm}(|\delta\xi\rangle) = O(\alpha/\Delta E)$. With this, an explicit calculation of the spin-contribution (Eqs.4.20,4.21) for any pair of states of the form (4.33) gives

$$\boldsymbol{g}_S = \begin{pmatrix} \frac{2}{3} & 0 & 0 \\ 0 & \frac{2}{3} & 0 \\ 0 & 0 & -\frac{2}{3} \end{pmatrix} + O(\alpha/\Delta E), \tag{4.34}$$

Thus $det(\boldsymbol{g}_S(\boldsymbol{k}=\boldsymbol{0})) = -\frac{8}{27} + O(\alpha/\Delta E)$, so that $det(\boldsymbol{g}_S(\boldsymbol{k}=\boldsymbol{0})) < 0$ for sufficiently small α.

Note that $g_S = -2/3$ coincides with the application of the Landé expression with quantum numbers $L = 1, S = \frac{1}{2}, J = \frac{1}{2}$ [23]. The Landé expression for $\boldsymbol{g}_S$ can be seen from eq.31.37 of [23], p. 654. This equation shows the two contributions to the g-tensor in the atomic limit. It is interesting to note that while it is common to say that these band states have quantum numbers $\boldsymbol{L} = 1, \boldsymbol{S} = \frac{1}{2}, \boldsymbol{J} = \frac{1}{2}$, the symmetries that this statement implies are only partially in force. In particular, while symmetry dictates that g_S is indeed exactly the Landé value $-\frac{2}{3}$ for $\alpha \to 0$. g_L is not fixed to its Landé value $+\frac{4}{3}$.

Let us now consider the calculation of $\boldsymbol{g}_S(\boldsymbol{k})$ for $|\boldsymbol{k}| = k_{ND}$ (see Definition 1). We need the Bloch eigenvectors of bands $\mathcal{B}(\boldsymbol{k}), \bar{\mathcal{B}}(\boldsymbol{k})$ to evaluate Eq.4.20, we denote this pair as $|u_n(\boldsymbol{k})\rangle$ and $|u_m(\boldsymbol{k})\rangle$. Again using perturbation theory:

$$|u_{n/m}(\boldsymbol{k})\rangle = \left|u^{(0)}_{n/m}(\boldsymbol{k})\right\rangle - \frac{\alpha^2}{4}\sum_{n'\neq n,m} \frac{\left\langle u^{(0)}_{n'}(\boldsymbol{k})\right| (\nabla \boldsymbol{V}\times\boldsymbol{p})\cdot\boldsymbol{\sigma}\left|u^{(0)}_{n/m}(k)\right\rangle}{E^{(0)}_{n'} - E^{(0)}_{n/m}} \left|u^{(0)}_{n'}(\boldsymbol{k})\right\rangle + \mathcal{O}\left(\frac{\alpha^4}{16\Delta E^2}\right). \tag{4.35}$$

Again, we use the fact that all energy denominators are by assumption greater than ΔE. Thus, the states $|u_{n/m}(\boldsymbol{k})\rangle$, for sufficiently small α, are arbitrarily close to the eigenvectors with no spin orbit coupling $\left|u^{(0)}_{n/m}(\boldsymbol{k})\right\rangle$. For these the three eigenvalues of $\boldsymbol{g}_S$ are $+2$, and thus $det(\boldsymbol{g}_S(k_{ND})) = +8$. Since $det\,(\boldsymbol{g}_S)$ is continuous in $\boldsymbol{k}$ and changes sign between the origin and the sphere of radius k_{ND}, there must be a closed surface within this sphere on which $det(\boldsymbol{g}_S(k_{ND})) = 0$. □

[5]We assume the convergence of this perturbation, which is essentially the same as the issue of the convergence of the $\boldsymbol{k}\cdot\boldsymbol{p}$ perturbation calculations as in eqs. (4.15) and (4.23), which is well established.

Note that the g-factors describe an isotropic quantity at $\mathbf{k} = (0,0,0)$. Equation 4.34 does not contradict this, as changing the phase convention of one state, $\left|\bar{\xi}_\Gamma\right\rangle \to -\left|\bar{\xi}_\Gamma\right\rangle$, gives, for $\alpha = 0^+$,

$$\boldsymbol{g}_S = \begin{pmatrix} -\frac{2}{3} & 0 & 0 \\ 0 & -\frac{2}{3} & 0 \\ 0 & 0 & -\frac{2}{3} \end{pmatrix}, \tag{4.36}$$

whose determinant is also $-\frac{8}{27}$, and whose magnetic moment $\boldsymbol{M}$ is also identical, as seen from Eq.4.30. A similar change of sign convention causes the eigenvalues of $\boldsymbol{g}_S$ at k_{ND} to be $(-2,-2,2)$, but with $det(\boldsymbol{g}_S) = +8$ unchanged.

The Theorem.1 may seem to contradict the seemingly obvious assertion that $g_S = 2$ if there is no spin-orbit coupling, which would mean that $det(\boldsymbol{g_S}) = +8$. But the actual statement is more subtle: as $\alpha \to 0$, $det(\boldsymbol{g}_S(\boldsymbol{k})) = +8$ for almost all $\boldsymbol{k}$. When $\alpha = 0$, $\boldsymbol{k} = 0$ is special because of the emergent 6-fold degeneracy of the multiplets. Thus, the order of limits $\alpha \to 0$, $\boldsymbol{k} \to 0$ is important, and it is permitted that a surface $det(\boldsymbol{g}_S(\boldsymbol{k})) = 0$ always exists, but this surface must collapse onto the origin as $\alpha \to 0$.

Having shown that the $det(\boldsymbol{g}_S)$ must go to zero, we noticed that along the directions $\overrightarrow{OA}$ shown in the third column of Table.4.1, states in these bands exhibit maximum entanglement at the point where $det(\boldsymbol{g}_S) = 0$. We will now proceed to prove this interesting fact and show the relation of $det(\boldsymbol{g}_S) = 0$ to the spin-orbit entanglement. For this, we need to show the general relation between the reduced density matrices of the electron spin, ρ_S and $\bar{\rho}_S$ of the states $|\xi\rangle$ and $\left|\bar{\xi}\right\rangle$ respectively.

Lemma 1. *Consider the reduced density matrices, ρ_S and $\bar{\rho}_S$ of the Kramers-paired bands corresponding to the irreducible representations in red in Table.4.1 along the directions $\overrightarrow{OA}$. Then,*

$$\bar{\rho}_S = \sigma_y \rho_S^T \sigma_y \tag{4.37}$$

.

Proof. Consider the eigenstates $|\xi\rangle$ and $\left|\bar{\xi}\right\rangle$ of Kramers-paired bands corresponding to the irreducible representations of inversion-symmetric groups O_h, T_h and the group T_d. The proof is distributed in three parts as the underlying symmetry for each of these cases is different. The first part deals with the inversion-symmetric groups. For the group T_d, degenerate eigenstates occur only along the $\boldsymbol{\Delta}$- and the $\boldsymbol{\Lambda}$- directions. The second and the third parts deal with these two cases of T_d.

1. The eigenstates $|\xi\rangle$ and $\left|\bar{\xi}\right\rangle$ of bands in the inversion-symmetric groups are related by an inversion followed by the time-reversal operation θ [22, 24], having the form,

$$|\xi\rangle = \sum_r u(r)e^{i\boldsymbol{k}\cdot\boldsymbol{r}}, \quad \left|\bar{\xi}\right\rangle = \sum_r \theta(u(-r))e^{i\boldsymbol{k}\cdot\boldsymbol{r}} \tag{4.38}$$

, The reduced density matrices of these two states are, $\rho_S = \mathrm{Tr}_{orb}\,\rho = \mathrm{Tr}_{orb}\,(|\xi\rangle\langle\xi|)$ and $\bar{\rho}_S = \mathrm{Tr}_{orb}\,\bar{\rho} = \mathrm{Tr}_{orb}\left(\left|\bar{\xi}\right\rangle\left\langle\bar{\xi}\right|\right)$. Note that inversion is a space operation and therefore does not affect the spin part. Since ρ_S is hermitian, $\bar{\rho}_S = \sigma_y\kappa\rho_S\kappa\sigma_y = \sigma_y\rho_S^T\sigma_y$ (κ indicating complex conjugation)[25].

2. In the $\boldsymbol{\Lambda}$-direction of T_d, the states $|\xi\rangle$ and $\left|\bar{\xi}\right\rangle$ belong to the irreducible representation Λ_4 [26] and are given by linear combinations of the basis states of the little group C_{3v}. The basis states of C_{3v}, for the first partner of the irreducible representation Λ_4, can be chosen to be the following combinations involving the s-like and p-like (cf. Eq. 4.32) mutually orthogonal states (a way to obtain this is shown in section.2.4.3),

$$\begin{aligned}
\left|B_1^{\Lambda_4}\right\rangle &= |S\rangle\,|\uparrow\rangle\,, \\
\left|B_2^{\Lambda_4}\right\rangle &= \frac{1}{\sqrt{3}}\left(|X\rangle\,|\uparrow\rangle + |Y\rangle\,|\uparrow\rangle + |Z\rangle\,|\uparrow\rangle\right), \\
\left|B_3^{\Lambda_4}\right\rangle &= \frac{1}{\sqrt{6}}\left(|X\rangle\left(|\uparrow\rangle + i\,|\downarrow\rangle\right) - |Y\rangle\left(|\uparrow\rangle - |\downarrow\rangle\right)\right), \\
&\quad - \frac{(1+i)}{\sqrt{6}}\,|Z\rangle\,|\downarrow\rangle\,.
\end{aligned} \tag{4.39}$$

Using the projection operator formalism detailed in section.2.4.3 and also as defined in section 4.4 of [27], $\hat{P}_{kl}^{\Gamma_n}$, by definition, transforms one basis vector $|l\rangle$ into the basis vector $|k\rangle$ of the same representation Γ_n. That is, the eigenstate $|\xi\rangle = \alpha_1\left|B_1^{\Lambda_4}\right\rangle + \alpha_2\left|B_2^{\Lambda_4}\right\rangle + \alpha_3\left|B_3^{\Lambda_4}\right\rangle$ of the representation Λ_4 is transformed using the projector into $\left|\bar{\xi}\right\rangle = \hat{P}_{\bar{\xi}\xi}^{\Lambda_4}\,|\xi\rangle$. We see that this transformation involves a reversal of spin directions in these basis states. Indeed, direct calculation, starting from

$$\bar{\rho} = P_{\bar{\xi}\xi}^{\Lambda_4}\rho P_{\bar{\xi}\xi}^{\Lambda_4\dagger}, \tag{4.40}$$

where $\bar{\rho}$ is the density matrix corresponding to the state $\bar{\xi}$, shows that this leads to the reduced density matrices $\rho_S = \mathrm{Tr}_{orb}(\rho)$ and $\bar{\rho}_S = \mathrm{Tr}_{orb}(\bar{\rho})$ being related as

$$\bar{\rho}_S = \begin{pmatrix} \rho_{S22} & -\rho_{S12} \\ -\rho_{S21} & \rho_{S11} \end{pmatrix} \tag{4.41}$$

which is the component-wise form of Eq.4.37. It is interesting to note that this derivation makes no use of the time reversal symmetry.

3. The relevant representation Δ_5 of the little group C_{2v} of T_d has four basis states formed out

of the s- and p-like mutually orthogonal states (the details of obtaining the basis states is shown in chapter 2, section.2.4.3):

$$\begin{aligned}\left|B_1^{\Delta_5}\right\rangle &= |S\rangle\,|\uparrow\rangle\,,\\ \left|B_2^{\Delta_5}\right\rangle &= |X\rangle\,|\downarrow\rangle\,,\\ \left|B_3^{\Delta_5}\right\rangle &= |Y\rangle\,|\downarrow\rangle\,,\\ \left|B_4^{\Delta_5}\right\rangle &= |Z\rangle\,|\uparrow\rangle\,.'\end{aligned} \tag{4.42}$$

Note the alternation of spin directions! The projector $\hat{P}^{\Delta_5}_{\bar{\xi}\xi}$, following the definition of [27], transforms the state $|\tilde{\xi}\rangle = \alpha_1\left|B_1^{\Delta_5}\right\rangle + \alpha_2\left|B_2^{\Delta_5}\right\rangle + \alpha_3\left|B_3^{\Delta_5}\right\rangle + \alpha_4\left|B_4^{\Delta_5}\right\rangle$ into $|\bar{\tilde{\xi}}\rangle = \hat{P}^{\Delta_5}_{\bar{\xi}\xi}\,|\tilde{\xi}\rangle$. Given the form of the eigenvector $|\tilde{\xi}\rangle$, its spin density matrix is diagonal,

$$\rho_S = \begin{pmatrix}\rho_{S11} & 0\\ 0 & \rho_{S22}\end{pmatrix}. \tag{4.43}$$

Using the projector, we arrive at the state,

$$\bar{\rho}_S = \mathrm{Tr}_{orb}\left(\hat{P}^{\Delta_5}_{\bar{\xi}\xi}\rho\hat{P}^{\Delta_5\dagger}_{\bar{\xi}\xi}\right) = \begin{pmatrix}\rho_{S22} & 0\\ 0 & \rho_{S11}\end{pmatrix}, \tag{4.44}$$

consistent with Eq.4.37. □

Note that Eq.4.44 implies the satisfaction of the condition Eq.4.37 for any choice of the partners of the representation: for an arbitrary SU(2) rotation

$$V = \begin{pmatrix}X & Y\\ -Y^* & X^*\end{pmatrix}, \tag{4.45}$$

$$\begin{aligned}V\bar{\rho}_S V^\dagger &= \begin{pmatrix}c|X|^2-(1-c)|Y|^2 & (1-2c)XY\\ (1-2c)X^*Y^* & -(c-1)|X|^2+c|Y|^2\end{pmatrix}\\ &= \sigma_y(V\rho_S V^\dagger)^T\sigma_y,\end{aligned} \tag{4.46}$$

where $c = \rho_{S11}$ of Eq.4.43.

With the help of the lemma, we can show that these two states are maximally spin-orbital entangled when $det(\boldsymbol{g}_S) = 0$.

Theorem 2. *Consider the reduced density matrices of the spin subsystem, $\rho_S, \bar{\rho}_S$, of the Kramers-paired bands corresponding to the irreducible representations in red along the directions $\overrightarrow{OA}$ as indicated in*

Table.4.1. Then

$$det(\boldsymbol{g}_S) = 0 \implies \mathcal{S}(\rho_S) = \mathcal{S}(\bar{\rho}_S) = 1, \tag{4.47}$$

where $\mathcal{S}(\rho_S) = -\operatorname{Tr}(\rho_S \log \rho_S)$ *is the entanglement entropy of the reduced density matrix of the spin subsystem.*

Proof. The spin g-tensor of these states can be decomposed according to Eq.4.28 as $\boldsymbol{g}_S = U\Sigma V$. We go to the coordinate system of the Bloch sphere such that in this transformed basis V is rotated away, i.e., $\boldsymbol{g}_S = U\Sigma$. This necessitates a change of basis of $|\xi\rangle$ and $|\bar{\xi}\rangle$ into $|\xi'\rangle$ and $|\bar{\xi}'\rangle$ by an $SU(2)$ transformation,

$$\begin{pmatrix} |\xi'\rangle \\ |\bar{\xi}'\rangle \end{pmatrix} = \begin{pmatrix} X & Y \\ -Y^* & X^* \end{pmatrix} \begin{pmatrix} |\xi\rangle \\ |\bar{\xi}\rangle \end{pmatrix} \tag{4.48}$$

where X and Y are complex amplitudes such that $|X|^2 + |Y|^2 = 1$. Equation 4.46 shows that for any X and Y this rotation does not affect the relation between ρ_S and $\bar{\rho}_S$. We choose X, Y to reflect the mapping $SU(2) \longrightarrow SO(3)$ [28],

$$V^{-1} = \begin{pmatrix} \operatorname{Re}(X^2 - Y^2) & \operatorname{Im}(X^2 + Y^2) & -2\operatorname{Re}(XY) \\ -\operatorname{Im}(X^2 - Y^2) & \operatorname{Re}(X^2 + Y^2) & 2\operatorname{Im}(XY) \\ 2\operatorname{Re}(XY^*) & 2\operatorname{Im}(XY^*) & |X|^2 - |Y|^2 \end{pmatrix}. \tag{4.49}$$

The total density matrices of the time-reversal pair $|\xi'\rangle$ and $|\bar{\xi}'\rangle$ are $\rho = |\xi'\rangle\langle\xi'|$, $\bar{\rho} = |\bar{\xi}'\rangle\langle\bar{\xi}'|$. Tracing out the orbital degrees of freedom leaves us with the reduced density matrices of the spin-subsystem, $\rho_S = \operatorname{Tr}_{orb}\rho = |\xi'_S\rangle\langle\xi'_S|$, $\bar{\rho}_S = \operatorname{Tr}_{orb}\bar{\rho} = |\bar{\xi}'_S\rangle\langle\bar{\xi}'_S|$.
The spin matrix from Eq.4.20 can be re-written as

$$S_i = \begin{pmatrix} \operatorname{Tr}|\xi'\rangle\langle\xi'|\,\sigma_i & \operatorname{Tr}|\xi'\rangle\langle\bar{\xi}'|\,\sigma_i \\ \operatorname{Tr}|\bar{\xi}'\rangle\langle\xi'|\,\sigma_i & \operatorname{Tr}|\bar{\xi}'\rangle\langle\bar{\xi}'|\,\sigma_i, \end{pmatrix}, \tag{4.50}$$

and the spin g-tensor has the form

$$\boldsymbol{g}_S = \begin{pmatrix} \operatorname{Tr}(|\xi'\rangle\langle\bar{\xi}'|\,\sigma_x + |\bar{\xi}'\rangle\langle\xi'|\,\sigma_x) & i\operatorname{Tr}(|\xi'\rangle\langle\bar{\xi}'|\,\sigma_x - |\bar{\xi}'\rangle\langle\xi'|\,\sigma_x) & \operatorname{Tr}_{spin}(\rho_S\sigma_x - \bar{\rho}_S\sigma_x) \\ \operatorname{Tr}(|\xi'\rangle\langle\bar{\xi}'|\,\sigma_y + |\bar{\xi}'\rangle\langle\xi'|\,\sigma_y) & i\operatorname{Tr}(|\xi'\rangle\langle\bar{\xi}'|\,\sigma_y - |\bar{\xi}'\rangle\langle\xi'|\,\sigma_y) & \operatorname{Tr}_{spin}(\rho_S\sigma_y - \bar{\rho}_S\sigma_y) \\ \operatorname{Tr}(|\xi'\rangle\langle\bar{\xi}'|\,\sigma_z + |\bar{\xi}'\rangle\langle\xi'|\,\sigma_z) & i\operatorname{Tr}(|\xi'\rangle\langle\bar{\xi}'|\,\sigma_z - |\bar{\xi}'\rangle\langle\xi'|\,\sigma_z) & \operatorname{Tr}_{spin}(\rho_S\sigma_z - \bar{\rho}_S\sigma_z) \end{pmatrix}. \tag{4.51}$$

The eigenvectors from Eq.4.48 along with the transformed spin matrix of Eq.4.50 give us the spin g-tensor in Eq.4.51. Recall that $\boldsymbol{g}_S = U\Sigma$ which means that up to a sign factor, $det(\boldsymbol{g}_S) = det(\Sigma)$. Recall also that Σ is the diagonal matrix of singular values in descending order. Since we have

$$det(\boldsymbol{g}_S) = det(\Sigma) = \Sigma_{xx}\Sigma_{yy}\Sigma_{zz} = 0, \tag{4.52}$$

then at least $\Sigma_{zz} = 0$, so that all the entries of the third column of $\boldsymbol{g}_S$) are zero. Thus,

$$\begin{aligned} &\mathrm{Tr}_{spin}(\rho_S\sigma_x - \bar{\rho}_S\sigma_x) = 0, \\ &\mathrm{Tr}_{spin}(\rho_S\sigma_y - \bar{\rho}_S\sigma_y) = 0, \\ &\mathrm{Tr}_{spin}(\rho_S\sigma_z - \bar{\rho}_S\sigma_z) = 0, \\ &\implies \rho_S - \bar{\rho}_S = 0. \end{aligned} \tag{4.53}$$

Now, combining $\rho_S = \bar{\rho}_S$ with $\bar{\rho}_S = \sigma_y\rho_S^T\sigma_y$ (lemma 1) gives

$$\rho_S = \bar{\rho}_S = \tfrac{1}{2}\mathbb{1}, \tag{4.54}$$

so that

$$\mathcal{S}(\rho_S) = \mathcal{S}(\bar{\rho}_S) = 1. \tag{4.55}$$

□

It should be noted that Theorem.2 applies not only to the three cubic point groups O_h, T_h and T_d, but also to various other non-cubic groups. We do not look at any other groups here since we are interested in applications of this theory to materials that belong to O_h and T_d. As can be noticed in Table.4.1, Theorem.2 does not apply at all to the groups T and O, because they do not have any directions in which pairs of states are degenerate, even taking time reversal into account. This has been verified using the method described in section 13.2 of [24]. We provide the analysis of this in the appendix.A.

We have shown that, due to Theorem.1, bands with certain symmetries necessarily have surfaces surrounding the Γ-point where $det(\boldsymbol{g}_S) = 0$. In the next chapter, we discuss the application of the theory of the $\boldsymbol{g}$-tensor to the important semiconductors silicon (Si), germanium (Ge) and gallium arsenide (GaAs). We also show the complex topologies of the surfaces of both $\boldsymbol{g}_S$ and $\boldsymbol{g} = \boldsymbol{g}_L + \boldsymbol{g}_S$ for important valence and conduction bands with the relevant symmetry in each of the three cases mentioned in the lemma. 1 above.

A

Analysis of groups T and O

As mentioned in [24], we would like to see if the irreducible representations of the groups T and O admit symmetry preserving transformation under the nonunitary group $\bar{G}$ which involves the operations u_i of the unitary group G and anti-unitary operations, θu_i where θ is a time-reversal operation. To refresh aspects of group theory, refer to chapter 2 section.2.3. Here we briefly remind the reader about the transformation of the representations under operations belonging to the non-unitary group.

A.1 Transformation of the representations under non-unitary operations

The transformation of the irreducible representations of the groups T and O under the unitary operations u_i, of the unitary group G, as well as under the anti-unitary operations θu_i (where $\theta^2 = -1$), determines whether they satisfy Theorem.2 (in chapter 4). In this section, we examine these transformations. As mentioned in the introduction, $\bar{G} = G + \theta G$, the non-unitary group comprising both unitary and anti-unitary operations. If we denote a as a general anti-unitary operator, then according to eq.13.22 of [24], the following equations must hold for the representation matrix $\hat{D}$,

1. $u_1 u_2 \phi_k = \sum_j \phi_j \left[\hat{D}(u_1)\hat{D}(u_2)\right]_{jk}$,
2. $ua\phi_k = \sum_j \phi_j \left[\hat{D}(u)\hat{D}(a)\right]_{jk}$,
3. $au\phi_k = \sum_j \phi_j \left[\hat{D}(a)\hat{D}(u)^*\right]_{jk}$,

4. $a_1 a_2 \phi_k = \sum_j \phi_j \left[\hat{D}(a_1)\hat{D}(a_2)^*\right]_{jk}$

where ϕ_i are the basis of the representation $\hat{D}$. The representation matrices of au and $a_1 a_2$ are not equal to the product of the matrices a, u and a_1, a_2 respectively. Such representations are called corepresentations of a non-unitary group. Two corepresentations D and D' are said to be equivalent if there exists a matrix T for which they satisfy:

$$\begin{aligned} \hat{D}'(u) &= \hat{T}^{-1}\hat{D}(u)\hat{T}, \\ \hat{D}'(a) &= \hat{T}^{-1}\hat{D}(a)\hat{T}^*. \end{aligned} \tag{A.1}$$

for all u and a. To construct an irreducible corepresentation D of $\bar{G}$ given an irreducible representation Δ with dimension d of the unitary subgroup G, we consider the basis $\psi_{j(j=1,\ldots,d)}$ such that $u\psi_k = \sum_{j=1}^{d} \psi_j \Delta_{jk}(u)$. If $\psi'_k = a_0\psi_k$ where a_0 is an anti-unitary operator, then $u\psi'_k = \sum_{j=1}^{d} \psi'_j \bar{\Delta}_{jk}(u)$ and we define $\bar{\Delta}$ as (eq.13.26 of [24])

$$\hat{\bar{\Delta}}(u) = \hat{\Delta}\left(a_0^{-1} u a_0\right)^*. \tag{A.2}$$

$\bar{\Delta}$ is also an irreducible representation of G. To get the irreducible corepresentation $\hat{D}$ of $\bar{G}$, we must consider the following cases.

1. If Δ and $\bar{\Delta}$ are equivalent then there exists a unitary U such that $\hat{\bar{\Delta}}(u) = \hat{U}^{-1}\hat{\Delta}(u)\hat{U}$. We define a quantity λ as $UU^* = \lambda\Delta(a_0^2)$. The irreducible corepresentation $\hat{D}$ of the non-unitary group $\bar{G}$ is related to Δ in the following way,
   - If $\lambda = +1$, $\hat{D}(u) = \hat{\Delta}(u), \hat{D}(a_0) = \hat{U}$.
   - If $\lambda = -1$, $\hat{D}(u) = \begin{pmatrix} \hat{\Delta}(u) & 0 \\ 0 & \hat{\Delta}(u) \end{pmatrix}, \hat{D}(a_0) = \begin{pmatrix} 0 & -\hat{U} \\ \hat{U} & 0 \end{pmatrix}$.
2. If $\hat{\Delta}(u)$ and $\hat{\bar{\Delta}}(u)$ are inequivalent, the irreducible corepresentation D of $\bar{G}$ is given by,

$$\hat{D} = \begin{pmatrix} \hat{\Delta}(u) & 0 \\ 0 & \hat{\bar{\Delta}}(u) \end{pmatrix}, \hat{D}(a_0) = \begin{pmatrix} 0 & \hat{\Delta}(a_0) \\ 1 & 0 \end{pmatrix}. \tag{A.3}$$

The derivations of the above cases have been discussed extensively in [24] on pages 297-298.

If $a_0 = \theta$, the time reversal operator then, following Eq.A.2,

$$\hat{\bar{\Delta}}(u) = \hat{\Delta}\left(\theta^{-1} u \theta\right)^* = \hat{\Delta}(u)^*. \tag{A.4}$$

In the cases of the groups T and O, finding representations that satisfy Eq.A.2 such that Δ and $\bar{\Delta}$ are equivalent, would imply these representations would be equivalent under an operator v_0 that

takes $\boldsymbol{k}$ to $-\boldsymbol{k}$ unitarily and returns to $\boldsymbol{k}$ by a succeeding time-reversal operation. The wavefunctions of the bands of these representations would then be related by the overall operation θa_0 and would admit maximal spin-orbit entanglement as per theorem. 2. This would also prohibit the bands from splitting.

A.2 Non-unitary operations on little groups

To determine whether Theorem 2 applies to the groups T and O, we focus solely on the spin density matrix of charge carriers in specific directions of $\boldsymbol{k}$-space. This requires a non-unitary transformation that acts only on the spin subspace of the representations of the little groups C_2, C_3, and C_4, as defined in Section 2.3.6. Therefore, it is sufficient to verify the $SU(2)$ form of Eq.A.4. The $SU(2)$ representation of a_0 must be the time reversal operation $\theta = i\sigma_y$ that takes $\boldsymbol{k}$ to $-\boldsymbol{k}$ and then brings it back to $\boldsymbol{k}$ by a unitary π-rotation $v_0 = \begin{pmatrix} i & 0 \\ 0 & -i \end{pmatrix}$ around the z-axis,

$$a_0 = v_0\theta = \begin{pmatrix} i & 0 \\ 0 & -i \end{pmatrix} i \begin{pmatrix} 0 & -i \\ i & 0 \end{pmatrix} \kappa = \begin{pmatrix} 0 & i \\ i & 0 \end{pmatrix} \kappa. \tag{A.5}$$

The $SU(2)$ matrix form of v_0 is easily obtained from subsection.2.3.4, Eq.2.14 . Since we want to understand how a_0 acts on the elements of the little groups, which, for the basis states $\phi(1/2, 1/2)$ and $\phi(1/2, -1/2)$ are diagonal matrices, we will look at the transformation of a general 2×2 diagonal matrix, $U = \begin{pmatrix} a & 0 \\ 0 & b \end{pmatrix}$ first.

$$\begin{aligned} a_0^{-1} U a_0 &= \kappa \begin{pmatrix} 0 & -i \\ -i & 0 \end{pmatrix} \begin{pmatrix} a & 0 \\ 0 & b \end{pmatrix} \begin{pmatrix} 0 & i \\ i & 0 \end{pmatrix} \kappa \\ &= \kappa \begin{pmatrix} 0 & -i \\ -i & 0 \end{pmatrix} \begin{pmatrix} 0 & ia \\ ib & 0 \end{pmatrix} = \kappa \begin{pmatrix} b & 0 \\ 0 & a \end{pmatrix} = \begin{pmatrix} b^* & 0 \\ 0 & a^* \end{pmatrix}. \end{aligned} \tag{A.6}$$

Note that the transformations $a_0^{-1} E a_0$ and $a_0^{-1} \bar{E} a_0$ are trivial so we do not explicitly show them.

We look at these little groups individually,

1. *Little group* C_2:
   The character table for the little group C_2 is [26],

	E	$\bar{E}$	C_2	$\bar{C}_2$	Time Inv.	Bases
Γ_3	1	-1	i	$-i$	b	$\phi\,(1/2, 1/2)$
Γ_4	1	-1	$-i$	i	b	$\phi\,(1/2, -1/2)$

We recognize that the unitary elements U of C_2 are:

$$C_2 = \begin{pmatrix} i & 0 \\ 0 & -i \end{pmatrix}, \bar{C}_2 = \begin{pmatrix} -i & 0 \\ 0 & i \end{pmatrix}. \tag{A.7}$$

The matrix C_2 can be obtained for the spin direction vector, $\boldsymbol{n}_{C_2} = (0,0,1)$ and angle $\phi_{C_2} = \pi$, using the method described in subsection.2.3.4, eqn.2.14. We identify a and b for each of the case.

$U = \begin{pmatrix} a & 0 \\ 0 & b \end{pmatrix}$	a	b	a^*	b^*	$a_0^{-1} U a_0 = \begin{pmatrix} b^* & 0 \\ 0 & a^* \end{pmatrix}$
C_2	i	$-i$	$-i$	i	C_2
$\bar{C}_2$	$-i$	i	i	$-i$	$\bar{C}_2$

The representations Γ_3 and Γ_4 map onto themselves after the operation a_0 and are not equivalent. Therefore the corepresentation matrix of $\bar{G} = \theta C_2$ as shown in A.1.2 will be,

$$\hat{D} = \begin{pmatrix} \Gamma_3 & 0 \\ 0 & \Gamma_4 \end{pmatrix}. \tag{A.8}$$

2. *Little group C_3*:
The character table for the little group C_3 is [26],

	E	$\bar{E}$	C_3	$\bar{C}_3$	C_3^{-1}	$\bar{C}_3^{-1}$	Time Inv.	Bases
Γ_4	1	-1	ω	$-\omega$	$-\omega^2$	ω^2	b	$\phi\,(1/2, 1/2)$
Γ_5	1	-1	$-\omega^2$	ω^2	ω	$-\omega$	b	$\phi\,(1/2, -1/2)$

We recognize that the unitary elements U of C_3 are:

$$C_3 = \begin{bmatrix} \omega & 0 \\ 0 & -\omega^2 \end{bmatrix}, \bar{C}_3 = -C_3, C_3^{-1} = \begin{bmatrix} -\omega^2 & 0 \\ 0 & \omega \end{bmatrix}, \bar{C}_3^{-1} = -C_3^{-1}, \tag{A.9}$$

where $\omega = e^{i\pi/3}$. The matrix C_3 can be obtained for the spin direction vector, $\boldsymbol{n}_{C_3} = (0,0,1)$ and angle $\phi_{C_3} = \frac{2\pi}{3}$, using the method described in subsection.2.3.4, eqn.2.14. We identify a and b for each of the case.

$U = \begin{pmatrix} a & 0 \\ 0 & b \end{pmatrix}$	a	b	a^*	b^*	$a_0^{-1} U a_0 = \begin{pmatrix} b^* & 0 \\ 0 & a^* \end{pmatrix}$
C_3	ω	$-\omega^2$	$-\omega^2$	ω	C_3
$\bar{C}_3^{-1}$	$-\omega^2$	ω	ω	$-\omega^2$	$\bar{C}_3^{-1}$

The representation Γ_4 and Γ_5 are inequivalent as $a_0^{-1}\Gamma_4 a_0 = \Gamma_4$ and $a_0^{-1}\Gamma_5 a_0 = \Gamma_5$.Therefore the corepresentation matrix of $\bar{G} = \theta C_3$ as shown in A.1.2 will be,

$$\hat{D} = \begin{pmatrix} \Gamma_4 & 0 \\ 0 & \Gamma_5 \end{pmatrix}. \tag{A.10}$$

3. *Little group* C_4:
The character table for the little group C_4 is [26],

	E	$\bar{E}$	C_4	$\bar{C}_4$	C_2	C_2	C_4^{-1}	$\bar{C}_4^{-1}$	Time Inv.	Bases
Γ_5	1	-1	ω	$-\omega$	i	$-i$	$-\omega^3$	ω	b	$\phi\,(1/2, 1/2)$
Γ_6	1	-1	$-\omega^3$	ω^3	$-i$	i	ω	$-\omega^3$	b	$\phi\,(1/2, -1/2)$

We recognize that the unitary elements U of C_4 are:

$$C_4 = \begin{pmatrix} \omega & 0 \\ 0 & -\omega^3 \end{pmatrix}, \bar{C}_4 = -C_4, C_4^{-1} = \begin{pmatrix} -\omega^3 & 0 \\ 0 & \omega \end{pmatrix}, \bar{C}_4^{-1} = -C_4^{-1}C_2 = \begin{pmatrix} -i & 0 \\ 0 & i \end{pmatrix}, \bar{C}_2 = -C_2. \tag{A.11}$$

where $\omega = e^{i\pi/4}$. The matrix C_4 can be obtained for the spin direction vector, $\boldsymbol{n}_{C_4} = (0, 0, 1)$ and angle $\phi_{C_4} = \frac{\pi}{2}$, using the method described in subsection.2.3.4, eqn.2.14. We identify a and b for each of the case.

$U = \begin{pmatrix} a & 0 \\ 0 & b \end{pmatrix}$	a	b	a^*	b^*	$a_0^{-1}Ua_0 = \begin{pmatrix} b^* & 0 \\ 0 & a^* \end{pmatrix}$
C_4	ω	$-\omega^3$	$-\omega^3$	ω	C_4
$\bar{C}_4^{-1}$	$-\omega^3$	ω	ω	$-\omega^3$	$\bar{C}_4^{-1}$

The representations of the ϕ-spinors are inequivalent, $a_0^{-1}\Gamma_5 a_0 = \Gamma_5$ and $a_0^{-1}\Gamma_6 a_0 = \Gamma_6$. Therefore the corepresentation matrix of $\bar{G} = \theta C_4$ as shown in A.1.2 will be,

$$\hat{D} = \begin{pmatrix} \Gamma_5 & 0 \\ 0 & \Gamma_6 \end{pmatrix}. \tag{A.12}$$

In conclusion, we see that the spinor states are not doubly degenerate in any of the little groups C_2, C_3, C_4. This means that we see $\boldsymbol{k} \xrightarrow{\theta} -\boldsymbol{k} \xrightarrow{v_0} \boldsymbol{k}$, in other words Eq.4.10, along no directions for the groups T and O and the representations do not admit maximal spin-orbit entanglement.

Bibliography

[1] X. Fan, T. G. Myers, B. A. D. Sukra, and G. Gabrielse. Measurement of the electron magnetic moment. *Phys. Rev. Lett.*, 130:071801, Feb 2023. doi: 10.1103/PhysRevLett.130.071801. URL https://link.aps.org/doi/10.1103/PhysRevLett.130.071801.

[2] J. M. Elzerman, R. Hanson, J. S. Greidanus, L. H. Willems van Beveren, S. De Franceschi, L. M. K. Vandersypen, S. Tarucha, and L. P. Kouwenhoven. Few-electron quantum dot circuit with integrated charge read out. *Phys. Rev. B*, 67:161308, Apr 2003. doi: 10.1103/PhysRevB.67.161308. URL https://link.aps.org/doi/10.1103/PhysRevB.67.161308.

[3] N. W. Hendrickx, L. Massai, M. Mergenthaler, F. J. Schupp, S. Paredes, S. W. Bedell, G. Salis, and A. Fuhrer. Sweet-spot operation of a germanium hole spin qubit with highly anisotropic noise sensitivity. *Nature Materials*, 23(7):920–927, May 2024. ISSN 1476-4660. doi: 10.1038/s41563-024-01857-5. URL http://dx.doi.org/10.1038/s41563-024-01857-5.

[4] Chithra H Sharma, Appanna Parvangada, Lars Tiemann, Kai Rossnagel, Jens Martin, and Robert H Blick. Resistively detected electron spin resonance and g factor in few-layer exfoliated mos2 devices. *arXiv preprint arXiv:2410.18758*, 2024.

[5] Till Andlauer and Peter Vogl. Electrically controllable g tensors in quantum dot molecules. *Phys. Rev. B*, 79:045307, Jan 2009. doi: 10.1103/PhysRevB.79.045307. URL https://link.aps.org/doi/10.1103/PhysRevB.79.045307.

[6] Chien-An Wang, Valentin John, Hanifa Tidjani, Cécile X. Yu, Alexander S. Ivlev, Corentin Déprez, Floor van Riggelen-Doelman, Benjamin D. Woods, Nico W. Hendrickx, William I. L. Lawrie, Lucas E. A. Stehouwer, Stefan D. Oosterhout, Amir Sammak, Mark Friesen, Giordano Scappucci, Sander L. de Snoo, Maximilian Rimbach-Russ, Francesco Borsoi, and Menno Veldhorst. Operating semiconductor quantum processors with hopping spins. *Science*, 385 (6707):447–452, 2024. doi: 10.1126/science.ado5915. URL https://www.science.org/doi/abs/10.1126/science.ado5915.

[7] Daniel Jirovec, Philipp M. Mutter, Andrea Hofmann, Alessandro Crippa, Marek Rychetsky, David L. Craig, Josip Kukucka, Frederico Martins, Andrea Ballabio, Natalia Ares, Daniel Chrastina, Giovanni Isella, Guido Burkard, and Georgios Katsaros. Dynamics of hole singlet-triplet qubits with large g-factor differences. *Phys. Rev. Lett.*, 128:126803, Mar 2022. doi: 10.1103/PhysRevLett.128.126803. URL https://link.aps.org/doi/10.1103/PhysRevLett.128.126803.

[8] Daniel Jirovec, Andrea Hofmann, Andrea Ballabio, Philipp M Mutter, Giulio Tavani, Marc Botifoll, Alessandro Crippa, Josip Kukucka, Oliver Sagi, Frederico Martins, et al. A singlet-triplet hole spin qubit in planar ge. *Nature materials*, 20(8):1106–1112, 2021.

[9] Philipp M. Mutter and Guido Burkard. All-electrical control of hole singlet-triplet spin qubits at low-leakage points. *Phys. Rev. B*, 104:195421, Nov 2021. doi: 10.1103/PhysRevB.104.195421. URL https://link.aps.org/doi/10.1103/PhysRevB.104.195421.

[10] Mitchell Brickson, N Tobias Jacobson, Andrew J Miller, Leon N Maurer, Tzu-Ming Lu, Dwight R Luhman, and Andrew D Baczewski. Using a high-fidelity numerical model to infer the shape of a few-hole ge quantum dot. *arXiv preprint arXiv:2408.14422*, 2024.

[11] J. M. Luttinger. Quantum theory of cyclotron resonance in semiconductors: General theory. *Phys. Rev.*, 102:1030–1041, May 1956. doi: 10.1103/PhysRev.102.1030. URL https://link.aps.org/doi/10.1103/PhysRev.102.1030.

[12] Y. Yafet. *g Factors and Spin-Lattice Relaxation of Conduction Electrons*, volume 14 of *Solid State Physics*. Academic Press, 1963. doi: https://doi.org/10.1016/S0081-1947(08)60259-3. URL https://www.sciencedirect.com/science/article/pii/S0081194708602593.

[13] Peter Y Yu and Manuel Cardona. *Fundamentals of semiconductors*, volume 619. Springer, 2005.

[14] Anatole Abragam and Brebis Bleaney. *Electron paramagnetic resonance of transition ions*. Clarendon Press, 1970.

[15] C. Gradl, R. Winkler, M. Kempf, J. Holler, D. Schuh, D. Bougeard, A. Hernández-Mínguez, K. Biermann, P. V. Santos, C. Schüller, and T. Korn. Asymmetric g tensor in low-symmetry two-dimensional hole systems. *Phys. Rev. X*, 8:021068, Jun 2018. doi: 10.1103/PhysRevX.8.021068. URL https://link.aps.org/doi/10.1103/PhysRevX.8.021068.

[16] L. A. Yeoh, A. Srinivasan, O. Klochan, R. Winkler, U. Zülicke, M. Y. Simmons, D. A. Ritchie, M. Pepper, and A. R. Hamilton. Noncollinear paramagnetism of a gaas two-dimensional hole system. *Phys. Rev. Lett.*, 113:236401, Dec 2014. doi: 10.1103/PhysRevLett.113.236401. URL https://link.aps.org/doi/10.1103/PhysRevLett.113.236401.

[17] Dimitrie Culcer, Yugui Yao, and Qian Niu. Coherent wave-packet evolution in coupled bands. *Phys. Rev. B*, 72:085110, Aug 2005. doi: 10.1103/PhysRevB.72.085110. URL https://link.aps.org/doi/10.1103/PhysRevB.72.085110.

[18] Ming-Che Chang and Qian Niu. Berry phase, hyperorbits, and the hofstadter spectrum: Semiclassical dynamics in magnetic bloch bands. *Phys. Rev. B*, 53:7010–7023, Mar 1996. doi: 10.1103/PhysRevB.53.7010. URL https://link.aps.org/doi/10.1103/PhysRevB.53.7010.

[19] Di Xiao, Ming-Che Chang, and Qian Niu. Berry phase effects on electronic properties. *Rev. Mod. Phys.*, 82:1959–2007, Jul 2010. doi: 10.1103/RevModPhys.82.1959. URL https://link.aps.org/doi/10.1103/RevModPhys.82.1959.

[20] T Thonhauser. Theory of orbital magnetization in solids. *International Journal of Modern Physics B*, 25(11):1429–1458, 2011. URL https://api.semanticscholar.org/CorpusID:119292686. esp. eq.41.

[21] Simon L Altmann and Peter Herzig. Point-group theory tables, 1994. URL https://www.theochem.ru.nl/files/local/altmann-2011.pdf. 2nd Ed. (corrected), 2011, Wien.

[22] R. J. Elliott. Spin-orbit coupling in band theory—character tables for some "double" space groups. *Phys. Rev.*, 96:280–287, Oct 1954. doi: 10.1103/PhysRev.96.280. URL https://link.aps.org/doi/10.1103/PhysRev.96.280.

[23] N.W. Ashcroft and N.D. Mermin. *Solid State Physics*. HRW international editions. Holt, Rinehart and Winston, 1976. ISBN 9780030839931. URL https://books.google.de/books?id=1C9HAQAAIAAJ.

[24] Teturo Inui, Yukito Tanabe, and Yositaka Onodera. *Group theory and its applications in physics*, volume 78. Springer Science & Business Media, 2012. See sections 13.2 and 13.3.

[25] Robert G Littlejohn. Time reversal, 2019. URL https://bohr.physics.berkeley.edu/classes/221/1112/notes/timerev.pdf.

[26] George F. Koster, John O. Dimmock, and Robert G. Wheeler. *The Properties of the Thirty-Two Point Groups*. MIT Press, 1963. URL https://babel.hathitrust.org/cgi/pt?id=mdp.39015022422318&view=1up&seq=7.

[27] M.S. Dresselhaus, G. Dresselhaus, and A. Jorio. *Group Theory: Application to the Physics of Condensed Matter*. Springer Berlin Heidelberg, 2007. ISBN 9783540328971. URL https://books.google.de/books?id=sKaH8vrfmnQC.

[28] DB Westra. Su (2) and so (3), 2008. URL https://www.mat.univie.ac.at/~westra/so3su2.pdf.

5

Application of the g-tensor formalism to semiconductors

5.1 Introduction

The g-factors of important semiconductors such as silicon (Si), germanium (Ge) and gallium-arsenide (GaAs) have already been calculated long ago [1–3]. We consider here these three semiconductors not just because they are important for classical computation but also because they have become materials of interest for quantum computation. Here we show these results for the g-factors again but with an emphasis on the topological features of the g-factor zeros in different important bands and the resulting spin-orbit entanglement properties of the band eigenstates. The topological aspects of silicon have been explored earlier [4]. We work within the tight-binding formalism. Since we are only concerned with the topology, the ab-initio accuracy is not necessary.

5.2 Model Hamiltonian

We use the $sp^3d^5s^*$ tight-binding Hamiltonian [5–7] which is quite an accurate model for fitting the energy bands of Si and Ge. But it is an open question whether this model is equally accurate for other purposes. This is a twenty-band model, ten orbitals for each atom in the unit cell each with two-spins. For the bulk semiconductors, as shown by Chadi [8], this Hamiltonian has on-site energies along the diagonal and has off-diagonal interaction terms. The spin-orbit interactions occurs between $p_{x,\sigma}$ and $p_{y,\sigma}$ orbitals of the same spin σ, $\langle p_{x,\sigma}| H_{SO} |p_{y,\sigma}\rangle$ and between $p_{x/y,\sigma}$ and

$p_{z\sigma'}$ of different spins $\{\sigma, \sigma'\}$, $\langle p_{x/y,\sigma}| H_{SO} |p_{z,\sigma'}\rangle$,

$$\begin{aligned}
\left\langle \boldsymbol{p}_x \uparrow |H_{SO}| \boldsymbol{p}_y \uparrow \right\rangle &= \left\langle \boldsymbol{p}_y \uparrow |H_{SO}| \boldsymbol{p}_x \uparrow \right\rangle^* = i\lambda_c, \\
\langle \boldsymbol{p}_x \uparrow |H_{SO}| \boldsymbol{p}_z \downarrow \rangle &= -\langle \boldsymbol{p}_z \uparrow |H_{SO}| \boldsymbol{p}_x \uparrow \rangle = \lambda_c, \\
\left\langle \boldsymbol{p}_y \uparrow |H_{SO}| \boldsymbol{p}_z \downarrow \right\rangle &= -\left\langle \boldsymbol{p}_z \uparrow |H_{SO}| \boldsymbol{p}_y \downarrow \right\rangle = -i\lambda_c,
\end{aligned} \tag{5.1}$$

where λ_c is the Chadi spin-orbit parameter. The spin-orbit interacting between the d-orbitals is usually much smaller than that between the p-orbitals and is therefore neglected. We use the parameters as given in [9]. The band structures for both Si and Ge are quite precise as can be seen in Fig.5.1.

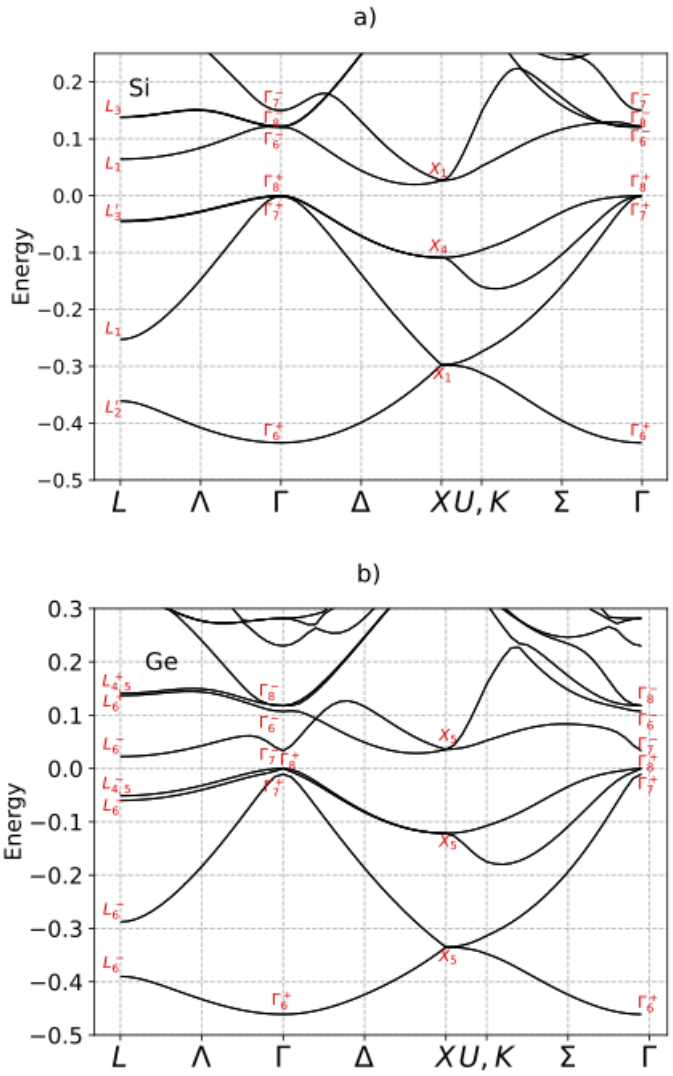

Figure 5.1: (a) The band-structure of silicon. (b) The band-structure of germanium. The red labels are the irreducible representations of the band states at $\mathbf{\Gamma}$, taking spin-orbit coupling into account; see Table 4.1. Energies are in atomic Hartree units.

In Fig.5.1, one can see all the band labels clearly. For silicon, at the Γ-point, bands Γ_5^+ and Γ_4^- split into Kramers-degenerate pairs $\Gamma_5^+ \rightarrow \Gamma_7^+ \oplus \Gamma_8^+$ and $\Gamma_4^- \rightarrow \Gamma_6^- \oplus \Gamma_8^-$. Recall that Γ_7^+ and Γ_6^- are spin-degenerate Kramers-pair bands, the other bands may have multiple degeneracy. Since the spin-orbit interaction is quite small, these splittings are barely noticeable. As for germanium, the spin-orbit interaction, though small, is still larger than silicon. The splitting of the bands is more obvious in this case. Notice that the band Γ_7^- is isolated from the other bands but it does not belong to any of the symmetry classes as described in lemma.1. The band of our interest is still the band labeled Γ_6^-, it does not have any other accidental degeneracy than Kramers-degeneracy.

5.3 Treatment of the momentum matrix element

As seen before, we need to calculate the momentum matrix elements in order to determine the g-tensor. The relation between the momentum matrix element and the Hamiltonian has been discussed in [10]. It is important to take into account the non-zero contributions of the intra-atomic term,

$$\langle u_n(\boldsymbol{k})|\boldsymbol{\pi}|u_m(\boldsymbol{k})\rangle = \frac{m}{\hbar}\sum_{\alpha,\beta} a_n^{\alpha *} a_m^{\beta} \nabla_{\boldsymbol{k}} \langle\alpha|H|\beta\rangle + \sum_{\alpha,\beta} a_n^{\alpha *} a_m^{\beta} \langle\alpha|\boldsymbol{d}|\beta\rangle (E_n - E_m). \tag{5.2}$$

Eq.5.2 shows the momentum matrix element between the Bloch states $|u_n(\boldsymbol{k})\rangle = \sum_\alpha a_n^\alpha |\alpha\rangle$ and $|u_m(\boldsymbol{k})\rangle = \sum_\beta a_m^\beta |\beta\rangle$ where α, β are orbital indices and $\boldsymbol{d}$ is the position operator. Notice that the second term in Eq.5.2 cannot be ignored as that would imply that in a periodic system of well-separated atoms, the momentum matrix elements are zero as the gradient term vanishes because of no overlap between orbitals.

To calculate the orbital magnetic moment contribution $\boldsymbol{g}_L$ we must have values for the matrix elements $\boldsymbol{d}_{\alpha\beta} = \langle\alpha|\boldsymbol{d}|\beta\rangle$ with the orbital indices α, β. $\boldsymbol{d}_{\alpha\beta}$ is generally not diagonal in the orbital index [10]. The non-zero cases are determined by symmetry. From the $\Delta l = \pm 1$ selection rule we know that the principal off-diagonal contribution will be between s and p orbitals. These matrix elements are needed for describing the intra-atomic transitions. In previous tight-binding studies, these have been fit to the optical properties of the bulk semiconductors [11].

We choose to fit the position matrix elements to the Landé g-factor in the atomic limit. The g-factor expression for isolated atoms is given by the Landé theory,

$$g_J = \frac{1}{2}\left(1 + \frac{L(L+1) - S(S+1)}{J(J+1)}\right) + \frac{g_0}{2}\left(1 - \frac{L(L+1) - S(S+1)}{J(J+1)}\right) = +\frac{2}{3}, \tag{5.3}$$

where g_0 is the vacuum electron g-factor. Recall that the bands we consider here are the bands dispersed by $L = 1, S = \frac{1}{2}, J = \frac{1}{2}$ states. Within our tight binding model in the atomic limit, this value of $g_J = +\frac{2}{3}$ occurs when $\langle s|\boldsymbol{d}|p_i\rangle_{Si} = 2.788$ for an isolated Si and $\langle s|\boldsymbol{d}|p_i\rangle_{Ge} = 2.535$ for an

isolated Ge. This is shown in Fig.5.2.a) for Si and Fig.5.2.b) for Ge. Values are given in respective atomic units (a_0) in both cases. Notice that at $\langle \boldsymbol{d} \rangle = 0$, the singular value of $\boldsymbol{g}_S + \boldsymbol{g}_L$, $\Sigma_{zz} = +\frac{2}{3}$ but $det(\boldsymbol{g}_S + \boldsymbol{g}_L) < 0$. The appearance of the kink in both cases is connected to the change in the sign of the determinant as mentioned previously. We choose the value of $\langle \boldsymbol{d} \rangle$ such that $\Sigma_{zz} = +\frac{2}{3}$ and $det(\boldsymbol{g}_S + \boldsymbol{g}_L) > 0$.

We do a similar fit for GaAs. In this case, each of the two atoms, Ga and As, has its own intra-atomic contribution; fitting again to the Landé value gives $\langle s|\boldsymbol{d}|p_i\rangle_{Ga} = 2.891$, $\langle s|\boldsymbol{d}|p_i\rangle_{As} = 2.455$.

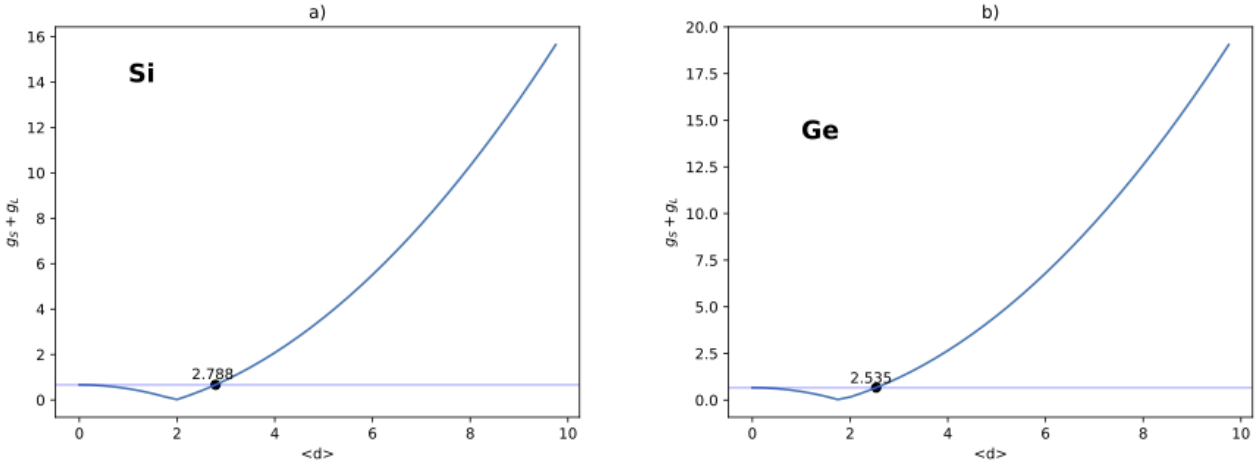

Figure 5.2: Intra-atomic terms for Si(a) and Ge(b) fit according to the atomic limit. At $\langle \boldsymbol{d} \rangle = 0$, the singular value of $\boldsymbol{g}_S + \boldsymbol{g}_L$, $\Sigma_{zz} = +\frac{2}{3}$ but $det(\boldsymbol{g}_S + \boldsymbol{g}_L) < 0$. We choose the value of $\langle \boldsymbol{d} \rangle$ which corresponds to a positive value of the determinant.

5.4 Calculation of the g-factor

Now that we have all the components, we proceed to calculate the two contributions to the total $\boldsymbol{g}$-tensor according to Eq.4.21 and Eq.4.27 for bulk silicon, germanium as well as for gallium-arsenide. As mentioned earlier, the choice of $\boldsymbol{g}_{tot}$ is not unique so we instead choose to look at the eigenvalues of $\boldsymbol{G}$ which was first introduced in Eq.4.17.

5.4.1 Singular values of the g-tensor

We remind the reader that the important eigenstate pairs for which the results of theorems 1 and 2 can be seen are $\left|\xi_{\Gamma_7^+}\right\rangle$-$\left|\bar{\xi}_{\Gamma_7^+}\right\rangle$ (the split-off valence band) and $\left|\xi_{\Gamma_6^-}\right\rangle$-$\left|\bar{\xi}_{\Gamma_6^-}\right\rangle$ (a low lying conduction band). Such bands show that the g-factor changes its sign as we move away from the Γ-point.

Let us consider the lowest conduction band in the case of silicon as it disperses from the $\left|\xi_{\Gamma_6^-}\right\rangle, \left|\bar{\xi}_{\Gamma_6^-}\right\rangle$ states. We plot the singular values of $\boldsymbol{g}_S$ and $\boldsymbol{g}_{tot}$ for silicon (shown in Fig. 5.3), which we have now calculated, in an arbitrary direction going outward from the Γ-point. We see a high anisotropy in the g-factor values as we do not go along a specific symmetry direction.

At the Γ-point, $\boldsymbol{g}_S$ (Fig. 5.3) must have isotropic singular-values, $\Sigma_{xx} = \Sigma_{yy} = \Sigma_{zz}$, and they are indeed $\Sigma_{xx} = \frac{2}{3}, \Sigma_{yy} = \frac{2}{3}, \Sigma_{zz} = \frac{2}{3}$. Note that the singular values are by construction always positive. In Fig.5.3, we see at least one value Σ_{zz} goes to 0 which means a sign change has occurred. In order to determine the sign of the g-factors, we must look at the determinant. As discussed before, the determinant of the $\boldsymbol{g}$-tensor is an invariant quantity. The red dashed curve shows that $det(\boldsymbol{g}_S)$ starts at $-\frac{8}{27}$, crosses zero at the point where at least one singular value goes to zero (exactly one, in this case), and asymptotes eventually to $+8$.

5.4.2 Determining the zero-crossing surface

Let us call the point at which at least one singular value of $\boldsymbol{g}_S$, Σ_{zz} goes to 0 as $\boldsymbol{k} \to \boldsymbol{k}_c$, assuming that the spin-orbit interaction is "small enough" (as shown in thm.1). This may happen an odd number of times. In Fig.5.3, we have shown this for one direction but we observe that this occurs in all $\boldsymbol{k}$ directions starting at the Γ-point, forming one or more smooth surfaces surrounding it. As we know, the singular value going to 0 is directly related to $det(\boldsymbol{g}_S) = \Sigma_{xx}\Sigma_{yy}\Sigma_{zz} = 0$. For any band n as described in def.1, these surfaces are given by $det\left(\boldsymbol{g}_S\left(\boldsymbol{k}_c\right)\right) = 0$. These can be as complex as fermi surfaces $E_n(\boldsymbol{k}_F) = E_F$ and will have the same cubic symmetry. Similar techniques as the ones used to find the Fermi surfaces can be employed to find these surfaces of zero-crossings of the determinant. In the following, we will discuss one such method that we implemented.

Fig.5.3 shows the singular values plotted as the blue curves and the determinants of $\boldsymbol{g}_S$ and $\boldsymbol{g}_{tot}$ plotted are the red dashed curves. In Fig.5.3.a), at the Γ-point i.e $|\boldsymbol{k}| = 0$, $\Sigma_{xx} = \Sigma_{yy} = \Sigma_{zz} = \frac{2}{3}$ and $det(\boldsymbol{g}_S) = -\frac{8}{27}$ and further away, $\Sigma_{xx} = \Sigma_{yy} = \Sigma_{zz} = 2$ and $det(\boldsymbol{g}_S) = 8$. Similarly, Fig.5.3.b) shows the singular values and the determinant of $\boldsymbol{g}_{tot}$. One thing to notice here is that two of the singular values go to 0 resulting in $det(\boldsymbol{g}_{tot}) = 0$ multiple times. This is because for $\boldsymbol{g}_{tot}$ we have now taken into account two contributions $\boldsymbol{g}_S$ and $\boldsymbol{g}_L$. The bands approaching each other can also cause the energy denominator in Eq.4.23 and *Eq.*4.24 to become quite small and the Berry curvature contributions to shoot up.

Connection to linear algebra

We refer back to the singular-value decomposition of the $\boldsymbol{g}$-tensor in Eq.4.28. The $\boldsymbol{g}$-tensor is a real square matrix, U and V can be chosen to be real orthogonal matrices. The singular value matrix Σ is a positive diagonal matrix which means $det(\Sigma) \geq 0$. This means that the information of the

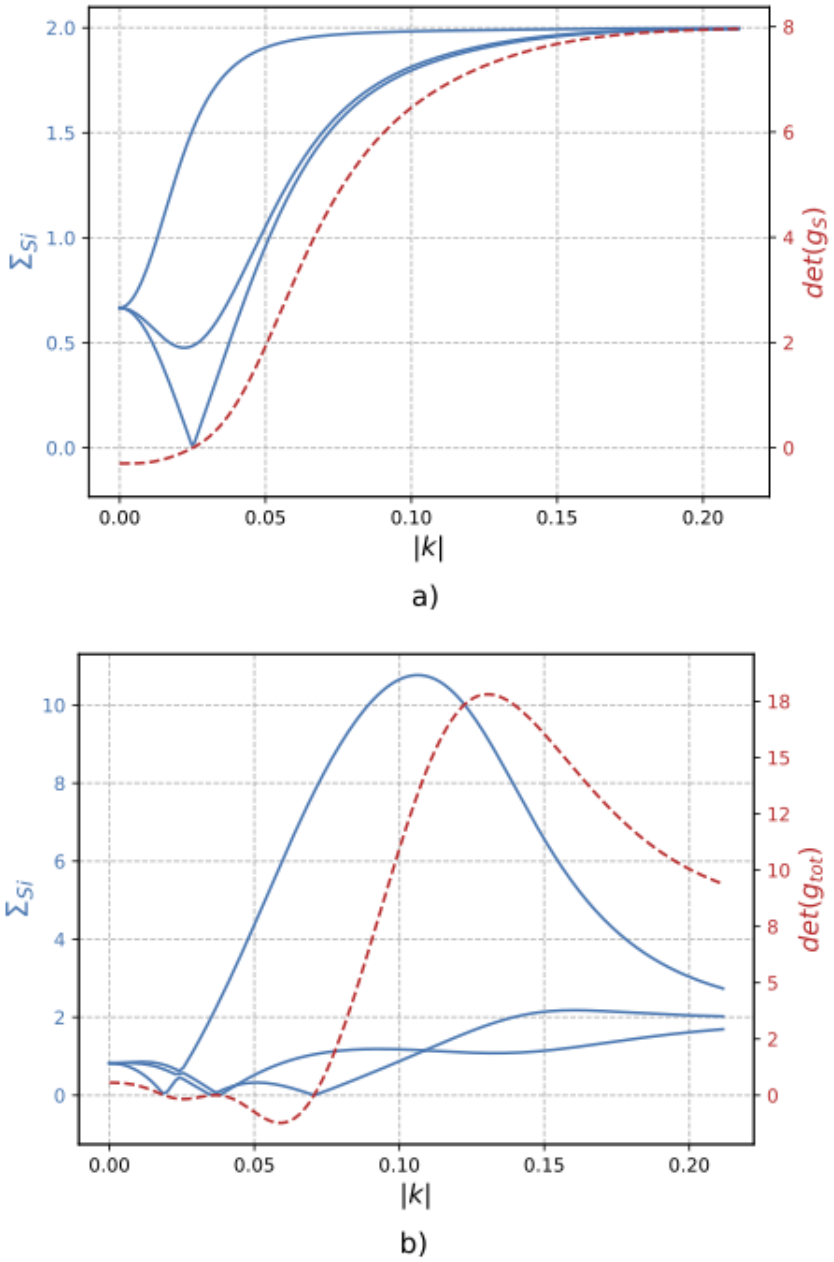

Figure 5.3: Occurrence of zeros in g-factors, as seen in the singular values of the g-tensor (blue), for the first conduction band of Si. These singular values (by definition non-negative) are calculated in an arbitrary direction to highlight the anisotropy. The red dashed curve is the evolution of the determinant of the g-tensor. Panel a) shows the singular values and the determinant of only the spin contribution to the g-tensor, g_S. The singular values start at 2/3 and converge to 2 which is what we must observe for Si. Panel b) shows the singular values and the determinant of $\boldsymbol{g}_{tot} = \boldsymbol{g}_L + \boldsymbol{g}_S$. The change in the sign of the determinant is a clear indication of the change in the sign of the g-factors. $|k|$ is given in inverse atomic units, a_0^{-1}.

sign of the g-tensor comes from U and V,

$$sgn(det(\boldsymbol{g}_S)) = det(U) \cdot det(V). \tag{5.4}$$

The determinants $det(U)$ and $det(V)$ are either -1 or $+1$. Thus, the change in the sign of the g-tensor is determined by the product of the two determinants of these real orthogonal matrices U and V. We leverage this and simplify this further by making a change of basis as described in thm.2 and set $V = \mathbb{I}$. Eq.5.4 then becomes $sgn(det(\boldsymbol{g}_S)) = det(U)$. Note that the form in Eq.5.4 is the most generic form for any direction in $\boldsymbol{k}$-space.

Binary search method

One way to come arbitrarily close to $\boldsymbol{k}_c$ would be by using a fast converging algorithm such as the binary search. The binary search algorithm works by halving the intervals of search, thus reducing the compute times. In our case, we provide the algorithm with an interval with a starting point, $\boldsymbol{k}_{start}$ and an ending point, $\boldsymbol{k}_{end}$. The algorithm would then compute the middle point of this interval, $\boldsymbol{k}_{mid}$ and calculate the sign of $det(\boldsymbol{g}_S(\boldsymbol{k}_{mid}))$ at this point. The new starting or ending point would be chosen based on which of the two $det(\boldsymbol{g}_S(\boldsymbol{k}_{start}))$ or $det(\boldsymbol{g}_S(\boldsymbol{k}_{end}))$ have the same sign as $det(\boldsymbol{g}_S(\boldsymbol{k}_{mid}))$. The interval is then halved. Remark that it is only possible to get to a value of $\boldsymbol{k}_c$ with a certain cut-off precision. In our case, it is not necessary to determine $\boldsymbol{k}_c$ extremely precisely because we are only interested in the topology of the surfaces formed by $\boldsymbol{k}_c$. The starting interval must be chosen carefully: there must be only one zero crossing in an interval otherwise there are chances of the other zero crossings to be missed or the algorithm to fail.

We provide a pseudocode, algorithm.1, which was used in this work. Here, $funcg_S$ refers to a function that calculates the determinant of g_S and ϵ an arbitrary value of how close we'd like the determinant to be to 0:

Note that we have calculated $\boldsymbol{k}_c$ at which $|det(\boldsymbol{g}_S(\boldsymbol{k}_c))| \leq \epsilon$ where ϵ is arbitrarily close to 0 but we will continue to call this point as the point where $det(\boldsymbol{g}_S(\boldsymbol{k}_c)) = 0$.

5.4.3 Determining the entanglement

Now that we have the points $\boldsymbol{k}_c$ at which $det(\boldsymbol{g}_S) = 0$, we will proceed to determine the entanglement of the states $|\xi\rangle$ and $|\bar{\xi}\rangle$ at this point.

To calculate the entanglement entropy of the band-pair with the eigenstates $\left|\xi_{\Gamma_7^+}(\boldsymbol{k}_c)\right\rangle, \left|\bar{\xi}_{\Gamma_7^+}(\boldsymbol{k}_c)\right\rangle$, we would like to ensure that we are working with the states that are on the poles of the Bloch sphere. For this we rotate the states according to Eq.4.48 such that $V = \mathbb{I}$ from Eq.4.49. We calculate the reduced spin-density matrices of the rotated states,

$$\rho_S = \mathrm{Tr}_{orb}\left(\left|\xi'_{\Gamma_7^+}(\boldsymbol{k}_c)\right\rangle\left\langle\xi'_{\Gamma_7^+}(\boldsymbol{k}_c)\right|\right), \bar{\rho}_S = \mathrm{Tr}_{orb}\left(\left|\bar{\xi}'_{\Gamma_7^+}(\boldsymbol{k}_c)\right\rangle\left\langle\bar{\xi}'_{\Gamma_7^+}(\boldsymbol{k}_c)\right|\right). \tag{5.5}$$

Algorithm 1 A binary search for $\boldsymbol{k}_c$

function BINARY SEARCH($\boldsymbol{k}_{start}, \boldsymbol{k}_{end}, funcg_S, \epsilon$)
  $\boldsymbol{k}_{mid} = (\boldsymbol{k}_{start} + \boldsymbol{k}_{end})/2$
  $detg_{S_{ks}} \leftarrow funcg_S(\boldsymbol{k}_{start})$
  $detg_{S_{ke}} \leftarrow funcg_S(\boldsymbol{k}_{end})$
  $detg_{S_{km}} \leftarrow funcg_S(\boldsymbol{k}_{mid})$
  if $sgn(detg_{S_{ks}}) = sgn(detg_{S_{km}})$ **then**
    $\boldsymbol{k}^{new}_{start} \leftarrow \boldsymbol{k}_{mid}$
    $\boldsymbol{k}^{new}_{end} \leftarrow \boldsymbol{k}_{end}$
  else if $sgn(detg_{S_{ke}}) = sgn(detg_{S_{km}})$ **then**
    $\boldsymbol{k}^{new}_{end} \leftarrow \boldsymbol{k}_{mid}$
    $\boldsymbol{k}^{new}_{start} \leftarrow \boldsymbol{k}_{start}$
  end if
  if $|detg_{S_{km}}| \leq \epsilon$ **then return** $\boldsymbol{k}_{mid}$
  else BINARY SEARCH($\boldsymbol{k}^{new}_{start}, \boldsymbol{k}^{new}_{end}, funcg_S, \epsilon$)
  end if
end function

The entanglement entropy is simply $S(\rho_S) = -\operatorname{Tr}(\rho_S \log(\rho_S))$. Numerically, we see that $S(\rho_S) = S(\bar{\rho}_S) = 1$.

Note that the change of basis is an important step. In the following, we look at the von Neumann entropy of all the other states around the Bloch-sphere. These states can be written as, $|\theta_B, \phi_B\rangle = \cos(\theta_B)\left|\xi'_{\Gamma_7^+}\right\rangle + e^{i\phi_B}\sin(\theta_B)\left|\bar{\xi}'_{\Gamma_7^+}\right\rangle$ with θ_B and ϕ_B defining the navigation parameters of the orthogonal states $\left|\xi'_{\Gamma_7^+}\right\rangle, \left|\bar{\xi}'_{\Gamma_7^+}\right\rangle$ along the Bloch sphere. Following the same procedure as for the states at the poles, the entropy can be computed for these states as well. We notice $S(|\theta_B, \phi_B\rangle\langle\theta_B, \phi_B|) < 1$. For example, the entanglement entropies of the cardinal states,

$$|\pm\rangle = \left[\frac{1}{\sqrt{2}}\left(\left|\xi'_{\Gamma_7^+}\right\rangle \pm \left|\bar{\xi}'_{\Gamma_7^+}\right\rangle\right)\right], |\pm i\rangle = \left[\frac{1}{\sqrt{2}}\left(\left|\xi'_{\Gamma_7^+}\right\rangle \pm i\left|\bar{\xi}'_{\Gamma_7^+}\right\rangle\right)\right] \tag{5.6}$$

are

$$S(\operatorname{Tr}_{orb}|\pm\rangle\langle\pm|) = 0.810, S(\operatorname{Tr}_{orb}|\pm i\rangle\langle\pm i|) = 0.824, \tag{5.7}$$

which are obviously far from the maximal value.

Recall that Eq.4.50 shows a different way to calculate the spin matrix. This can be done using

the density matrix formalism discussed above. For a density matrix ρ and its Kramers pair $\bar{\rho}$,

$$S_i = \begin{pmatrix} \mathrm{Tr}\left(\rho\sigma_i\right) & \mathrm{Tr}\left(\left|\xi\right\rangle\left\langle\bar{\xi}\right|\sigma_i\right) \\ \mathrm{Tr}\left(\left|\bar{\xi}\right\rangle\left\langle\xi\right|\sigma_i\right) & \mathrm{Tr}\left(\bar{\rho}\sigma_i\right) \end{pmatrix}. \tag{5.8}$$

The off-diagonal terms of this matrix involve terms like $\left|\xi\right\rangle\left\langle\bar{\xi}\right|$ and $\left|\bar{\xi}\right\rangle\left\langle\xi\right|$ which do not correspond to a density matrix. These operators can be obtained from the states, $\left|\xi\right\rangle, \left|\bar{\xi}\right\rangle, \left|+_B\right\rangle = \frac{1}{\sqrt{2}}\left(\left|\xi\right\rangle + \left|\bar{\xi}\right\rangle\right), \left|-_B\right\rangle = \frac{1}{\sqrt{2}}\left(\left|\xi\right\rangle + i\left|\bar{\xi}\right\rangle\right)$ using the quantum process tomography (QPT) method as defined in sec.8.4.2 of [12]. The QPT method can be used to describe the how the input state $\left|\xi\right\rangle\left\langle\bar{\xi}\right|$ can be transformed into the output state which is a linear combination of the density matrix representations, and vice versa. The statevectors $\left|+_B\right\rangle$ and $\left|-_B\right\rangle$ are defined in a non-conventional manner, but here we follow the convention of the authors of [12]. We combine these operators in the following manner,

$$\begin{aligned} \left|+_B\right\rangle\left\langle+_B\right| + i\left|-_B\right\rangle\left\langle-_B\right| - \frac{1+i}{2}\left|\xi\right\rangle\left\langle\xi\right| - \frac{1+i}{2}\left|\bar{\xi}\right\rangle\left\langle\bar{\xi}\right| &= \frac{1}{2}\left|\xi\right\rangle\left\langle\xi\right| + \frac{1}{2}\left|\xi\right\rangle\left\langle\bar{\xi}\right| + \frac{1}{2}\left|\bar{\xi}\right\rangle\left\langle\xi\right| + \frac{1}{2}\left|\bar{\xi}\right\rangle\left\langle\bar{\xi}\right| \\ &+ \frac{i}{2}\left|\xi\right\rangle\left\langle\xi\right| + \frac{1}{2}\left|\xi\right\rangle\left\langle\bar{\xi}\right| - \frac{1}{2}\left|\bar{\xi}\right\rangle\left\langle\xi\right| + \frac{i}{2}\left|\bar{\xi}\right\rangle\left\langle\bar{\xi}\right| \\ &- \frac{1}{2}\left|\xi\right\rangle\left\langle\xi\right| - \frac{i}{2}\left|\xi\right\rangle\left\langle\xi\right| - \frac{1}{2}\left|\bar{\xi}\right\rangle\left\langle\bar{\xi}\right| - \frac{i}{2}\left|\bar{\xi}\right\rangle\left\langle\bar{\xi}\right| \\ &= \left|\xi\right\rangle\left\langle\bar{\xi}\right|. \end{aligned} \tag{5.9}$$

Thus we see that the off-diagonal terms can be re-written using the original density matrices. In the same way, we can use the QPT method to obtain an expression for $\left|\bar{\xi}\right\rangle\left\langle\xi\right|$ as a linear combination the density matrices. In the latter case, we must redefine $\left|-_B\right\rangle = \frac{1}{\sqrt{2}}\left(\left|\xi\right\rangle - i\left|\bar{\xi}\right\rangle\right)$. In this section we have shown the entanglement dynamics for the state $\left|\Gamma_7^+\right\rangle$. The same can be done for all the other states that have been discussed in lemma.1.

5.5 Topology of $det(\boldsymbol{g}) = 0$ surfaces

So far we have shown that the points $\boldsymbol{k}_c$ in the momentum-space, at which $det\left(\boldsymbol{g}\right) = 0$ exist all around the Γ-point, creating one or multiple surfaces around it. This is guaranteed by symmetry. We have shown a method to obtain these points and a method to also quantify the entanglement of the spin-states at these points. In the rest of the chapter, we will focus on the topology of the surfaces formed out of these points.

The surfaces in $\boldsymbol{k}$-space determined by the equation $det(\boldsymbol{g}(\boldsymbol{k})) = 0$, which may be calculated using the method described in Sec. 5.4.2, can have complex topology. In the following, we show some of these surfaces for the first conduction and split-off (valence) bands for Si, the second conduction and split-off bands for Ge and the split-off bands of GaAs. These are the bands belonging to the interesting representations as discussed in lemma 1. The calculations for GaAs have been

done using an sp^3-band model [13, 14], which has been fitted to match valence-band properties. We also observe a multiplicity of these surfaces for both Si and Ge in various directions.

5.5.1 Maximal Entanglement Surfaces

Silicon: first conduction band

We start by looking at the surface of silicon first conduction band. As we know this is the band of interest for most of electronics. Fig.5.4 shows the surface that encloses $det\,(g_S) < 0$. Recall from the result of theorem.2 that this is also the surface at which the spin and orbital subspaces are maximally entanglement.

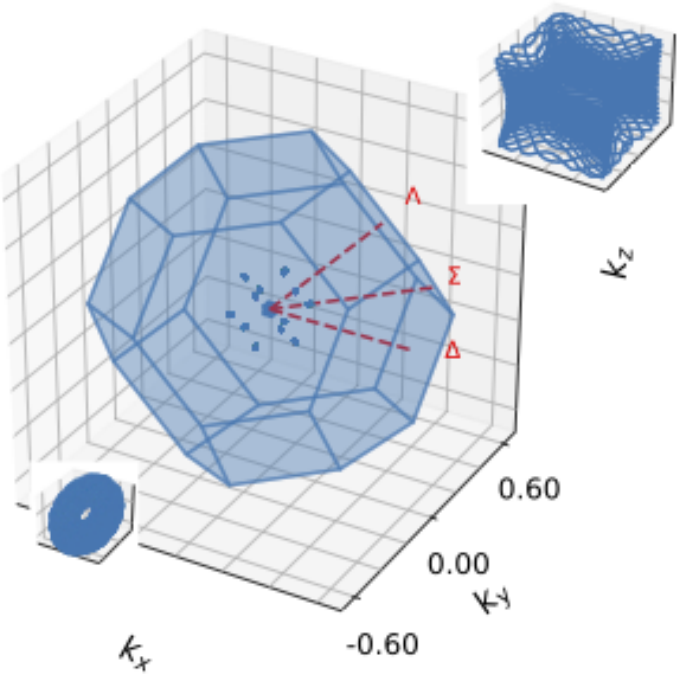

Figure 5.4: MES of silicon for the first conduction bands, with Brillouin zone boundary shown. The inset in the top right corner shows the innermost surface; grid spacing here is $10^{-2}\,a_o^{-1}$. This surface closely resembles a cuboid, and it is surrounded by flattened toruses in the $\mathbf{\Sigma}$ (110) directions. The inset in the bottom left corner is a zoom of this structure, with grid spacing here being $10^{-3}\,a_o^{-1}$.

In the main part of Fig.5.4, the blue region indicates the entire Brillouin zone. As can be seen this region extends in $[-0.6, 0.6]$ interval in the k_x, k_y, k_z directions. The scale is in atomic units. At the center of the Brillouin zone, is a smooth cuboid with concave faces whose magnified version is shown in the upper inset. This is the main surface at which $det(g_S) = 0$ and we note that it is topologically spherical. We call this surface a maximal entanglement surface (MES). As mentioned earlier, we do not concern ourselves too much with the accuracy of the locations of these points, but you may notice that this surface is very close to the Γ-point, extending to rather small

fraction of the distance to the Brillouin zone boundaries.

Fig.5.4 also shows twelve smaller toruses, all of which lie along the $\Sigma(110)$-direction.[1]The bottom inset shows a zoomed in version of these toruses. They are mostly flat. These toruses are examples of the aforementioned "multiple surfaces". They occur because the bands with a different degeneracy (corresponding to the black representations in table.4.1) have anti-crossings with the Kramers bands represented by the red labels of table.4.1 in the Σ-direction.

Germanium: second conduction band

The germanium MES surface is different than the "simpler" silicon one. The band that has the symmetry as mentioned in lemma.1 is in fact the second conduction bands. We show, in Fig.5.5, the zoomed-in version of the splitting of this band Fig.5.1,

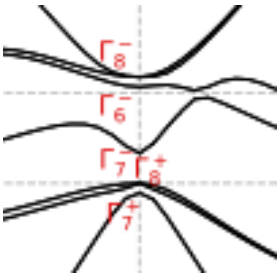

Figure 5.5: Splitting of bands Γ_6^- and Γ_7^+. The band with the symmetry of lemma.1 are these two bands which can be seen here to be *isolated* in the sense of definition.1 from chapter.4.

The first thing to notice in Fig.5.6 is that the cuboid-like object (the MES of Ge) in the center of the blue region of the Brillouin zone is very similar to the one in Fig.5.4. The difference is that, this cuboid has now holes in its eight vertices ($\Lambda(111)$-direction) which lead to tube-like structures extending all the way to the next BZ. We see that the topology of this surface is similar to the Fermi surface of copper, except that the tubes that connect to the second BZ are longer and narrower. In Fig.5.6 the thickness of the tubes has been exaggerated by a factor of 2 because of the size of the point plotting. The reason for the occurrence of these tube-like structures is also the same, the adjacent bands approach the Kramers bands in these directions.

Split-off bands

The conduction bands were the important bands for silicon and germanium. But since we promised that these surfaces are guaranteed for other set of bands as well, we will now discuss the topology of the split-off bands for all three semi-conductors, silicon, germanium and gallium-arsenide.

[1]The figure.5.4 as one of the torus seems to be on the red line demarcated along the $\Lambda(111)$-direction. but this only because of the prespectve in which the figure is shown.

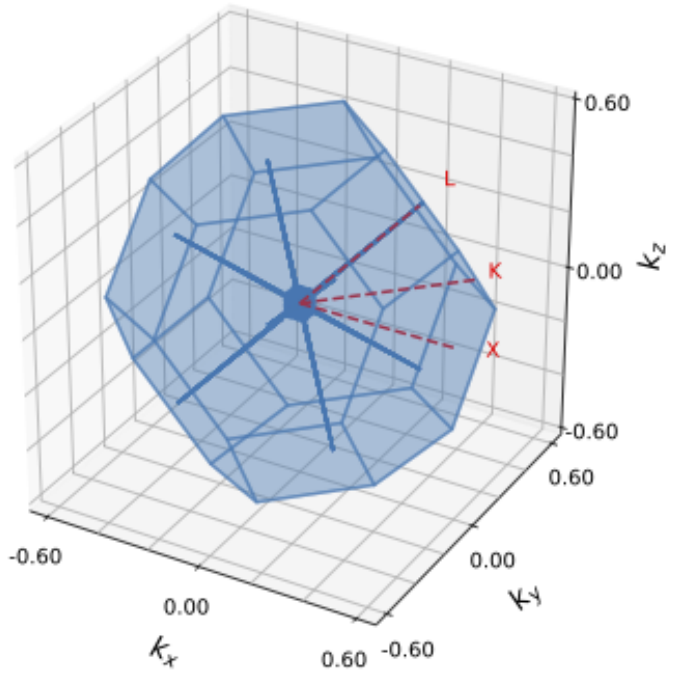

Figure 5.6: The germanium MES for the second conduction bands, with Brillouin zone boundary shown. The surface resembles a cuboid with openings at the vertices. These openings connect to the central surfaces of the neighboring zones via long tube like structures, whose thickness is exaggerated by a factor of 2 for visualization.

Fig.5.7, shows the surfaces on which $det(g_S) = 0$ for the split-off bands of the three semiconductors. As we can see from Fig.5.1, the split-off bands are well-isolated. This is also reflected in Fig.5.7: we do not see multiple surfaces in any of the three cases. All three surfaces are topologically spheres.

For silicon and germanium, Fig.5.7.a) and b), the spin-orbit entanglement on the entire surface is maximal for the split-off bands. For gallium-arsenide, notice that the surface itself is significantly larger than the one for silicon and germanium. This is because the spin-orbit interaction is much larger in this case. As GaAs belong to the Point group T_d, according to lemma.1, there are only 14 points where the spin-orbit entanglement is maximum. These points occur along the Δ and the Λ directions. These are indicated as blue points on Fig.5.7.c).

5.5.2 Zero-crossing surfaces of $det(g_{tot}) = 0$

The surfaces where $det(g_{tot}) = 0$ are significantly different than the ones where $det(g_S) = 0$. Recall that $g_{tot} = g_S + g_L$. The contributions coming from the orbital magnetic moment have drastic effects on the singular values of g_{tot} and subsequently on the surfaces. We have discussed some instances earlier where the Berry curvature contribution can become quite large and even dominate over the spin-contribution.

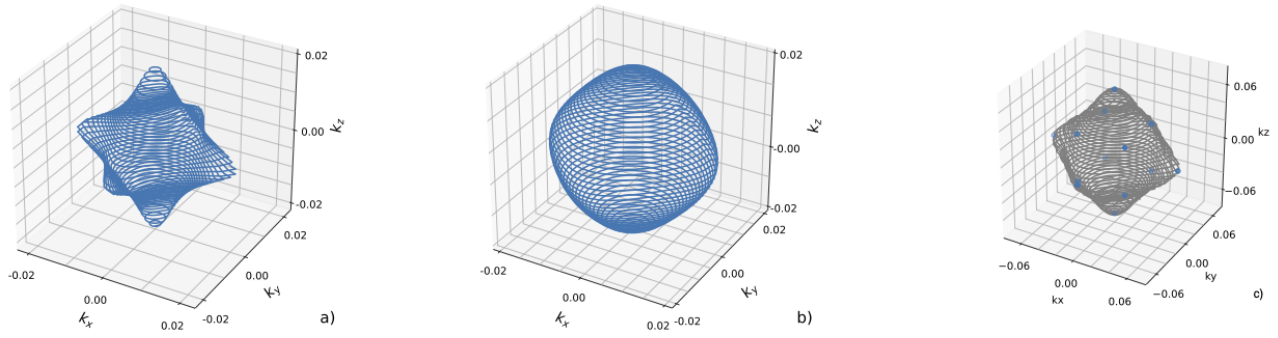

Figure 5.7: MES surfaces of split-off bands (valence bands). (a) The surface of Si. (b) The surface of Ge. These surfaces are topologically spherical. (c) The split-off bands of GaAs exhibit maximum spin-orbit entanglement only along the **Δ** and **Λ** directions. The grey surface is the surface where $det(g_S) = 0$. The spin-orbit entanglement is maximal only at the blue points on this surface.

Split-off bands

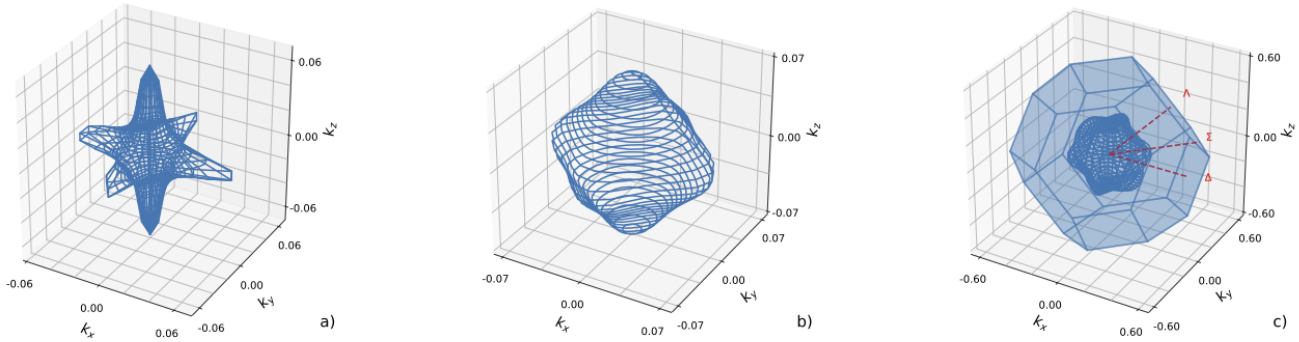

Figure 5.8: Panels (a), (b), (c) show surfaces on which $det(g_{tot}) = 0$ of the split-off bands for Si, Ge and GaAs respectively. Si and Ge surfaces are of comparable scales whereas the GaAs surface almost covers half of the BZ.

For the split-off bands, Fig.5.8, we notice a similarity from the previous case. The bands are isolated and well-behaved. The surfaces turn out to be are topologically spherical. The surface for silicon, Fig.5.8.a), is more pointed in the Δ-direction and does not extend very far out.

The surface of germanium Fig.5.8.b), on the other hand, is a bit more rounded but similar in size to that of silicon, once again, accounting for the comparable magnitude of the spin-orbit interaction in the two cases.

The surface of gallium-arsenide extends out in different directions than silicon or germanium. This surface is also much larger as compared to the other two for the same reason as mentioned in 5.5.1. In general, all of these surfaces are slightly larger than the g_S surfaces because of the extra contributions coming from g_L.

Silicon: first conduction band

The surface of $det(\boldsymbol{g}_{tot}) = 0$ for silicon is more complex then the previous case. Here, we have double surfaces that join together at certain points. Fig. 5.9 shows how far the entire surface extend in the Brillouin Zone which is demarcated by the blue region.

The central surface is made of two concentric cuboids that touch in the Δ and the Λ-directions. This is seen more clearly from the inset. The inset displays a cross-section of the double cube. In the Λ-direction we also see four red satellite regions. In the Σ-directions we see longer satellite regions. This is also again a feature of the adjacent bands and Kramers bands coming close together.

The touching of the central double surfaces is due to symmetry reasons. Remark that this occurs in the two directions along which we expect $\Sigma_{xx}, \Sigma_{yy} = \Sigma_{zz} = 0$ since we know that at least two values must go to 0. These touchings are known as Lifshitz critical points [15]. When approaching high symmetry directions, we say that the surfaces pinch together, giving rise to touching conical structures as in the Fermi surfaces of semi-metals such as graphite [16, 17].

We see that the touchings are a typical feature of $det(\boldsymbol{g}_{tot}) = 0$. At a different value of $det(\boldsymbol{g}_{tot})$, we see what is known as a Lifshitz transition: for $det(\boldsymbol{g}_{tot}) < 0$, the surfaces separate away from the symmetry direction causing the symmetry axes to pass through the gaps now formed between the surfaces. This causes the surface to have a non-trivial topology as it then has thirteen holes: eight along the $\boldsymbol{\Lambda}$-directions and five along the $\boldsymbol{\Delta}$-directions. We count the two holes in the z-direction as a single one, this is analogous to a torus have a single hole. The genus of the surface for $det(\boldsymbol{g}_{tot}) < 0$ is therefore 13. For a more pictorial example, this surface would look like a wiffle ball with 14 holes.

For a slightly positive value of $det(\boldsymbol{g}_{tot})$, the bands separate along the symmetry directions, causing gaps open longitudinally. That leaves two separate cubes, one inside the other. This causes the surface to have an overall genus 0 for $det(\boldsymbol{g}_{tot}) > 0$. We do not discuss the satellite surfaces here as they only shrink or appear enlarged in size as we consider slightly positive or negatives values of the determinant, their topology does not change.

Germanium: second conduction band

The surface of germanium for $det(\boldsymbol{g}_{tot}) = 0$ is even more complex than that of silicon. Fig. 5.10 shows a cross section of the figure in the diagonal plane across the BZ. As can be seen, the central part of the surface is topologically spherical. The second surface has a rugged form and has openings in the six $\boldsymbol{\Delta}$-directions. The dashed lines are additional surfaces connecting into the next BZ. The points where the dashed lines connect to the second surface are not special points.

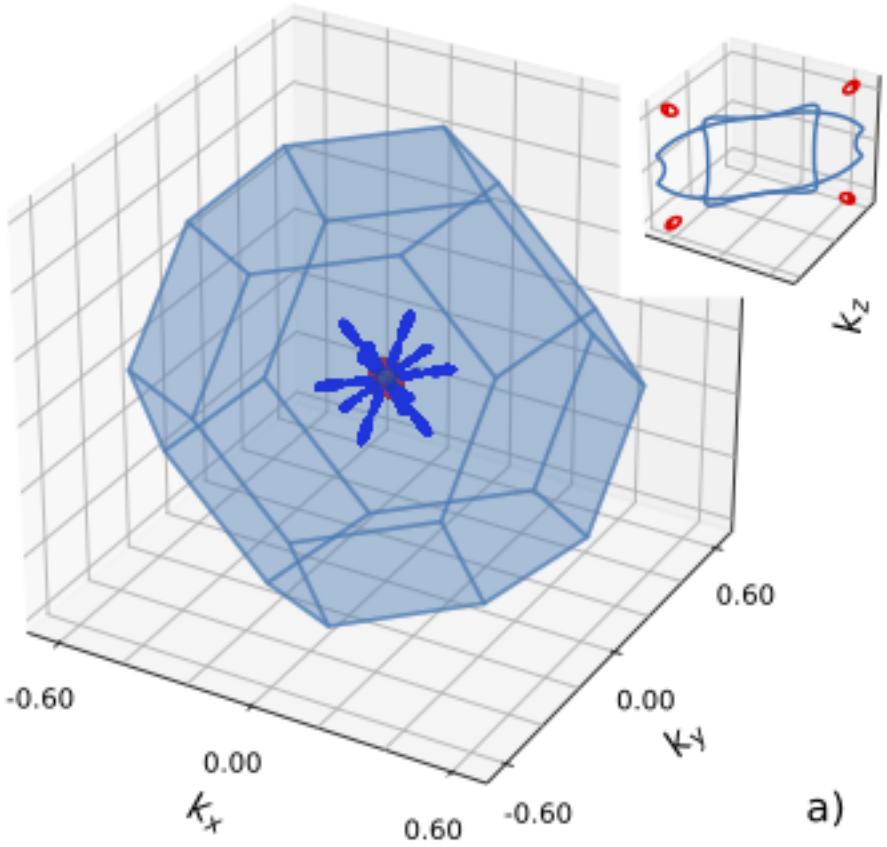

Figure 5.9: Visualization of the surfaces defined by $det(g_{tot}) = 0$ for the first conduction band of Si. The central part is a double surface. The inset shows the cross-section of this central region and four spherical satellites in the **Λ**-directions. One can clearly note the conical touchings in the **Δ** and **Λ** symmetry directions. The Lifshitz transition at $det(g_{tot}) = 0$ involves a change of genus of this surface from 0 to 13. Additional surfaces are present as elongated satellites in the **Σ** and **Δ** directions.

The part which we refer to as the second surface appears as two separate pieces on either side of the central surface in the cross-section. But in the full 3D picture, these two pieces are connected all around the central sphere and have holes along the x, the y and the z-axes. Overall the surface has a genus 5.

Notice that, as in the case of silicon, germanium too admits conical touchings along the **Λ**-direction. Four of these can be seen in the cross-section of Fig.5.10, on either side of the central surface. Contrary to the case of Si, the gaps open away from the symmetry axes when $\det(g_{tot}) < 0$ i.e the axes pass through the gap. Now the surface has eight more holes in the **Λ**-directions along with the five holes that it already had in the **Δ**-directions. The genus of the total surface has changed to 13.

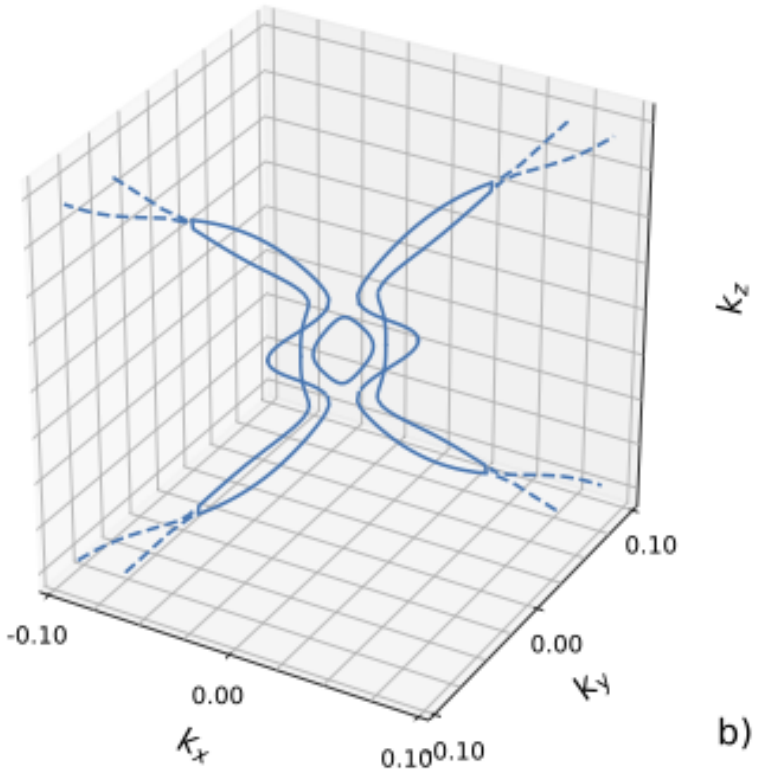

Figure 5.10: Cross section of the $det(g_{tot}) = 0$ Ge surface for the second conduction band. This cross section is informative because it shows four conical touching points (close to the central spherical surface) along the $\mathbf{\Lambda}$ directions. In this case as well, the Lifshitz transition changes the genus of the surface from 5 to 13.

The gaps open along the symmetry directions for a slightly positive value of the determinant, $det(g_{tot}) > 0$. This only makes the second surface a double sphere with five holes, or more pictorially, a double layered wiffle ball with five holes. The transition of the determinant from a positive to a negative value changes its genus from 13 to 5, thus changing the topology of the surface.

The appearance of gaps in the conical structures with the change of the surface genus is perhaps indicative of a quantum phase transition. The next step is to apply this theory to spin qubits in Si/SiGe hetero-structures. The momentum matrix element approach is designed to be accurate in the atomic limit. For systems with more complex behavior and where other external factors have a significant influence through the orbital contribution, we may need to consider a different approach which is discussed in the succeeding chapters.

Bibliography

[1] Laura M. Roth and Benjamin Lax. g factor of electrons in germanium. *Phys. Rev. Lett.*, 3: 217–219, Sep 1959. doi: 10.1103/PhysRevLett.3.217. URL https://link.aps.org/doi/10.1103/PhysRevLett.3.217.

[2] Laura M. Roth. g factor and donor spin-lattice relaxation for electrons in germanium and silicon. *Phys. Rev.*, 118:1534–1540, Jun 1960. doi: 10.1103/PhysRev.118.1534. URL https://link.aps.org/doi/10.1103/PhysRev.118.1534.

[3] L. Liu. Valence spin-orbit splitting and conduction g tensor in si. *Phys. Rev. Lett.*, 6:683–685, Jun 1961. doi: 10.1103/PhysRevLett.6.683. URL https://link.aps.org/doi/10.1103/PhysRevLett.6.683.

[4] A. Shtyk and C. Chamon. Topological electronic properties of silicon. *Phys. Rev. B*, 102: 195125, Nov 2020. doi: 10.1103/PhysRevB.102.195125. URL https://link.aps.org/doi/10.1103/PhysRevB.102.195125.

[5] Murat Onen and Marco Turchetti. Calculating the band structure of 3c-sic using sp 3 d 5 s* model. *Journal of Theoretical and Applied Physics*, 13:1–6, 2019. doi: 10.1007/s40094-019-0324-5.

[6] Gerhard Klimeck, Dan Blanks, Roger Lake, Chris R. Bowen, Chenjing L. Fernando, Manhua Leng, William R. Frensley, Dejan Jovanovic, and Paul Sotirelis. Writing research software in a large group for the nemo project. *VLSI Design*, 8:035374, 1998. doi: 10.1155/1998/35374. URL https://doi.org/10.1155/1998/35374.

[7] Gerhard Klimeck. Nemo 3d, 1998-2003. URL https://nanohub.org/groups/nemo_3d_distribution.

[8] D. J. Chadi. Spin-orbit splitting in crystalline and compositionally disordered semiconductors. *Phys. Rev. B*, 16:790–796, Jul 1977. doi: 10.1103/PhysRevB.16.790. URL https://link.aps.org/doi/10.1103/PhysRevB.16.790.

[9] Y. M. Niquet, D. Rideau, C. Tavernier, H. Jaouen, and X. Blase. Onsite matrix elements of the tight-binding hamiltonian of a strained crystal: Application to silicon, germanium, and their alloys. *Phys. Rev. B*, 79:245201, Jun 2009. doi: 10.1103/PhysRevB.79.245201. URL https://link.aps.org/doi/10.1103/PhysRevB.79.245201.

[10] Thomas Garm Pedersen, Kjeld Pedersen, and Thomas Brun Kriestensen. Optical matrix elements in tight-binding calculations. *Phys. Rev. B*, 63:201101, May 2001. doi: 10.1103/PhysRevB.63.201101. URL https://link.aps.org/doi/10.1103/PhysRevB.63.201101.

[11] Yia-Chung Chang and D. E. Aspnes. Theory of dielectric-function anisotropies of (001) gaas (2×1) surfaces. *Phys. Rev. B*, 41:12002–12012, Jun 1990. doi: 10.1103/PhysRevB.41.12002. URL https://link.aps.org/doi/10.1103/PhysRevB.41.12002.

[12] Michael A Nielsen and Isaac Chuang. *Quantum computation and quantum information*. American Association of Physics Teachers, 2002.

[13] D. J. Chadi and Marvin L. Cohen. Tight-binding calculations of the valence bands of diamond and zincblende crystals. *Physica Status Solidi B-basic Solid State Physics*, 68:405–419, 1975. URL https://api.semanticscholar.org/CorpusID:12495144.

[14] Mahdisadjadi. Tight-binding calculation of the band structure of silicon, 2016. URL https://gist.github.com/Mahdisadjadi/62c960d3ccad1ee1868e9370e7567229?short_path=55e79d7.

[15] Grigory Volovik. Topological lifshitz transitions. *Low Temp. Phys.*, 43:47–55, January 2017. doi: 10.1063/1.4974185. URL https://doi.org/10.1063/1.4974185.

[16] Mildred S. Dresselhaus and John G. Mavroides. The fermi surface of graphite. *IBM J. Res. Dev.*, 8:262–267, 1964. URL https://api.semanticscholar.org/CorpusID:8497170.

[17] S. M. Young, S. Zaheer, J. C. Y. Teo, C. L. Kane, E. J. Mele, and A. M. Rappe. Dirac semimetal in three dimensions. *Phys. Rev. Lett.*, 108:140405, Apr 2012. doi: 10.1103/PhysRevLett.108.140405. URL https://link.aps.org/doi/10.1103/PhysRevLett.108.140405.

6

Current Density Formalism

6.1 Introduction

In this chapter, we study the orbital contributions to the g-factors of electrons in more complex systems such as quantum dots. Since the potential presumably varies over large lattice distances, we assume that it varies locally in a negligible manner. This means that quantum dot wavefunction is made up of a part which almost does not change over small distance. Approximating the wavefunction in this way is commonly known as the *envelope-function approximation*[1]. The eigenfunctions of the quantum dot electrons are a superposition of the product of the envelope-function at a given lattice point and the corresponding valley states.

Recall that for silicon, the valley states are the six Bloch states at the band minimum which lie in the six Δ-directions. This means that the spin $\boldsymbol{g}$-tensor, $\boldsymbol{g}_S$, can be calculated based on Eq.4.20 and Eq.4.21 with the appropriate choice of ξ and $\bar{\xi}$ as quantum dot eigenstates. We mentioned that the momentum matrix elements are enhanced by the intra-atomic term which acts as second-order correction in the overlap, $\boldsymbol{S}$[2]. This violates gauge invariance. In this chapter we discuss a formalism in which a local and stronger form of conservation holds. This is the current density formalism. The current density relates directly to the magnetic moment, $\boldsymbol{L} = \int \boldsymbol{r} \times \boldsymbol{J}(\boldsymbol{r}) d\boldsymbol{r}$. With this formalism we are able to visualize the origins of the magnetic moment contribution to the g-factor.

6.2 The current density

In this formalism we look at the current density operator which is related to the momentum operator as [1][3],

$$\hat{\boldsymbol{J}}\left(\boldsymbol{R}'\right) = \frac{1}{2m}\left(\hat{\boldsymbol{p}}\delta(\boldsymbol{R}' - \hat{\boldsymbol{R}}) + \delta(\boldsymbol{R}' - \hat{\boldsymbol{R}})\hat{\boldsymbol{p}}\right). \tag{6.1}$$

The expectation value of the current density operator holds the information about the orbital contributions to the g-factor. Consider now a system described by a Hamiltonian H and eigenvectors ψ. The Schrödinger equation of ψ in the discrete basis is,

$$\begin{aligned} i\hbar\frac{d}{dt}\psi_i &= \sum_j H_{ij}\psi_j, \\ -i\hbar\frac{d}{dt}\psi_i^* &= \sum_j H_{ij}^*\psi_j^*. \end{aligned} \tag{6.2}$$

Consider the probability density of the state, $\sum_{i\in s}|\psi|^2$ where s is the spin-orbital index. We look at its time evolution,

$$\begin{aligned} \frac{d}{dt}\sum_{i\in s}|\psi|^2 = \frac{d}{dt}\sum_{i\in s}\psi_i^*\psi_i &= \sum_{i\in s}\left[\left(\frac{d}{dt}\psi_i\right)\psi_i^* + \psi_i\left(\frac{d}{dt}\psi_i^*\right)\right] \\ &= \frac{1}{i\hbar}\sum_{i\in s}\left(\psi_i^*\sum_j H_{ij}\psi_j - \psi_i\sum_j H_{ij}^*\psi_j^*\right). \end{aligned} \tag{6.3}$$

This is an important conservation law also known as the *continuity equation*. Physically this means that our system may admit flow of currents but locally these must cancel each other out.

6.3 Current operator and symmetry

In the case of bulk semiconductors, specifically the ones with high symmetries, the currents preserve these symmetries. In the case of diamond structure crystals, the current densities of the time-reversal pairs and the inversion pairs hold specific relations. These relations can be used later on to draw further conclusions.

In real space, at a position $\boldsymbol{r}$, we write the spin-mixed eigenvectors as a linear combinations of the pure spin-up and spin-down states, $|\psi(r)\rangle = \phi_\uparrow|\uparrow\rangle + \phi_\downarrow|\downarrow\rangle$. Then the current operator for $|\psi(\boldsymbol{r})\rangle$ must be,

$$\left\langle J_\psi(\boldsymbol{r})\right\rangle = -\frac{\hbar}{m}\,\mathrm{Im}\left(\phi_\uparrow^*(\boldsymbol{r})\nabla\phi_\uparrow(\boldsymbol{r}) + \phi_\downarrow^*(\boldsymbol{r})\nabla\phi_\downarrow(\boldsymbol{r})\right). \tag{6.4}$$

[1]Here we show the operators using the $\hat{}$ symbol to distinguish between the position operator $\hat{\boldsymbol{R}}$ and the position vector $\boldsymbol{R}'$ but we will drop the $\hat{}$ notation later on.

When we apply the time reversal operation to the eigenvector,

$$\begin{aligned} T\left|\psi(\boldsymbol{r})\right\rangle &= \phi_{\uparrow}^{*}(\boldsymbol{r})\left|\downarrow\right\rangle - \phi_{\downarrow}^{*}(\boldsymbol{r})\left|\uparrow\right\rangle \\ \implies \left\langle J_{T\psi}(\boldsymbol{r})\right\rangle &= -\frac{\hbar}{m}\,\mathrm{Im}\left(\phi_{\uparrow}(\boldsymbol{r})\nabla\phi_{\uparrow}^{*}(\boldsymbol{r}) + \phi_{\downarrow}(\boldsymbol{r})\nabla\phi_{\downarrow}^{*}(\boldsymbol{r})\right) \\ &= -\frac{\hbar}{m}\,\mathrm{Im}\left(\phi_{\uparrow}^{*}(\boldsymbol{r})\nabla\phi_{\uparrow}(\boldsymbol{r}) + \phi_{\downarrow}^{*}(\boldsymbol{r})\nabla\phi_{\downarrow}(\boldsymbol{r})\right)^{*} \\ &= +\frac{\hbar}{m}\,\mathrm{Im}\left(\phi_{\uparrow}^{*}(\boldsymbol{r})\nabla\phi_{\uparrow}(\boldsymbol{r}) + \phi_{\downarrow}^{*}(\boldsymbol{r})\nabla\phi_{\downarrow}(\boldsymbol{r})\right) = -\left\langle J_{\psi}(\boldsymbol{r})\right\rangle . \end{aligned} \tag{6.5}$$

Applying the inversion operator, we get $P\left|\psi(\boldsymbol{r})\right\rangle = \left|\psi(-\boldsymbol{r})\right\rangle$. The gradient at $-\boldsymbol{r}$ results in an overall negative sign, $\frac{d}{dx}\phi(-x) = -\frac{d}{d(-x)}\phi(-x) = -\frac{d}{dy}\phi(y)|_{y=-x}$.

$$\left\langle J_{P\psi}(\boldsymbol{r})\right\rangle = -\frac{\hbar}{m}\,\mathrm{Im}\left(\phi_{\uparrow}^{*}(-\boldsymbol{r})\nabla\phi_{\uparrow}(-\boldsymbol{r}) + \phi_{\downarrow}^{*}(-\boldsymbol{r})\nabla\phi_{\downarrow}(-\boldsymbol{r})\right) = -\left\langle J_{\psi}(-\boldsymbol{r})\right\rangle . \tag{6.6}$$

We can now write the overall relation between the current densities of partners that are related by time-reversal and by inversion,

$$\left\langle J_{PT\psi}(\boldsymbol{r})\right\rangle = -\left\langle J_{P\psi}(\boldsymbol{r})\right\rangle = \left\langle J_{\psi}(-\boldsymbol{r})\right\rangle . \tag{6.7}$$

6.4 Current density in silicon

6.4.1 Current density in bulk silicon

The current density operator upto this point has been defined as a function of a position $\boldsymbol{r}$ (refer to Eq.6.4). In the case of bulk silicon, we define the current to flow between an atom and its neighbors. In a discretized model such as the tight-binding formalism, we consider only nearest neighbor interactions to be non-zero. As a result, the operator is defined between an atom and its nearest neighbor and depends on the positions of these two atoms placed at two different lattice sites [4, 5]. We call the line connecting an atom and its nearest neighbor as a bond. Fig.6.1 indicates the four bonds of a silicon atom and its four nearest neighbors in red. The eigenfunctions of the atom at position $\boldsymbol{R}_i$ and of its neighbor at $\boldsymbol{R}_j$ are,

$$\begin{aligned} \left|\psi_k(\boldsymbol{R}_i)\right\rangle &= e^{i\boldsymbol{k}\cdot\boldsymbol{R}_i}\left|u_k(\boldsymbol{R}_i)\right\rangle , \\ \left|\psi_k(\boldsymbol{R}_j)\right\rangle &= e^{i\boldsymbol{k}\cdot\boldsymbol{R}_j}\left|u_k(\boldsymbol{R}_j)\right\rangle . \end{aligned} \tag{6.8}$$

The current flow between these states would be[2],

$$\left\langle \boldsymbol{J}(\boldsymbol{R}_i,\boldsymbol{R}_j)\right\rangle = \frac{1}{i\hbar}\left\langle\psi_k\right|\boldsymbol{J}\left|\psi_k\right\rangle . \tag{6.9}$$

[2] $\boldsymbol{J}$ can be defined as a vectorial quantity since it is along the direction of the unit vector between the point $\boldsymbol{R}_i$ and $\boldsymbol{R}_j$

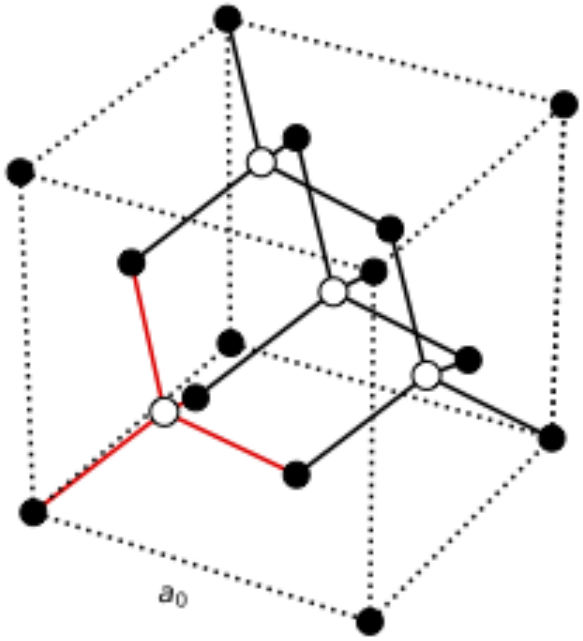

Figure 6.1: The current flow is described to occur along the red bonds between the central "white" atom and its four immediate "black" neighbors.

Here $\boldsymbol{J}\left(\boldsymbol{R}_i, \boldsymbol{R}_j\right)$ describes an off-diagonal matrix similar to the sub-Hamiltonian of the entire crystal Hamiltonian involving the interaction terms between atoms at only positions $\boldsymbol{R}_i$ and $\boldsymbol{R}_j$ whose upper half is multiplied by i and the lower half by $-i$. The entire crystal Hamiltonian, for a million atoms, is approximately a million times million matrix and for convenience, can be divided into smaller blocks of matrices which contain the non-zero interactions for the purpose of studying the expectation values of the local operators.

The band minimum of silicon is a region of interest for many practical purposes in the usual semiconductors. We analyse the current at this point. Consider the wavepacket moving with a group velocity v_g. In R-space, the charge density is the square of the amplitude of the wavepacket (blue curve in Fig.6.2). This charge density admits a finite current density which is proportional to the group velocity [6].

The wavevector $\boldsymbol{k} = (k_x, 0, 0)$ such that at k_x, $\nabla_{\boldsymbol{k}} E = 0$ is a special point. Recall that at this point $\nabla_{\boldsymbol{k}} E = v(\boldsymbol{k}) = 0$. The current vanishes where the charge density is zero or where the group

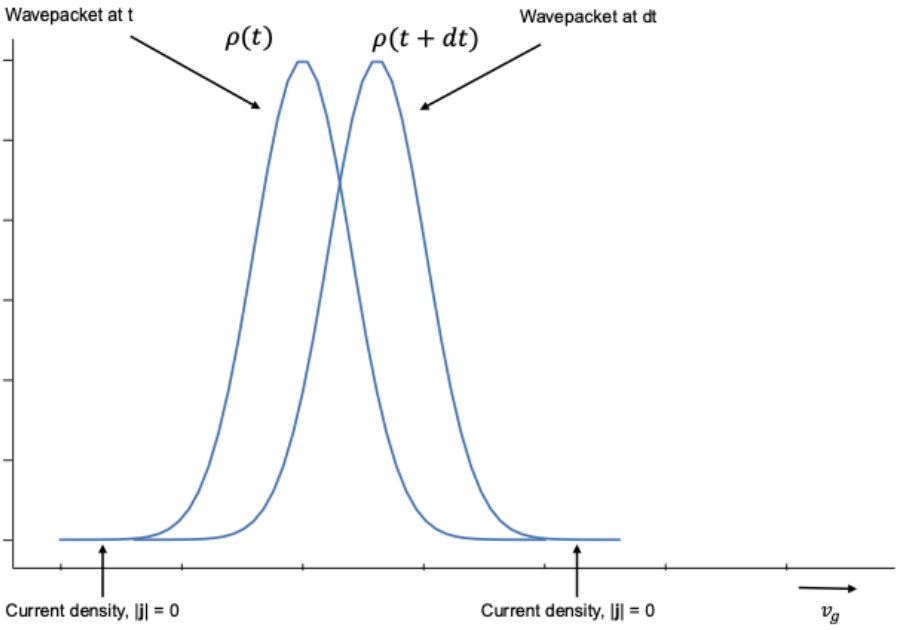

Figure 6.2: As the wavepacket moves in R-space, it has a finite current density overall. At the band-minimum, $v_g = 0$ and so $\langle \boldsymbol{J} \rangle = 0$. The charge density drops at the tails of the curve in the figure and so does the current density.

velocity is zero. At the band minimum, the wavepacket has no group velocity, implying that the expectation value of the current density must be zero for all bonds. In other words, while there may be current flow along the bond between positions $\boldsymbol{R}_i$ and $\boldsymbol{R}_j$, the net current remains zero. This is consistent with the fact that in bulk silicon the g-factor of the Bloch-states at the band minimum within the Chadi-Cohen tight-binding formalism [7] is almost +2 (not exactly +2 because of spin-orbit effects) which comes from only the spin-contribution. There is not orbital contributions for the Bloch states.

Fig.6.3 shows the variation of the current density in the $\left\{ \left|\psi_k(\boldsymbol{R}_i)\right\rangle, \left|\psi_k(\boldsymbol{R}_j)\right\rangle \right\}$ and $\left\{ PT\left|\psi_k(\boldsymbol{R}_i)\right\rangle, PT\left|\psi_k(\boldsymbol{R}_j)\right\rangle \right\}$ Bloch basis of the lowest conduction band Γ_6^- between the orbitals at an arbitrary $\boldsymbol{R}_i$ and the orbitals of one neighbor at $\boldsymbol{R}_j$ along the Δ-direction (i.e. from the Γ to X point). Both the currents (orange curve for $\left\langle J(\boldsymbol{R}_i, \boldsymbol{R}_j)\right\rangle$ and blue curve for $\left\langle (PT)^\dagger J(\boldsymbol{R}_i, \boldsymbol{R}_j) PT\right\rangle$) are 0 at $\boldsymbol{k} = (0,0,0)$ since the group velocity here is also zero. The curves have the same magnitude but are opposite in signs for all k_z. Additionally, the current densities also approach zero at the band minimum, which is located near $k_z = 0.5$ (in atomic units), approximately 85% of the Brillouin zone (BZ).

There is another zero crossing of the currents close to the Γ-point as can be seen in Fig.6.3. It is evident that the currents represented by the orange and blue curves do not increase immedi-

ately in a linear fashion as $\boldsymbol{k}$ increases. The the orange curve is initially negative slightly away from the Γ-point before turning positive, while the blue curve exhibits the opposite behavior. The close proximity of the Γ_6^- and Γ_8^- bands causes interactions that alter their dispersion, deviating from expected behavior. This interaction is a result of a band extremum which is also the reason why the velocity and, consequently, the current densities change sign.

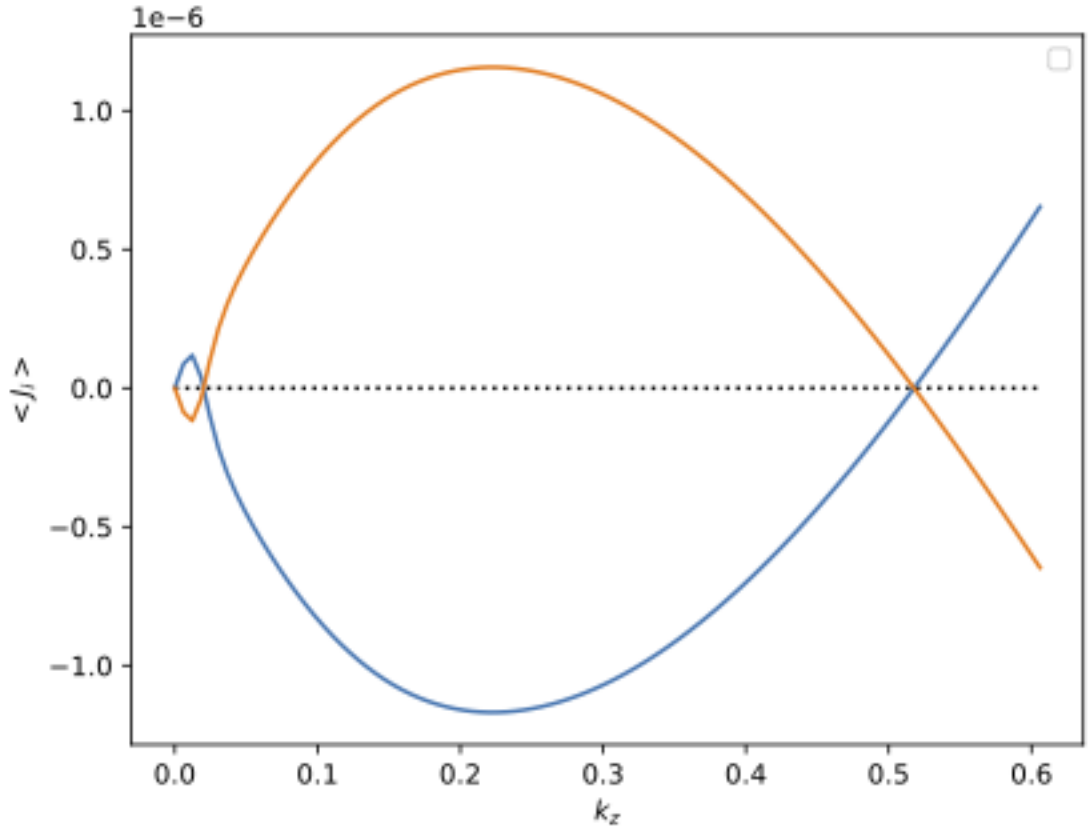

Figure 6.3: A plot of $\langle J(\boldsymbol{R}_0, \boldsymbol{R}_1)\rangle$ and $\langle (PT)^\dagger J(\boldsymbol{R}_0, \boldsymbol{R}_1) PT\rangle$ between the atom at $\boldsymbol{R}_0$ and its neighbor at $\boldsymbol{R}_1$ vs k_z (Δ-direction). The net current at the band minimum along the $(\boldsymbol{R}_i, \boldsymbol{R}_j)$ bond is zero. The orange currents are negative and the blue currents are positive close to the Γ-point. Upon crossing a band extrema, the currents change sign.

6.4.2 Current density for quantum dot eigenstates

As discussed earlier in chapter.3, the electrons are confined in a potential whose effects are more mesoscopic rather than atomic in nature. Therefore, we use the envelope-approximation to describe these electrons wherein $F(\boldsymbol{R})$ captures the effects of the potential at the spatial level. Consider a large volume of a substrate within which we trap electrons using a potential well. The full wave-function of such an electron can be expressed as a product of the function F that captures the mesoscopic variations and a superposition of the periodic Bloch part of the underlying lattice

(refer to chapter 14 eq.78 in [1]),

$$\Psi_n(\boldsymbol{r}) = \sum_{\boldsymbol{k}} \phi_{n\boldsymbol{k}}(\boldsymbol{r}) \int d\boldsymbol{r'} F_n(\boldsymbol{r'}) e^{-i\boldsymbol{k}\cdot\boldsymbol{r'}} = \sum_{\boldsymbol{k}} u_{n\boldsymbol{k}}(\boldsymbol{r}) e^{i\boldsymbol{k}\cdot\boldsymbol{r}} \int d\boldsymbol{r'} F_n(\boldsymbol{r'}) e^{-i\boldsymbol{k}\cdot\boldsymbol{r'}}. \tag{6.10}$$

The conversion of wavevector sum into integrals involves a volume element [1],

$$\sum_{\boldsymbol{k}} = \frac{\Omega}{(2\pi)^3} \int d\boldsymbol{k} = \frac{N}{V_c^*} \int d\boldsymbol{k}, \tag{6.11}$$

where the direct volume Ω contains N primitive cells, $V_c^* = \frac{(2\pi)^3}{V_c}$ is the volume of the primitive cell in the reciprocal lattice and $V_c = \boldsymbol{a} \cdot \boldsymbol{b} \times \boldsymbol{c}$ is the volume of the primitive cell in the direct lattice.
At a point $\boldsymbol{k}$ away from $\boldsymbol{k}_0$,

$$\Psi_n(\boldsymbol{r}) = \frac{(2\pi)^3 N}{V_c} \int d\boldsymbol{k} \left(u_{n\boldsymbol{k}}(\boldsymbol{r})_{|_{\boldsymbol{k}=\boldsymbol{k_0}}} + (\boldsymbol{k} - \boldsymbol{k}_0) \cdot \nabla_{\boldsymbol{k}} (u_{n\boldsymbol{k}}(\boldsymbol{r}))_{|_{\boldsymbol{k}=\boldsymbol{k}_0}} \right) e^{i\boldsymbol{k}\cdot\boldsymbol{r}} \int d\boldsymbol{r'} F_n(\boldsymbol{r'}) e^{-i(\boldsymbol{k}-\boldsymbol{k}_0)\cdot\boldsymbol{r'}}. \tag{6.12}$$

The first term in Eq.6.12 can be resolved easily,

$$\begin{aligned}
\int d\boldsymbol{k}\, u_{n\boldsymbol{k}_0}(\boldsymbol{r}) e^{i\boldsymbol{k}\cdot\boldsymbol{r}} \int d\boldsymbol{r'} F_n(\boldsymbol{r'}) e^{-i(\boldsymbol{k}-\boldsymbol{k}_0)\cdot\boldsymbol{r'}} &= u_{n\boldsymbol{k}_0}(\boldsymbol{r}) \int d\boldsymbol{r'} F_n(\boldsymbol{r'}) \int d\boldsymbol{k}\, e^{i\boldsymbol{k}\cdot\boldsymbol{r}} e^{-i(\boldsymbol{k}-\boldsymbol{k}_0)\cdot\boldsymbol{r'}} \\
&= u_{n\boldsymbol{k}_0}(\boldsymbol{r}) \int d\boldsymbol{r'} F_n(\boldsymbol{r'}) \underbrace{\int d\boldsymbol{k}\, e^{i\boldsymbol{k}\cdot(\boldsymbol{r}-\boldsymbol{r'})}}_{\frac{1}{\sqrt{2\pi}}\delta(\boldsymbol{r}-\boldsymbol{r'})} e^{i\boldsymbol{k}_0\cdot\boldsymbol{r'}} \\
&= \frac{1}{\sqrt{2\pi}} u_{n\boldsymbol{k}_0}(\boldsymbol{r}) e^{i\boldsymbol{k}_0\cdot\boldsymbol{r}} F_n(\boldsymbol{r}) = \frac{1}{\sqrt{2\pi}} \phi_{n\boldsymbol{k}_0}(\boldsymbol{r}) F_n(\boldsymbol{r}).
\end{aligned}$$

$$\implies \Psi_n(\boldsymbol{r}) = \frac{(2\pi)^3 N}{V_c} \left[\frac{1}{\sqrt{2\pi}} \phi_{n\boldsymbol{k}_0}(\boldsymbol{r}) F_n(\boldsymbol{r}) + \int d\boldsymbol{k}\, \nabla_{\boldsymbol{k}} (u_{n\boldsymbol{k}}(\boldsymbol{r}))_{|_{\boldsymbol{k}=\boldsymbol{k}_0}} e^{i\boldsymbol{k}\cdot\boldsymbol{r}} \cdot (\boldsymbol{k} - \boldsymbol{k}_0) \int d\boldsymbol{r'} F_n(\boldsymbol{r'}) e^{-i(\boldsymbol{k}-\boldsymbol{k}_0)\cdot\boldsymbol{r'}} \right]. \tag{6.13}$$

We notice that the integral in the second term of Eq.6.12 can be resolved using integration by parts,

$$\int d\boldsymbol{r'} F_n(\boldsymbol{r'}) (\boldsymbol{k} - \boldsymbol{k}_0) e^{-i(\boldsymbol{k}-\boldsymbol{k}_0)\cdot\boldsymbol{r'}} = i \Big[\int d\boldsymbol{r'} \nabla_{\boldsymbol{r'}} \Big(F_n(\boldsymbol{r'}) e^{-i(\boldsymbol{k}-\boldsymbol{k}_0)\cdot\boldsymbol{r'}} \Big) - \int d\boldsymbol{r'} \nabla_{\boldsymbol{r'}} \Big(F_n(\boldsymbol{r'}) \Big) e^{-i(\boldsymbol{k}-\boldsymbol{k}_0)\cdot\boldsymbol{r'}} \Big]. \tag{6.14}$$

Inserting Eq.6.14 back into the second part of 6.13,

$$
\begin{aligned}
&\int d\boldsymbol{k}\, \nabla_{\boldsymbol{k}}(u_{n\boldsymbol{k}}(\boldsymbol{r}))_{|_{\boldsymbol{k}=\boldsymbol{k}_0}} e^{i\boldsymbol{k}\cdot\boldsymbol{r}} \cdot (\boldsymbol{k}-\boldsymbol{k}_0) \int d\boldsymbol{r'} F_n(\boldsymbol{r'}) e^{-i(\boldsymbol{k}-\boldsymbol{k}_0)\cdot\boldsymbol{r'}} \\
&= i\Big[\nabla_{\boldsymbol{k}}(u_{n\boldsymbol{k}}(\boldsymbol{r}))_{|_{\boldsymbol{k}=\boldsymbol{k}_0}} \cdot \int d\boldsymbol{k}\, e^{i\boldsymbol{k}\cdot\boldsymbol{r}} \Big\{ \int d\boldsymbol{r'} \nabla_{\boldsymbol{r'}} \Big(F_n(\boldsymbol{r'}) e^{-i(\boldsymbol{k}-\boldsymbol{k}_0)\cdot\boldsymbol{r'}} \Big) - \int d\boldsymbol{r'} \nabla_{\boldsymbol{r'}} \Big(F_n(\boldsymbol{r'}) \Big) e^{-i(\boldsymbol{k}-\boldsymbol{k}_0)\cdot\boldsymbol{r'}} \Big\} \Big] \\
&= i\nabla_{\boldsymbol{k}}(u_{n\boldsymbol{k}}(\boldsymbol{r}))_{|_{\boldsymbol{k}=\boldsymbol{k}_0}} \cdot \Big[\int d\boldsymbol{r'} \nabla_{\boldsymbol{r'}} \Big(F_n(\boldsymbol{r'}) \underbrace{\int d\boldsymbol{k}\, e^{i\boldsymbol{k}\cdot(\boldsymbol{r}-\boldsymbol{r'})}}_{\frac{1}{\sqrt{2\pi}}\delta(r-r')} e^{i\boldsymbol{k}_0\cdot\boldsymbol{r'}} \Big) - \int d\boldsymbol{r'} \nabla_{\boldsymbol{r'}} \Big(F_n(\boldsymbol{r'}) \Big) \underbrace{\int d\boldsymbol{k}\, e^{i\boldsymbol{k}\cdot(\boldsymbol{r}-\boldsymbol{r'})}}_{\frac{1}{\sqrt{2\pi}}\delta(r-r')} e^{i\boldsymbol{k}_0\cdot\boldsymbol{r'}} \\
&= \frac{i}{\sqrt{2\pi}} \underbrace{\int \nabla_{\boldsymbol{r}} \cdot \Big(F_n(r) \nabla_{\boldsymbol{k}}(u_{n\boldsymbol{k}}(\boldsymbol{r}))_{|_{\boldsymbol{k}=\boldsymbol{k}_0}} e^{i\boldsymbol{k}_0\boldsymbol{r}} \Big) d\boldsymbol{r}}_{\oint \left(F_n(r) \nabla_{\boldsymbol{k}}(u_{n\boldsymbol{k}}(\boldsymbol{r}))_{|_{\boldsymbol{k}=\boldsymbol{k}_0}} e^{i\boldsymbol{k}_0\boldsymbol{r}} \right) \cdot d\boldsymbol{s} = 0} - \frac{i}{\sqrt{2\pi}} \Big[\nabla_{\boldsymbol{k}}(u_{n\boldsymbol{k}}(\boldsymbol{r}))_{|_{\boldsymbol{k}=\boldsymbol{k}_0}} e^{i\boldsymbol{k}_0\cdot\boldsymbol{r}} \cdot \nabla_{\boldsymbol{r}} \Big(F_n(\boldsymbol{r}) \Big) \Big] \\
&= -\frac{i}{\sqrt{2\pi}} \nabla_{\boldsymbol{k}}(u_{n\boldsymbol{k}}(\boldsymbol{r}))_{|_{\boldsymbol{k}=\boldsymbol{k}_0}} \cdot \nabla_{\boldsymbol{r}} \Big(F_n(\boldsymbol{r}) \Big) e^{i\boldsymbol{k}_0\cdot\boldsymbol{r}}.
\end{aligned} \tag{6.15}
$$

The boundary term is a volume integral ($\int d\boldsymbol{r}$) over all space. $u_{n\boldsymbol{k}}(\boldsymbol{r})_{|_{\boldsymbol{k}=\boldsymbol{k}_0}} e^{i\boldsymbol{k}_0\cdot\boldsymbol{r}}$ is a constant vector such that $\nabla_{\boldsymbol{r}} \cdot u_{n\boldsymbol{k}}(\boldsymbol{r})_{|_{\boldsymbol{k}=\boldsymbol{k}_0}} e^{i\boldsymbol{k}_0\cdot\boldsymbol{r}}$. We apply Gauss-divergence theorem for volume integral of a gradient field.

$$
\begin{aligned}
\nabla_{\boldsymbol{k}}(u_{n\boldsymbol{k}}(\boldsymbol{r}))_{|_{\boldsymbol{k}=\boldsymbol{k}_0}} \cdot \int d\boldsymbol{r} \nabla_{\boldsymbol{r}} F_n(\boldsymbol{r}) e^{i\boldsymbol{k}_0\cdot\boldsymbol{r}} &= \int \nabla_{\boldsymbol{r}} \cdot \Big(F_n(\boldsymbol{r}) \nabla_{\boldsymbol{k}}(u_{n\boldsymbol{k}}(\boldsymbol{r}))_{|_{\boldsymbol{k}=\boldsymbol{k}_0}} e^{i\boldsymbol{k}_0\cdot\boldsymbol{r}} \Big) d\boldsymbol{r} \\
&\quad - \int F_n(\boldsymbol{r}) \underbrace{\nabla_{\boldsymbol{r}} \cdot \Big(\nabla_{\boldsymbol{k}}(u_{n\boldsymbol{k}}(\boldsymbol{r}))_{|_{\boldsymbol{k}=\boldsymbol{k}_0}} e^{i\boldsymbol{k}_0\cdot\boldsymbol{r}} \Big)}_{=0} d\boldsymbol{r} \\
&= \oint \Big(F_n(\boldsymbol{r}) \nabla_{\boldsymbol{k}}(u_{n\boldsymbol{k}}(\boldsymbol{r}))_{|_{\boldsymbol{k}=\boldsymbol{k}_0}} e^{i\boldsymbol{k}_0\cdot\boldsymbol{r}} \Big) \cdot d\boldsymbol{S} \\
&= \Big(\nabla_{\boldsymbol{k}}(u_{n\boldsymbol{k}}(\boldsymbol{r}))_{|_{\boldsymbol{k}=\boldsymbol{k}_0}} e^{i\boldsymbol{k}_0\cdot\boldsymbol{r}} \Big) \underbrace{\oint F_n(\boldsymbol{r}) \cdot d\boldsymbol{S}}_{=0}.
\end{aligned} \tag{6.16}
$$

At infinity the envelope functions $F_n(\boldsymbol{r})$ fall to zero. And therefore the boundary term is zero.

After resolving the integrals, Eq.6.12 becomes

$$
\Psi_n(\boldsymbol{r}) = \frac{(2\pi)^3 N}{V_c \sqrt{2\pi}} \Big[u_{n\boldsymbol{k}_0}(\boldsymbol{r}) F_n(\boldsymbol{r}) e^{i\boldsymbol{k}_0\cdot\boldsymbol{r}} - i\nabla_{\boldsymbol{k}}(u_{n\boldsymbol{k}}(\boldsymbol{r}))_{|_{\boldsymbol{k}=\boldsymbol{k}_0}} \cdot \nabla_{\boldsymbol{r}} \Big(F_n(\boldsymbol{r}) \Big) e^{i\boldsymbol{k_0}\cdot\boldsymbol{r}} \Big]. \tag{6.17}
$$

Notice that the envelope contribution $F_n(\boldsymbol{r})$ acts as a scaling factor. The expectation value of the current density operator at the band minimum will have no contributions coming from the term that is of zero-order in $\nabla_{\boldsymbol{r}}$ and $\nabla_{\boldsymbol{k}}$. The concept behind this has already been discussed in detail in the section.6.4.1. However, there may be a finite amount of current at the band minimum due to the first order gradients of the wavefunction as can be seen in Eq.6.17. This is also consistent with the Berry curvature effects that we have discussed in the bulk case in chapter.4 section.4.2.2

Eq.4.22.

We can easily extend this analysis to include the valley states and discuss the full quantum dot wavefunction. This shows that the effects of the spatial variations in the quantum dot will lead to the deviation of the g-factor value from +2.

6.5 Graphene

Graphene has become an interesting material in the last two decades to study not only from the perspective of material science and condensed matter theory but also from the perspective of quantum technology. Graphene admits many unusual and interesting properties as will be seen. Because it comprises predominantly of ^{12}C and has a low spin-orbit coupling, it is predicted to have long coherence times and can prove to be another promising candidate for quantum computing.

Bilayer graphene offers improved control over qubits and is more popularly used in quantum computing architectures. Numerous studies have been carried out to determine the effective g-factor in bilayer graphene [8–10]. The valley g-factors have also been measured experimentally [11, 12]. We proceed to look at the physical properties of monolayer graphene using the tight-binding formalism in order to understand the origins of the orbital contributions better.

Graphene is a 2D topological material which means that its energy bands admit Dirac cones [13] due to spin-orbit coupling. To see this, consider a lattice of monolayer graphene where atoms are arranged in a honeycomb pattern as shown in Fig.6.4. Any two atoms connected with a horizontal bond form a unit cell with a length a_0. The nearest neighbor hoppings of strength t_1 are defined between atoms of different types (between white and black atoms as in Fig.6.4) indicated as the red vectors denoted by $\overrightarrow{a_i}$. We introduce the second neighbor hoppings indicated as the black vectors, denoted by $\overrightarrow{b_i}$. These hoppings are defined between atoms of the same type, are purely imaginary in nature and have a chirality as is shown in Fig.6.4.

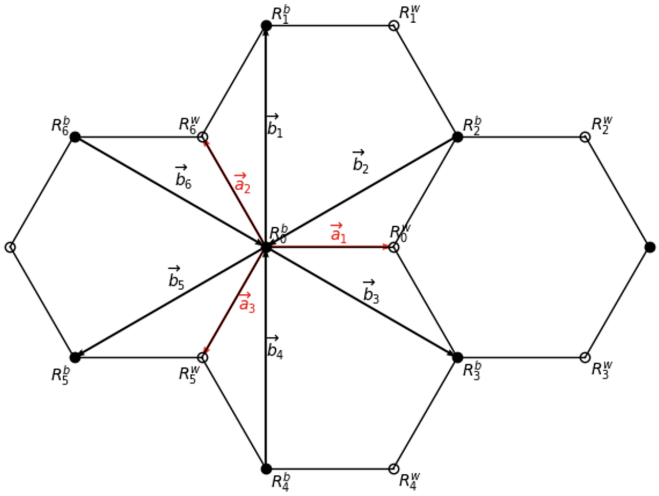

Figure 6.4: A honeycomb lattice of 2D graphene with two atoms forming a unit cell. Here, the atoms shown in white and black sharing a horizontal bond form a unit cell. The two types of bonds are shown in red and black. The nearest-neighbor interactions are the red arrows denoted as the vectors $\overrightarrow{a_i}$ and the second-neighbor interactions are the black dashed arrows denoted by $\overrightarrow{b_i}$. Note the chirality of the second neighbor hoppings.

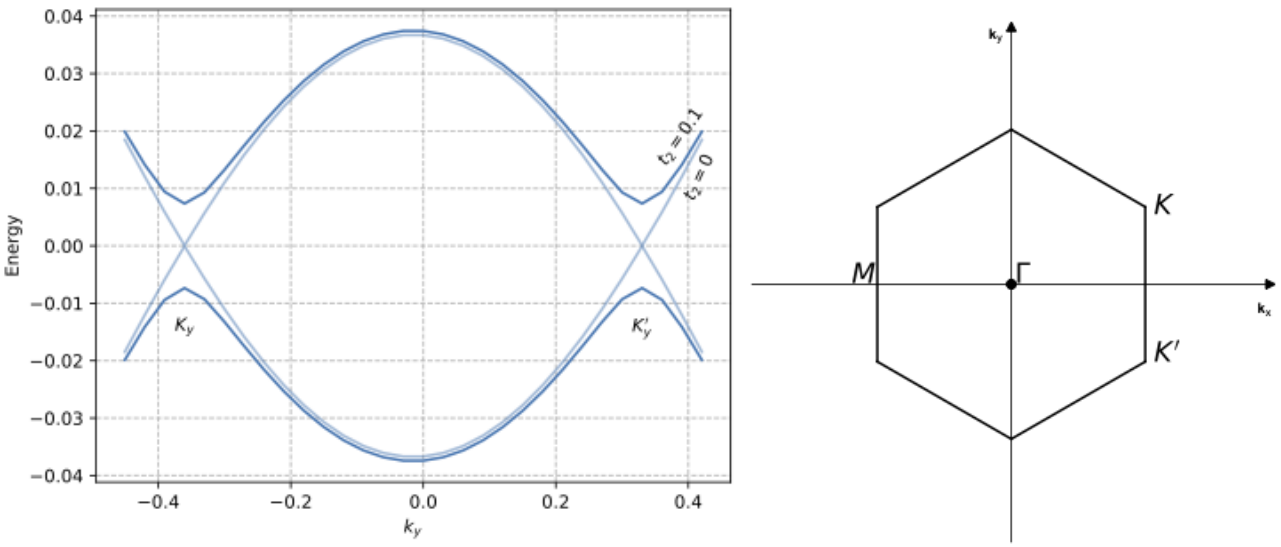

Figure 6.5: The band structure of graphene and its Brillouin zone. The blue curves are the conduction and valence bands of monolayer graphene. For a finite value of t_2 (Eq.6.18), we see gaps at points $\boldsymbol{K}$ and $\boldsymbol{K}'$. The rotated hexagon in $\boldsymbol{k}$-space is the first Brillouin zone of graphene and shows the location of the six valleys states. As t_2 decreases the gaps close at only $\boldsymbol{K}$ and $\boldsymbol{K}'$.

The Hamiltonian describing this system is:

$$H(k) = \left(t_1 \sum_i \cos(\boldsymbol{k}\cdot\boldsymbol{a}_i)\right)\sigma_x + \left(-t_1 \sum_i \sin(\boldsymbol{k}\cdot\boldsymbol{a}_i)\right)\sigma_y + \left(2t_2 \sum_i \sin(\boldsymbol{k}\cdot\boldsymbol{b}_i)\right)\sigma_z. \tag{6.18}$$

Here the action of the Pauli matrices, σ_i is not on spin but on the atomic p_π-orbitals of the black and the white atoms. The Hamiltonian in Eq. 6.18 is defined solely within the spin-up subspace, while in the spin-down subspace, the sign of the σ_z term is reversed. The energies of this Hamiltonian are,

$$E_\pm = \pm\sqrt{3t_1^2 + \sum_{i\neq j}\left(e^{i\boldsymbol{k}\cdot(\boldsymbol{a}_i-\boldsymbol{a}_j)} + e^{-i\boldsymbol{k}\cdot(\boldsymbol{a}_i-\boldsymbol{a}_j)}\right)t_1^2 + 4t_2^2\sum_i \sin\left(\boldsymbol{k}\cdot\boldsymbol{b}_i\right)}. \tag{6.19}$$

At $t_2 \neq 0$, the band structure admits a gap. Furthermore, for $t_2 = 0$, these gaps close only at points $\boldsymbol{K} = \frac{2\pi}{3a_0}\left(1, \frac{1}{\sqrt{3}}\right)$ and $\boldsymbol{K}' = \frac{2\pi}{3a_0}\left(1, -\frac{1}{\sqrt{3}}\right)$. These are the Dirac cones.

6.6 Current density in Graphene

To study the orbital contributions in graphene, we employ the current density formalism. We define current flows between the atoms at different lattice sites, as was the case of silicon. Notice that because we have two types of hoppings, we have two different kinds of currents. First type of currents are the ones that flow between atoms of different types (such as currents between the black and the white atoms in Fig.6.4) along the red bonds. The second types of currents are the ones flowing between the second neighbors (atoms of the same kind such as between the black atoms in Fig.6.4) along the black bonds.

We decompose the Hamiltonian as a product of the Pauli matrices $\boldsymbol{\sigma}$ where $\boldsymbol{\sigma} = \{\sigma_x, \sigma_y, \sigma_z\}$ and a vector $\boldsymbol{v} = (r\sin(\theta)\cos(\phi), r\sin(\theta)\sin(\phi), r\cos(\theta))$, such that $H = \boldsymbol{v}\cdot\boldsymbol{\sigma}$ and

$$\begin{aligned}
r\sin(\theta)\cos(\phi) &= t_1\left(\cos(\boldsymbol{k}\cdot\boldsymbol{a}_1) + \cos(\boldsymbol{k}\cdot\boldsymbol{a}_2) + \cos(\boldsymbol{k}\cdot\boldsymbol{a}_3)\right) = x,\\
r\sin(\theta)\sin(\phi) &= -t_1\left(\sin(\boldsymbol{k}\cdot\boldsymbol{a}_1) + \sin(\boldsymbol{k}\cdot\boldsymbol{a}_2) + \sin(\boldsymbol{k}\cdot\boldsymbol{a}_3)\right) = y,\\
r\cos(\theta) &= t_2\left(\sin(\boldsymbol{k}\cdot\boldsymbol{b}_1) + \sin(\boldsymbol{k}\cdot\boldsymbol{b}_2) + \sin(\boldsymbol{k}\cdot\boldsymbol{b}_3)\right) = z.
\end{aligned} \tag{6.20}$$

$$\begin{aligned}
&\implies r = \sqrt{x^2+y^2+z^2},\\
&\implies \cos(\theta) = \frac{z}{r},\\
&\implies \cos(\phi) = \frac{x}{\sqrt{x^2+y^2}}, \sin(\phi) = \frac{y}{\sqrt{x^2+y^2}}.
\end{aligned} \tag{6.21}$$

Then we can easily define its eigenstates as Bloch vectors which lie along $\boldsymbol{v}$,

$$\begin{aligned}
|u_{\boldsymbol{k}}(\boldsymbol{R})\rangle &= \cos\left(\frac{\theta}{2}\right)|B_i\rangle + e^{i\phi}\sin\left(\frac{\theta}{2}\right)|W_j\rangle\\
&= \sqrt{\frac{1+\frac{z}{r}}{2}}\,|B_i\rangle + e^{i\phi}\sqrt{\frac{1-\frac{z}{r}}{2}}\,|W_j\rangle\,.
\end{aligned} \tag{6.22}$$

where $|B_i\rangle$ and $|W_j\rangle$ are the basis vectors describing the black and white atoms respectively.

6.6.1 Nearest neighbor currents

As mentioned earlier, graphene exhibits two types of currents: first, which is related to the nearest neighbor hoppings and second, which occurs due to the second neighbor hoppings. Since the former type involves the three nearest neighbors of a given atom, we need not look at the entire Hilbert space. We only look at a subspace of the pair of concerned atoms.

The eigenvector defining the subspace corresponding to the atoms of different types can be expressed in the general form as given in Eq.6.22,

$$\left|u_{\boldsymbol{k}}(\boldsymbol{R}_i^b, \boldsymbol{R}_j^w)\right\rangle = e^{i\boldsymbol{k}\cdot\boldsymbol{R}_i^b}\sqrt{\frac{1+\frac{z}{r}}{2}}\left|B_i\right\rangle + e^{i\boldsymbol{k}\cdot\boldsymbol{R}_j^w}e^{i\phi}\sqrt{\frac{1-\frac{z}{r}}{2}}\left|W_j\right\rangle. \tag{6.23}$$

Here, $\boldsymbol{R}_i^b$ is the position of the B_i type of atom and $\boldsymbol{R}_j^w$ is the position of the W_j type of atom in its vicinity. For example, if B_i is the black atom of Fig.6.4 at $\boldsymbol{R}_0^b = \left(-\frac{a_0}{2}, \frac{\sqrt{3}a_0}{2}\right)$ then W_i would be one of its three nearest neighbors at $\boldsymbol{R}_j^w \in \{\boldsymbol{R}_0^b + \boldsymbol{a}_1, \boldsymbol{R}_0^b + \boldsymbol{a}_2, \boldsymbol{R}_0^b + \boldsymbol{a}_3\}$. This vector forms the sub-density matrix,

$$\rho\left(\boldsymbol{R}_i^b, \boldsymbol{R}_j^w\right) = \left|u_{\boldsymbol{k}}(\boldsymbol{R}_i^b, \boldsymbol{R}_j^w)\right\rangle\left\langle u_{\boldsymbol{k}}(\boldsymbol{R}_i^b, \boldsymbol{R}_j^w)\right| = \begin{pmatrix} \frac{1+\frac{z}{r}}{2} & e^{-i\boldsymbol{k}\cdot\left(\boldsymbol{R}_j^w - \boldsymbol{R}_i^b\right)}e^{i\phi}\sqrt{\frac{1-\frac{z}{r}}{2}}\sqrt{\frac{1+\frac{z}{r}}{2}} \\ e^{i\boldsymbol{k}\cdot\left(\boldsymbol{R}_j^w - \boldsymbol{R}_i^b\right)}e^{-i\phi}\sqrt{\frac{1-\frac{z}{r}}{2}}\sqrt{\frac{1+\frac{z}{r}}{2}} & \frac{1-\frac{z}{r}}{2} \end{pmatrix}. \tag{6.24}$$

The expectation value of the current density operator is defined in terms of the interaction matrix, The current between nearest neighbor atoms is,

$$\begin{aligned}
\left\langle J\left(\boldsymbol{R}_i^b, \boldsymbol{R}_j^w\right)\right\rangle &= \mathrm{Tr}\left(\rho\left(\boldsymbol{R}_i^b, \boldsymbol{R}_j^w\right)\begin{pmatrix} 0 & -it_1 \\ it_1 & 0 \end{pmatrix}\right) \\
&= \begin{pmatrix} it_1\left(e^{-i\boldsymbol{k}\cdot\left(\boldsymbol{R}_j^w - \boldsymbol{R}_i^b\right)}e^{-i\phi}\sqrt{\frac{1-\frac{z}{r}}{2}}\sqrt{\frac{1+\frac{z}{r}}{2}}\right) & -it_1\left(\frac{1+\frac{z}{r}}{2}\right) \\ it_1\left(\frac{1-\frac{z}{r}}{2}\right) & -it_1\left(e^{i\boldsymbol{k}\cdot\left(\boldsymbol{R}_j^w - \boldsymbol{R}_i^b\right)}e^{i\phi}\sqrt{\frac{1-\frac{z}{r}}{2}}\sqrt{\frac{1+\frac{z}{r}}{2}}\right) \end{pmatrix} \\
&= it_1\left(-e^{i\boldsymbol{k}\cdot\left(\boldsymbol{R}_j^w - \boldsymbol{R}_i^b\right)}e^{i\phi}\sqrt{\frac{1-\frac{z}{r}}{2}}\sqrt{\frac{1+\frac{z}{r}}{2}}\right) + e^{-i\boldsymbol{k}\cdot\left(\boldsymbol{R}_j^w - \boldsymbol{R}_i^b\right)}e^{-i\phi}\sqrt{\frac{1-\frac{z}{r}}{2}}\sqrt{\frac{1+\frac{z}{r}}{2}} \\
&= -it_1\frac{\sqrt{1-\frac{z^2}{r^2}}}{2}\left(e^{i\boldsymbol{k}\cdot\left(\boldsymbol{R}_j^w - \boldsymbol{R}_i^b\right)}e^{i\phi} - e^{-i\boldsymbol{k}\cdot\left(\boldsymbol{R}_j^w - \boldsymbol{R}_i^b\right)}e^{-i\phi}\right) \\
&= -t_1\sqrt{1-\frac{z^2}{r^2}}\left[\sin\left(\boldsymbol{k}\cdot\left(\boldsymbol{R}_j^w - \boldsymbol{R}_i^b\right) + \phi\right)\right].
\end{aligned} \tag{6.25}$$

The above expression of the current density operator is with a double index. We can simplify this by writing it in terms of a single bond index corresponding to the bond $\boldsymbol{a}_i$,

$$\left\langle J_i^{bw} \right\rangle = -t_1 \sqrt{1 - \frac{z^2}{r^2}} \left[\sin\left(\boldsymbol{k} \cdot \boldsymbol{a}_i + \phi\right) \right]. \tag{6.26}$$

6.6.2 Second neighbor currents

The second neighbor currents are defined between the same types of atoms, so between B_i and B_j or between W_i and W_j. We consider these two cases separately.

Current between black atoms

The Bloch vector defined for the atoms B_i, B_j at positions $\boldsymbol{R}_i^b, \boldsymbol{R}_j^b$ respectively is,

$$\left| u_{\boldsymbol{k}}(\boldsymbol{R}_i^b, \boldsymbol{R}_j^b) \right\rangle = e^{i\boldsymbol{k}\cdot\boldsymbol{R}_i^b} \sqrt{\frac{1+\frac{z}{r}}{2}} \left| B_i \right\rangle + e^{i\boldsymbol{k}\cdot\boldsymbol{R}_j^b} \sqrt{\frac{1+\frac{z}{r}}{2}} \left| B_j \right\rangle, \tag{6.27}$$

for which the sub-density matrix is,

$$\rho(\boldsymbol{R}_i^b, \boldsymbol{R}_j^b) = \begin{pmatrix} \frac{1+\frac{z}{r}}{2} & e^{-i\boldsymbol{k}\cdot\left(\boldsymbol{R}_j^b - \boldsymbol{R}_i^b\right)} \left(\frac{1+\frac{z}{r}}{2}\right) \\ e^{i\boldsymbol{k}\cdot\left(\boldsymbol{R}_j^b - \boldsymbol{R}_i^b\right)} \left(\frac{1+\frac{z}{r}}{2}\right) & \frac{1+\frac{z}{r}}{2} \end{pmatrix}. \tag{6.28}$$

We define the current density operator in terms of the vectors $\boldsymbol{a}_i$, $\boldsymbol{R}_j^b - \boldsymbol{R}_i^b = \boldsymbol{a}_\alpha - \boldsymbol{a}_\beta$, in order to capture the chirality,

$$J\left(\boldsymbol{R}_i^b, \boldsymbol{R}_j^b\right) = \begin{pmatrix} 0 & sgn\left(\hat{\boldsymbol{z}} \cdot \left(\boldsymbol{a}_\alpha \times -\boldsymbol{a}_\beta\right)\right) t_2 \\ sgn\left(\hat{\boldsymbol{z}} \cdot \left(\boldsymbol{a}_\alpha \times -\boldsymbol{a}_\beta\right)\right) t_2 & 0 \end{pmatrix}. \tag{6.29}$$

Therefore, the expectation value is,

$$\begin{aligned}
\left\langle J\left(\boldsymbol{R}_i^b, \boldsymbol{R}_j^b\right) \right\rangle &= \mathrm{Tr}\left(\rho\left(\boldsymbol{R}_i^b, \boldsymbol{R}_j^b\right) \begin{pmatrix} 0 & sgn\left(\hat{\boldsymbol{z}} \cdot \left(\boldsymbol{a}_\alpha \times -\boldsymbol{a}_\beta\right)\right) t_2 \\ sgn\left(\hat{\boldsymbol{z}} \cdot \left(\boldsymbol{a}_\alpha \times -\boldsymbol{a}_\beta\right)\right) t_2 & 0 \end{pmatrix} \right) \\
&= \mathrm{Tr} \begin{pmatrix} sgn\left(\hat{\boldsymbol{z}} \cdot \left(\boldsymbol{a}_\alpha \times -\boldsymbol{a}_\beta\right)\right) t_2 e^{i\boldsymbol{k}\cdot\left(\boldsymbol{R}_j^b - \boldsymbol{R}_i^b\right)} \left(\frac{1+\frac{z}{r}}{2}\right) & sgn\left(\hat{\boldsymbol{z}} \cdot \left(\boldsymbol{a}_\alpha \times -\boldsymbol{a}_\beta\right)\right) t_2 \left(\frac{1+\frac{z}{r}}{2}\right) \\ sgn\left(\hat{\boldsymbol{z}} \cdot \left(\boldsymbol{a}_\alpha \times -\boldsymbol{a}_\beta\right)\right) t_2 \left(\frac{1+\frac{z}{r}}{2}\right) & sgn\left(\hat{\boldsymbol{z}} \cdot \left(\boldsymbol{a}_\alpha \times -\boldsymbol{a}_\beta\right)\right) t_2 e^{-i\boldsymbol{k}\cdot\left(\boldsymbol{R}_j^b - \boldsymbol{R}_i^b\right)} \left(\frac{1+\frac{z}{r}}{2}\right) \end{pmatrix} \\
&= sgn\left(\hat{\boldsymbol{z}} \cdot \left(\boldsymbol{a}_\alpha \times -\boldsymbol{a}_\beta\right)\right) t_2 \left(\frac{1+\frac{z}{r}}{2}\right) \left(e^{i\boldsymbol{k}\cdot\left(\boldsymbol{R}_j^b - \boldsymbol{R}_i^b\right)} + e^{-i\boldsymbol{k}\cdot\left(\boldsymbol{R}_j^b - \boldsymbol{R}_i^b\right)} \right) \\
&= sgn\left(\hat{\boldsymbol{z}} \cdot \left(\boldsymbol{a}_\alpha \times -\boldsymbol{a}_\beta\right)\right) t_2 \left(1 + \frac{z}{r}\right) \cos\left(\boldsymbol{k} \cdot \left(\boldsymbol{R}_j^b - \boldsymbol{R}_i^b\right)\right).
\end{aligned} \tag{6.30}$$

Similar to the previous case, we can re-write the current density using a single bond index $\boldsymbol{b}_i$[3],

$$\left\langle J_i^{bb} \right\rangle = sgn\left(\hat{\boldsymbol{z}} \cdot \left(\boldsymbol{a}_\alpha \times -\boldsymbol{a}_\beta\right)\right) t_2 \left(1 + \frac{z}{r}\right) \cos\left(\boldsymbol{k} \cdot \boldsymbol{b}_i\right). \tag{6.31}$$

Current between white atoms

The Bloch vector defined for the atoms W_i, W_j at positions $\boldsymbol{R}_i^w, \boldsymbol{R}_j^w$ respectively is,

$$\left|u_{\boldsymbol{k}}(\boldsymbol{R}_i^w, \boldsymbol{R}_j^w)\right\rangle = e^{i\boldsymbol{k}\cdot\boldsymbol{R}_i^w} e^{i\phi} \sqrt{\frac{1-\frac{z}{r}}{2}} \left|W_i\right\rangle + e^{i\boldsymbol{k}\cdot\boldsymbol{R}_j^w} e^{i\phi} \sqrt{\frac{1-\frac{z}{r}}{2}} \left|W_j\right\rangle, \tag{6.32}$$

whose sub-density matrix has the form,

$$\rho(\boldsymbol{R}_i^w, \boldsymbol{R}_j^w) = \begin{pmatrix} \frac{1-\frac{z}{r}}{2} & e^{-i\boldsymbol{k}\cdot\left(\boldsymbol{R}_j^w - \boldsymbol{R}_i^w\right)} \left(\frac{1-\frac{z}{r}}{2}\right) \\ e^{i\boldsymbol{k}\cdot\left(\boldsymbol{R}_j^w - \boldsymbol{R}_i^w\right)} \left(\frac{1-\frac{z}{r}}{2}\right) & \frac{1-\frac{z}{r}}{2} \end{pmatrix}. \tag{6.33}$$

The hopping matrix is defined exactly as it was the case for B_i, B_j atoms,

$$J\left(\boldsymbol{R}_i^w, \boldsymbol{R}_j^w\right) = \begin{pmatrix} 0 & -sgn\left(\hat{\boldsymbol{z}} \cdot \left(\boldsymbol{a}_\alpha \times -\boldsymbol{a}_\beta\right)\right) t_2 \\ -sgn\left(\hat{\boldsymbol{z}} \cdot \left(\boldsymbol{a}_\alpha \times -\boldsymbol{a}_\beta\right)\right) t_2 & 0 \end{pmatrix}. \tag{6.34}$$

The expression for $\left\langle J\left(\boldsymbol{R}_i^w, \boldsymbol{R}_j^w\right)\right\rangle$ is,

$$\begin{aligned}
\left\langle J^{ww}\left(\boldsymbol{R}_i^w, \boldsymbol{R}_j^w\right)\right\rangle &= \mathrm{Tr}\left(\rho\left(\boldsymbol{R}_i^w, \boldsymbol{R}_j^w\right) \begin{pmatrix} 0 & -sgn\left(\hat{\boldsymbol{z}} \cdot \left(\boldsymbol{a}_\alpha \times -\boldsymbol{a}_\beta\right)\right) t_2 \\ -sgn\left(\hat{\boldsymbol{z}} \cdot \left(\boldsymbol{a}_\alpha \times -\boldsymbol{a}_\beta\right)\right) t_2 & 0 \end{pmatrix}\right) \\
&= \mathrm{Tr}\begin{pmatrix} -sgn\left(\hat{\boldsymbol{z}} \cdot \left(\boldsymbol{a}_\alpha \times -\boldsymbol{a}_\beta\right)\right) t_2 e^{i\boldsymbol{k}\cdot\left(\boldsymbol{R}_j^w - \boldsymbol{R}_i^w\right)} \left(\frac{1-\frac{z}{r}}{2}\right) & -sgn\left(\hat{\boldsymbol{z}} \cdot \left(\boldsymbol{a}_\alpha \times -\boldsymbol{a}_\beta\right)\right) t_2 \left(\frac{1-\frac{z}{r}}{2}\right) \\ -sgn\left(\hat{\boldsymbol{z}} \cdot \left(\boldsymbol{a}_\alpha \times -\boldsymbol{a}_\beta\right)\right) t_2 \left(\frac{1-\frac{z}{r}}{2}\right) & -sgn\left(\hat{\boldsymbol{z}} \cdot \left(\boldsymbol{a}_\alpha \times -\boldsymbol{a}_\beta\right)\right) t_2 e^{-i\boldsymbol{k}\cdot\left(\boldsymbol{R}_j^w - \boldsymbol{R}_i^w\right)} \left(\frac{1-\frac{z}{r}}{2}\right) \end{pmatrix} \\
&= -sgn\left(\hat{\boldsymbol{z}} \cdot \left(\boldsymbol{a}_\alpha \times -\boldsymbol{a}_\beta\right)\right) t_2 \left(\frac{1-\frac{z}{r}}{2}\right) \left(e^{i\boldsymbol{k}\cdot\left(\boldsymbol{R}_j^w - \boldsymbol{R}_i^w\right)} + e^{-i\boldsymbol{k}\cdot\left(\boldsymbol{R}_j^w - \boldsymbol{R}_i^w\right)}\right) \\
&= -sgn\left(\hat{\boldsymbol{z}} \cdot \left(\boldsymbol{a}_\alpha \times -\boldsymbol{a}_\beta\right)\right) t_2 \left(1 - \frac{z}{r}\right) \cos\left(\boldsymbol{k} \cdot \left(\boldsymbol{R}_j^w - \boldsymbol{R}_i^w\right)\right).
\end{aligned} \tag{6.35}$$

Or the expectation value in terms of the bond index $\boldsymbol{b}_i$ is,

$$\left\langle J_i^{ww} \right\rangle = -sgn\left(\hat{\boldsymbol{z}} \cdot \left(\boldsymbol{a}_\alpha \times -\boldsymbol{a}_\beta\right)\right) t_2 \left(1 - \frac{z}{r}\right) \cos\left(\boldsymbol{k} \cdot \boldsymbol{b}_i\right). \tag{6.36}$$

Note that each type of current is dependent on the orientation of the bond and not the position of the atom. Therefore, we see a periodicity of the current flow in the lattice. Note also that the values of $\left\langle J_i^{bb} \right\rangle$ and $\left\langle J_i^{ww} \right\rangle$ may differ from each other not only because of the overall negative sign

[3]The cross product $(\boldsymbol{a}_\alpha \times \boldsymbol{a}_\beta)$ can be expressed in terms of $\boldsymbol{R}_j - \boldsymbol{R}_j = \boldsymbol{b}_i$

but also because the former is multiplied by the weight $\left(1+\frac{z}{r}\right)$ whereas as the latter is multiplied by $\left(1-\frac{z}{r}\right)$.

In Fig.6.6, we show the variation of the current density of the Bloch states in the interval $k_y = [-2\pi, 2\pi]$, $k_x = 0$ for $t_1 = 1$ in Hartree units and $t_2 = 0.1$ in Hartree units. We do this only for illustration, as the actual t_2 is known to be much smaller relative to t_1. We show the plot of currents for only one type of atom but a similar plot can be constructed for the other type.

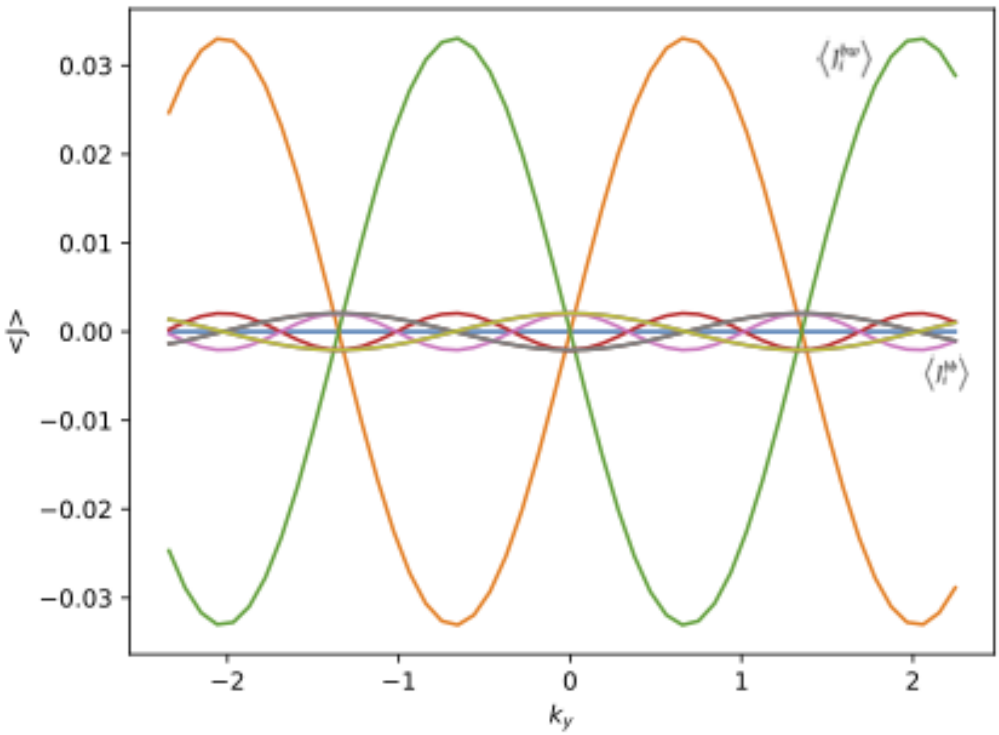

Figure 6.6: Current densities between an atom at R_i^b and its nine neighbors. The orange, green and blue curves are the $\langle J_i^{bw} \rangle$. Notice that along the $(0, k_y)$ direction, one of the nearest neighbor current (the blue curve) is 0 for all k_y. At $\boldsymbol{k} = (0,0)$, $\langle J_i^{bw} \rangle = 0 \ \forall i$. The smaller curves are the same atom contributions $\langle J_i^{bb} \rangle$.

The larger contributions in the Fig.6.6, shown by the orange and the green curves are from $\langle J_{\boldsymbol{a2}}^{bw} \rangle$ and $\langle J_{\boldsymbol{a3}}^{bw} \rangle$ where $\boldsymbol{a}_2$ and $\boldsymbol{a}_3$ are shown in Fig.6.4. The third $\langle J_{\boldsymbol{a}_1}^{bw} \rangle$ contribution is 0 for all k_y (blue line) as the current flow is perpendicular to the direction of $\boldsymbol{k}$. Looking back at the analytical expression for currents Eq.6.26, if the current flow is in the x-direction then its sine component will be 0. The fact that at $\boldsymbol{k} = (0,0)$ all three nearest neighbor currents are 0 also checks from the analytical expression as $\sin(0) = 0$.

Fig.6.6 shows that the second neighbor currents are much smaller than the nearest neighbor currents. This difference is explained by the expression of Eq.6.31 where we can see that $\langle J_i^{bb} \rangle \sim t_2$, t_2 is 10 times smaller than t_1. We do not show $\langle J_i^{ww} \rangle$ in the figure but for every $\langle J_i^{bb} \rangle$ there is a corresponding $\langle J_i^{ww} \rangle$. These currents are even functions of $\boldsymbol{k}$ which is also what the expression

Eq.6.31 shows. This does not violate the continuity equation as we can see that $\sum_i \langle J_i^{bb} \rangle = 0$.

Hence we may also conclude that the continuity equation must guarantee that $\sum_i \langle J_i^{bw} \rangle = -\sum_i \langle J_i^{wb} \rangle = 0$, $\sum_i \langle J_i^{bb} \rangle = 0$ and $\sum_i \langle J_i^{ww} \rangle = 0$ i.e the three types of currents must all sum to zero individually. Physically this means that our solid remains electrically neutral and that the currents leaving and entering a surface that surrounds any atom within the solid must all sum to zero.

6.6.3 Current density for valley states in Graphene

As discussed earlier the quantum dot states are formed out of a superposition of the valley states with the corresponding envelope function. For graphene, the valley states are at the points $\boldsymbol{K} = \frac{2\pi}{3a_0}\left(1, \frac{1}{\sqrt{3}}\right)$ and $\boldsymbol{K}' = \frac{2\pi}{3a_0}\left(1, -\frac{1}{\sqrt{3}}\right)$ as mentioned earlier in this chapter. These are the points at which the band gap closes as $t_2 = 0$. In this section we derive the expressions for all the different types of currents for the valley states which are a superposition of the $\boldsymbol{K}$ and $\boldsymbol{K}'$ states. We do not take into account the envelope functions.

Nearest neighbor currents of the valley states

Our valley states are now a superposition of the Bloch states at the two Dirac points mentioned earlier. We redefine $\boldsymbol{k} = \boldsymbol{K}$ and $-\boldsymbol{k} = -\boldsymbol{K} = \boldsymbol{K}'$ for consistency. $\boldsymbol{K}$ and $\boldsymbol{K}'$ are not directly related by any reciprocal lattice translation but $\boldsymbol{K}' = -\boldsymbol{K} + \boldsymbol{G}_1 + \boldsymbol{G}_2$ where $\boldsymbol{G}_1 = \frac{2\pi}{3a_0}(1, \sqrt{3})$, $\boldsymbol{G}_2 = \frac{2\pi}{3a_0}(1, -\sqrt{3})$ are the reciprocal lattice vectors of the hexagonal graphene lattice. This also mean that the states at $\boldsymbol{K}'$ and $-\boldsymbol{K}$ belong to the same representation. The valley state is,

$$|u\rangle = \frac{1}{\sqrt{2}}\left(\left|u^{\boldsymbol{k}}(\boldsymbol{R}_i^b, \boldsymbol{R}_j^w)\right\rangle + \left|u^{-\boldsymbol{k}}(\boldsymbol{R}_i^b, \boldsymbol{R}_j^w)\right\rangle\right). \tag{6.37}$$

We calculate the expectation value using the eigenvectors and not the sub-density matrix as the former method allows for certain direct simplifications.[4]

$$\begin{aligned}
\left\langle J\left(\boldsymbol{R}_i^b,\boldsymbol{R}_j^w\right)\right\rangle &= \frac{1}{2}\left(\left\langle u^{\boldsymbol{k}}(R_i^b,R_j^w)+u^{-\boldsymbol{k}}(R_i^b,R_j^w)|J^{bw}|u^{\boldsymbol{k}}(R_i^b,R_j^w)+u^{-\boldsymbol{k}}(R_i^b,R_j^w)\right\rangle\right)\\
&= \frac{1}{2}\begin{pmatrix} e^{-i\boldsymbol{k}\cdot\boldsymbol{R}_i^b}\sqrt{\frac{1+\frac{z}{r}}{2}}, & e^{-i\boldsymbol{k}\cdot\boldsymbol{R}_j^w}e^{-i\phi}\sqrt{\frac{1-\frac{z}{r}}{2}}\end{pmatrix}\begin{pmatrix}0 & -it_1\\ it_1 & 0\end{pmatrix}\begin{pmatrix} e^{-i\boldsymbol{k}\cdot\boldsymbol{R}_i^b}\sqrt{\frac{1-\frac{z}{r}}{2}}, \\ e^{-i\boldsymbol{k}\cdot\boldsymbol{R}_j^w}e^{-i\phi}\sqrt{\frac{1+\frac{z}{r}}{2}}\end{pmatrix}\\
&+\frac{1}{2}\begin{pmatrix} e^{i\boldsymbol{k}\cdot\boldsymbol{R}_i^b}\sqrt{\frac{1-\frac{z}{r}}{2}}, & e^{i\boldsymbol{k}\cdot\boldsymbol{R}_j^w}e^{i\phi}\sqrt{\frac{1+\frac{z}{r}}{2}}\end{pmatrix}\begin{pmatrix}0 & -it_1\\ it_1 & 0\end{pmatrix}\begin{pmatrix} e^{i\boldsymbol{k}\cdot\boldsymbol{R}_i^b}\sqrt{\frac{1+\frac{z}{r}}{2}}, \\ e^{i\boldsymbol{k}\cdot\boldsymbol{R}_j^w}e^{i\phi}\sqrt{\frac{1-\frac{z}{r}}{2}}\end{pmatrix}\\
&= \frac{1}{2}\begin{pmatrix} e^{-i\boldsymbol{k}\cdot\boldsymbol{R}_i^b}\sqrt{\frac{1+\frac{z}{r}}{2}}, & e^{-i\boldsymbol{k}\cdot\boldsymbol{R}_j^w}e^{-i\phi}\sqrt{\frac{1-\frac{z}{r}}{2}}\end{pmatrix}\begin{pmatrix} -it_1e^{-i\boldsymbol{k}\cdot\boldsymbol{R}_j^w}e^{-i\phi}\sqrt{\frac{1+\frac{z}{r}}{2}}, \\ it_1e^{-i\boldsymbol{k}\cdot\boldsymbol{R}_i^b}\sqrt{\frac{1-\frac{z}{r}}{2}}\end{pmatrix}\\
&+\frac{1}{2}\begin{pmatrix} e^{i\boldsymbol{k}\cdot\boldsymbol{R}_i^b}\sqrt{\frac{1-\frac{z}{r}}{2}}, & e^{i\boldsymbol{k}\cdot\boldsymbol{R}_j^w}e^{i\phi}\sqrt{\frac{1+\frac{z}{r}}{2}}\end{pmatrix}\begin{pmatrix} -it_1e^{i\boldsymbol{k}\cdot\boldsymbol{R}_j^w}e^{i\phi}\sqrt{\frac{1-\frac{z}{r}}{2}}, \\ it_1e^{i\boldsymbol{k}\cdot\boldsymbol{R}_i^b}\sqrt{\frac{1+\frac{z}{r}}{2}}\end{pmatrix}\\
&= -i\frac{t_1}{2}\left[e^{-i\boldsymbol{k}\cdot\left(\boldsymbol{R}_j^w+\boldsymbol{R}_i^b\right)}e^{-i\phi}\frac{1+\frac{z}{r}}{2}-e^{-i\boldsymbol{k}\cdot\left(\boldsymbol{R}_j^w+\boldsymbol{R}_i^b\right)}e^{-i\phi}\frac{1-\frac{z}{r}}{2}\right]\\
&-i\frac{t_1}{2}\left[e^{i\boldsymbol{k}\cdot\left(\boldsymbol{R}_j^w+\boldsymbol{R}_i^b\right)}e^{i\phi}\frac{1-\frac{z}{r}}{2}-e^{i\boldsymbol{k}\cdot\left(\boldsymbol{R}_j^w+\boldsymbol{R}_i^b\right)}e^{i\phi}\frac{1+\frac{z}{r}}{2}\right]\\
&= -\frac{it_1}{4}\left(e^{-i\boldsymbol{k}\cdot\left(\boldsymbol{R}_j^w+\boldsymbol{R}_i^b\right)}e^{-i\phi}\left[1+\frac{z}{r}-1+\frac{z}{r}\right]+e^{i\boldsymbol{k}\cdot\left(\boldsymbol{R}_j^w+\boldsymbol{R}_i^b\right)}e^{i\phi}\left[1-\frac{z}{r}+1+\frac{z}{r}\right]\right)\\
&= -it_1\frac{z}{2r}\left(e^{-i\boldsymbol{k}\cdot\left(\boldsymbol{R}_j^w+\boldsymbol{R}_i^b\right)}e^{-i\phi}-e^{i\boldsymbol{k}\cdot\left(\boldsymbol{R}_j^w+\boldsymbol{R}_i^b\right)}e^{i\phi}\right)\\
&= -it_1\frac{z}{2r}\left[\sin\left(\boldsymbol{k}\cdot\left(\boldsymbol{R}_j^w+\boldsymbol{R}_i^b\right)+\phi\right)\right].
\end{aligned}\tag{6.38}$$

$\left\langle J_i^{bb}\right\rangle$ of the valley states

The valley state vector for second neighbor black atoms is,

$$\begin{aligned}
\frac{1}{\sqrt{2}}\left(\left|u^{\boldsymbol{k}}\left(\boldsymbol{R}_i^b,\boldsymbol{R}_j^b\right)\right\rangle+\left|u^{-\boldsymbol{k}}\left(\boldsymbol{R}_i^b,\boldsymbol{R}_j^b\right)\right\rangle\right) &= \frac{1}{\sqrt{2}}\left(e^{i\boldsymbol{k}\cdot\boldsymbol{R}_i^b}\sqrt{\frac{1+\frac{z}{r}}{2}}\left|B_i\right\rangle+e^{i\boldsymbol{k}\cdot\boldsymbol{R}_j^b}\sqrt{\frac{1+\frac{z}{r}}{2}}\left|B_j\right\rangle\right.\\
&\left.+e^{-i\boldsymbol{k}\cdot\boldsymbol{R}_i^b}\sqrt{\frac{1-\frac{z}{r}}{2}}\left|B_i\right\rangle+e^{-i\boldsymbol{k}\cdot\boldsymbol{R}_j^b}\sqrt{\frac{1-\frac{z}{r}}{2}}\left|B_j\right\rangle\right).
\end{aligned}\tag{6.39}$$

[4] In the second step we have skipped the diagonal terms as $\left\langle u^{\boldsymbol{k}}(\boldsymbol{R}_i^b,\boldsymbol{R}_j^w)|\boldsymbol{J}_i|u^{\boldsymbol{k}}(\boldsymbol{R}_i^b,\boldsymbol{R}_j^w)\right\rangle = -\left\langle u^{-\boldsymbol{k}}(\boldsymbol{R}_i^b,\boldsymbol{R}_j^w)|\boldsymbol{J}_i|u^{-\boldsymbol{k}}(\boldsymbol{R}_i^b,\boldsymbol{R}_j^w)\right\rangle$.

The current operator between the black valleys states is,

$$
\begin{aligned}
&\left\langle J\left(\boldsymbol{R}_i^b,\boldsymbol{R}_j^b\right)\right\rangle = \frac{1}{2}\Bigg(\left\langle u^{\boldsymbol{k}}(R_i^b,R_j^b)|J^{bb}|u^{\boldsymbol{k}}(R_i^b,R_j^b)\right\rangle + \left\langle u^{-\boldsymbol{k}}(R_i^b,R_j^b)|J^{bb}|u^{-\boldsymbol{k}}(R_i^b,R_j^b)\right\rangle \\
&+\left\langle u^{\boldsymbol{k}}(R_i^b,R_j^b)|J^{bb}|u^{-\boldsymbol{k}}(R_i^b,R_j^b)\right\rangle + \left\langle u^{-\boldsymbol{k}}(R_i^b,R_j^b)|J^{bb}|u^{\boldsymbol{k}}(R_i^b,R_j^b)\right\rangle\Bigg) \\
&=\frac{1}{2}sgn(\hat{z}\cdot(\boldsymbol{a}_\alpha\times\boldsymbol{a}_\beta))t_2\cos\left(\boldsymbol{k}\cdot\left(\boldsymbol{R}_j^b-\boldsymbol{R}_i^b\right)\right)\left(1+\frac{z}{r}\right) \\
&+\frac{1}{2}\left(e^{i\boldsymbol{k}\cdot\boldsymbol{R}_i^b}\sqrt{\frac{1-\frac{z}{r}}{2}},e^{i\boldsymbol{k}\cdot\boldsymbol{R}_j^b}\sqrt{\frac{1-\frac{z}{r}}{2}}\right)\begin{pmatrix}0 & sgn(\hat{z}\cdot(\boldsymbol{a}_\alpha\times\boldsymbol{a}_\beta))t_2\\ sgn(\hat{z}\cdot(\boldsymbol{a}_\alpha\times\boldsymbol{a}_\beta))t_2 & 0\end{pmatrix}\begin{pmatrix}e^{-i\boldsymbol{k}\cdot\boldsymbol{R}_i^b}\sqrt{\frac{1-\frac{z}{r}}{2}}\\ e^{-i\boldsymbol{k}\cdot\boldsymbol{R}_j^b}\sqrt{\frac{1-\frac{z}{r}}{2}}\end{pmatrix} \\
&+\frac{1}{2}\left(e^{-i\boldsymbol{k}\cdot\boldsymbol{R}_i^b}\sqrt{\frac{1+\frac{z}{r}}{2}},e^{-i\boldsymbol{k}\cdot\boldsymbol{R}_j^b}\sqrt{\frac{1+\frac{z}{r}}{2}}\right)\begin{pmatrix}0 & sgn(\hat{z}\cdot(\boldsymbol{a}_\alpha\times\boldsymbol{a}_\beta))t_2\\ sgn(\hat{z}\cdot(\boldsymbol{a}_\alpha\times\boldsymbol{a}_\beta))t_2 & 0\end{pmatrix}\begin{pmatrix}e^{-i\boldsymbol{k}\cdot\boldsymbol{R}_i^b}\sqrt{\frac{1-\frac{z}{r}}{2}}\\ e^{-i\boldsymbol{k}\cdot\boldsymbol{R}_j^b}\sqrt{\frac{1-\frac{z}{r}}{2}}\end{pmatrix} \\
&+\frac{1}{2}\left(e^{i\boldsymbol{k}\cdot\boldsymbol{R}_i^b}\sqrt{\frac{1-\frac{z}{r}}{2}},e^{i\boldsymbol{k}\cdot\boldsymbol{R}_j^b}\sqrt{\frac{1-\frac{z}{r}}{2}}\right)\begin{pmatrix}0 & sgn(\hat{z}\cdot(\boldsymbol{a}_\alpha\times\boldsymbol{a}_\beta))t_2\\ sgn(\hat{z}\cdot(\boldsymbol{a}_\alpha\times\boldsymbol{a}_\beta))t_2 & 0\end{pmatrix}\begin{pmatrix}e^{i\boldsymbol{k}\cdot\boldsymbol{R}_i^b}\sqrt{\frac{1+\frac{z}{r}}{2}}\\ e^{i\boldsymbol{k}\cdot\boldsymbol{R}_j^b}\sqrt{\frac{1+\frac{z}{r}}{2}}\end{pmatrix} \\
&=\frac{1}{2}sgn(\hat{z}\cdot(\boldsymbol{a}_\alpha\times\boldsymbol{a}_\beta))t_2\cos\left(\boldsymbol{k}\cdot\left(\boldsymbol{R}_j^b-\boldsymbol{R}_i^b\right)\right)\left(1+\frac{z}{r}\right) \\
&+\frac{1}{2}\left(e^{i\boldsymbol{k}\cdot\boldsymbol{R}_i^b}\sqrt{\frac{1-\frac{z}{r}}{2}},e^{i\boldsymbol{k}\cdot\boldsymbol{R}_j^b}\sqrt{\frac{1-\frac{z}{r}}{2}}\right)\begin{pmatrix}sgn(\hat{z}\cdot(\boldsymbol{a}_\alpha\times\boldsymbol{a}_\beta))t_2e^{-i\boldsymbol{k}\cdot\boldsymbol{R}_j^b}\sqrt{\frac{1-\frac{z}{r}}{2}}\\ sgn(\hat{z}\cdot(\boldsymbol{a}_\alpha\times\boldsymbol{a}_\beta))t_2e^{-i\boldsymbol{k}\cdot\boldsymbol{R}_i^b}\sqrt{\frac{1-\frac{z}{r}}{2}}\end{pmatrix} \\
&+\frac{1}{2}\left(e^{-i\boldsymbol{k}\cdot\boldsymbol{R}_i^b}\sqrt{\frac{1+\frac{z}{r}}{2}},e^{-i\boldsymbol{k}\cdot\boldsymbol{R}_j^b}\sqrt{\frac{1+\frac{z}{r}}{2}}\right)\begin{pmatrix}sgn(\hat{z}\cdot(\boldsymbol{a}_\alpha\times\boldsymbol{a}_\beta))t_2e^{-i\boldsymbol{k}\cdot\boldsymbol{R}_j^b}\sqrt{\frac{1-\frac{z}{r}}{2}}\\ sgn(\hat{z}\cdot(\boldsymbol{a}_\alpha\times\boldsymbol{a}_\beta))t_2e^{-i\boldsymbol{k}\cdot\boldsymbol{R}_i^b}\sqrt{\frac{1-\frac{z}{r}}{2}}\end{pmatrix} \\
&+\frac{1}{2}\left(e^{i\boldsymbol{k}\cdot\boldsymbol{R}_i^b}\sqrt{\frac{1-\frac{z}{r}}{2}},e^{i\boldsymbol{k}\cdot\boldsymbol{R}_j^b}\sqrt{\frac{1-\frac{z}{r}}{2}}\right)\begin{pmatrix}sgn(\hat{z}\cdot(\boldsymbol{a}_\alpha\times\boldsymbol{a}_\beta))t_2e^{i\boldsymbol{k}\cdot\boldsymbol{R}_j^b}\sqrt{\frac{1+\frac{z}{r}}{2}}\\ sgn(\hat{z}\cdot(\boldsymbol{a}_\alpha\times\boldsymbol{a}_\beta))t_2e^{i\boldsymbol{k}\cdot\boldsymbol{R}_i^b}\sqrt{\frac{1+\frac{z}{r}}{2}}\end{pmatrix}.
\end{aligned}
\tag{6.40}
$$

$$\begin{aligned}\left\langle J\left(\boldsymbol{R}_i^b,\boldsymbol{R}_j^b\right)\right\rangle &= \frac{1}{2}sgn(\hat{z}\cdot(\boldsymbol{a}_\alpha\times\boldsymbol{a}_\beta))t_2\Bigg[\cos\left(\boldsymbol{k}\cdot\left(\boldsymbol{R}_j^b-\boldsymbol{R}_i^b\right)\right)\left(1+\frac{z}{r}\right)+\cos\left(\boldsymbol{k}\cdot\left(\boldsymbol{R}_j^b-\boldsymbol{R}_i^b\right)\right)\left(1-\frac{z}{r}\right)\\ &+\left(e^{-i\boldsymbol{k}\cdot\left(\boldsymbol{R}_j^b+\boldsymbol{R}_i^b\right)}+e^{-i\boldsymbol{k}\cdot\left(\boldsymbol{R}_j^b+\boldsymbol{R}_i^b\right)}+e^{i\boldsymbol{k}\cdot\left(\boldsymbol{R}_j^b+\boldsymbol{R}_i^b\right)}+e^{i\boldsymbol{k}\cdot\left(\boldsymbol{R}_j^b+\boldsymbol{R}_i^b\right)}\right)\frac{\sqrt{1-\frac{z^2}{r^2}}}{2}\Bigg]\\ &= \frac{1}{2}sgn(\hat{z}\cdot(\boldsymbol{a}_\alpha\times\boldsymbol{a}_\beta))t_2\Bigg[\cos\left(\boldsymbol{k}\cdot\left(\boldsymbol{R}_j^b-\boldsymbol{R}_i^b\right)\right)\left(1+\frac{z}{r}+1-\frac{z}{r}\right)\\ &+\left(e^{-i\boldsymbol{k}\cdot\left(\boldsymbol{R}_j^b+\boldsymbol{R}_i^b\right)}+e^{-i\boldsymbol{k}\cdot\left(\boldsymbol{R}_j^b+\boldsymbol{R}_i^b\right)}+e^{i\boldsymbol{k}\cdot\left(\boldsymbol{R}_j^b+\boldsymbol{R}_i^b\right)}+e^{i\boldsymbol{k}\cdot\left(\boldsymbol{R}_j^b+\boldsymbol{R}_i^b\right)}\right)\frac{\sqrt{1-\frac{z^2}{r^2}}}{2}\Bigg]\\ &= \frac{1}{2}sgn(\hat{z}\cdot(\boldsymbol{a}_\alpha\times\boldsymbol{a}_\beta))t_2\left[2\cos\left(\boldsymbol{k}\cdot\left(\boldsymbol{R}_j^b-\boldsymbol{R}_i^b\right)\right)+\left(e^{-i\boldsymbol{k}\cdot\left(\boldsymbol{R}_j^b+\boldsymbol{R}_i^b\right)}+e^{i\boldsymbol{k}\cdot\left(\boldsymbol{R}_j^b+\boldsymbol{R}_i^b\right)}\right)\sqrt{1-\frac{z^2}{r^2}}\right]\\ &= sgn(\hat{z}\cdot(\boldsymbol{a}_\alpha\times\boldsymbol{a}_\beta))t_2\left[\cos\left(\boldsymbol{k}\cdot\left(\boldsymbol{R}_j^b-\boldsymbol{R}_i^b\right)\right)+\cos\left(\boldsymbol{k}\cdot\left(\boldsymbol{R}_j^b+\boldsymbol{R}_i^b\right)\right)\sqrt{1-\frac{z^2}{r^2}}\right].\end{aligned} \tag{6.41}$$

$\left\langle J_i^{ww}\right\rangle$ of the valley states

The valley state in the sub-space of two second-neighbor white atoms is,

$$\begin{aligned}\frac{1}{\sqrt{2}}\left(\left|u^{\boldsymbol{k}}\left(\boldsymbol{R}_i^w,\boldsymbol{R}_j^w\right)\right\rangle+\left|u^{-\boldsymbol{k}}\left(\boldsymbol{R}_i^w,\boldsymbol{R}_j^w\right)\right\rangle\right) &= \frac{1}{\sqrt{2}}\Bigg(e^{i\boldsymbol{k}\cdot\boldsymbol{R}_i^w}e^{i\phi}\sqrt{\frac{1-\frac{z}{r}}{2}}\left|W_i\right\rangle+e^{i\boldsymbol{k}\cdot\boldsymbol{R}_j^w}e^{i\phi}\sqrt{\frac{1-\frac{z}{r}}{2}}\left|W_j\right\rangle\\ &+e^{-i\boldsymbol{k}\cdot\boldsymbol{R}_i^w}e^{-i\phi}\sqrt{\frac{1+\frac{z}{r}}{2}}\left|W_i\right\rangle+e^{-i\boldsymbol{k}\cdot\boldsymbol{R}_j^w}e^{-i\phi}\sqrt{\frac{1+\frac{z}{r}}{2}}\left|W_j\right\rangle\Bigg).\end{aligned} \tag{6.42}$$

The current operator for the second-neighbor is,

$$\begin{aligned}\left\langle J\left(\boldsymbol{R}_i^w,\boldsymbol{R}_j^w\right)\right\rangle &= \frac{1}{2}\Bigg(\left\langle u^{\boldsymbol{k}}(R_i^w,R_j^w)|J^{ww}|u^{\boldsymbol{k}}(R_i^w,R_j^w)\right\rangle+\left\langle u^{-\boldsymbol{k}}(R_i^w,R_j^w)|J^{ww}|u^{-\boldsymbol{k}}(R_i^w,R_j^w)\right\rangle\\ &+\left\langle u^{\boldsymbol{k}}(R_i^w,R_j^w)|J^{ww}|u^{-\boldsymbol{k}}(R_i^w,R_j^w)\right\rangle+\left\langle u^{-\boldsymbol{k}}(R_i^w,R_j^w)|J^{ww}|u^{\boldsymbol{k}}(R_i^w,R_j^w)\right\rangle\Bigg).\end{aligned} \tag{6.43}$$

$$
\begin{aligned}
&\left\langle J\left(\boldsymbol{R}_i^w, \boldsymbol{R}_j^w\right)\right\rangle = -\frac{1}{2} sgn(\hat{z}\cdot(\boldsymbol{a}_\alpha\times\boldsymbol{a}_\beta)) t_2 \cos\left(\boldsymbol{k}\cdot\left(\boldsymbol{R}_j^b-\boldsymbol{R}_i^b\right)\right)\left(1-\frac{z}{r}\right)\\
&-\frac{1}{2}\begin{pmatrix} e^{i\boldsymbol{k}\cdot\boldsymbol{R}_i^w}e^{i\phi}\sqrt{\frac{1+\frac{z}{r}}{2}}, & e^{i\boldsymbol{k}\cdot\boldsymbol{R}_j^w}e^{i\phi}\sqrt{\frac{1+\frac{z}{r}}{2}}\end{pmatrix}\begin{pmatrix} 0 & sgn(\hat{z}\cdot(\boldsymbol{a}_\alpha\times\boldsymbol{a}_\beta))t_2\\ sgn(\hat{z}\cdot(\boldsymbol{a}_\alpha\times\boldsymbol{a}_\beta))t_2 & 0\end{pmatrix}\\
&\begin{pmatrix} e^{-i\boldsymbol{k}\cdot\boldsymbol{R}_i^w}e^{-i\phi}\sqrt{\frac{1+\frac{z}{r}}{2}}\\ e^{-i\boldsymbol{k}\cdot\boldsymbol{R}_j^w}e^{-i\phi}\sqrt{\frac{1+\frac{z}{r}}{2}}\end{pmatrix}\\
&-\frac{1}{2}\begin{pmatrix} e^{-i\boldsymbol{k}\cdot\boldsymbol{R}_i^w}e^{-i\phi}\sqrt{\frac{1-\frac{z}{r}}{2}}, & e^{-i\boldsymbol{k}\cdot\boldsymbol{R}_j^w}e^{-i\phi}\sqrt{\frac{1-\frac{z}{r}}{2}}\end{pmatrix}\begin{pmatrix} 0 & sgn(\hat{z}\cdot(\boldsymbol{a}_\alpha\times\boldsymbol{a}_\beta))t_2\\ sgn(\hat{z}\cdot(\boldsymbol{a}_\alpha\times\boldsymbol{a}_\beta))t_2 & 0\end{pmatrix}\\
&\begin{pmatrix} e^{-i\boldsymbol{k}\cdot\boldsymbol{R}_i^w}e^{-i\phi}\sqrt{\frac{1+\frac{z}{r}}{2}}\\ e^{-i\boldsymbol{k}\cdot\boldsymbol{R}_j^w}e^{-i\phi}\sqrt{\frac{1+\frac{z}{r}}{2}}\end{pmatrix}\\
&-\frac{1}{2}\begin{pmatrix} e^{i\boldsymbol{k}\cdot\boldsymbol{R}_i^w}e^{i\phi}\sqrt{\frac{1+\frac{z}{r}}{2}}, & e^{i\boldsymbol{k}\cdot\boldsymbol{R}_j^w}e^{i\phi}\sqrt{\frac{1+\frac{z}{r}}{2}}\end{pmatrix}\begin{pmatrix} 0 & sgn(\hat{z}\cdot(\boldsymbol{a}_\alpha\times\boldsymbol{a}_\beta))t_2\\ sgn(\hat{z}\cdot(\boldsymbol{a}_\alpha\times\boldsymbol{a}_\beta))t_2 & 0\end{pmatrix}\\
&\begin{pmatrix} e^{i\boldsymbol{k}\cdot\boldsymbol{R}_i^w}e^{i\phi}\sqrt{\frac{1-\frac{z}{r}}{2}}\\ e^{i\boldsymbol{k}\cdot\boldsymbol{R}_j^w}e^{i\phi}\sqrt{\frac{1-\frac{z}{r}}{2}}\end{pmatrix}\\
&=-\frac{1}{2} sgn(\hat{z}\cdot(\boldsymbol{a}_\alpha\times\boldsymbol{a}_\beta)) t_2 \cos\left(\boldsymbol{k}\cdot\left(\boldsymbol{R}_j^w-\boldsymbol{R}_i^w\right)\right)\left(1-\frac{z}{r}\right)\\
&-\frac{1}{2}\begin{pmatrix} e^{i\boldsymbol{k}\cdot\boldsymbol{R}_i^w}e^{i\phi}\sqrt{\frac{1+\frac{z}{r}}{2}}, & e^{i\boldsymbol{k}\cdot\boldsymbol{R}_j^w}e^{i\phi}\sqrt{\frac{1-\frac{z}{r}}{2}}\end{pmatrix}\begin{pmatrix} sgn(\hat{z}\cdot(\boldsymbol{a}_\alpha\times\boldsymbol{a}_\beta))t_2 e^{-i\boldsymbol{k}\cdot\boldsymbol{R}_j^w}e^{-i\phi}\sqrt{\frac{1+\frac{z}{r}}{2}}\\ sgn(\hat{z}\cdot(\boldsymbol{a}_\alpha\times\boldsymbol{a}_\beta))t_2 e^{-i\boldsymbol{k}\cdot\boldsymbol{R}_i^w}e^{-i\phi}\sqrt{\frac{1+\frac{z}{r}}{2}}\end{pmatrix}\\
&-\frac{1}{2}\begin{pmatrix} e^{-i\boldsymbol{k}\cdot\boldsymbol{R}_i^w}e^{-i\phi}\sqrt{\frac{1-\frac{z}{r}}{2}}, & e^{-i\boldsymbol{k}\cdot\boldsymbol{R}_j^w}e^{-i\phi}\sqrt{\frac{1-\frac{z}{r}}{2}}\end{pmatrix}\begin{pmatrix} sgn(\hat{z}\cdot(\boldsymbol{a}_\alpha\times\boldsymbol{a}_\beta))t_2 e^{-i\boldsymbol{k}\cdot\boldsymbol{R}_j^w}e^{-i\phi}\sqrt{\frac{1+\frac{z}{r}}{2}}\\ sgn(\hat{z}\cdot(\boldsymbol{a}_\alpha\times\boldsymbol{a}_\beta))t_2 e^{-i\boldsymbol{k}\cdot\boldsymbol{R}_i^w}e^{-i\phi}\sqrt{\frac{1+\frac{z}{r}}{2}}\end{pmatrix}\\
&-\frac{1}{2}\begin{pmatrix} e^{i\boldsymbol{k}\cdot\boldsymbol{R}_i^w}e^{i\phi}\sqrt{\frac{1+\frac{z}{r}}{2}}, & e^{i\boldsymbol{k}\cdot\boldsymbol{R}_j^w}e^{i\phi}\sqrt{\frac{1+\frac{z}{r}}{2}}\end{pmatrix}\begin{pmatrix} sgn(\hat{z}\cdot(\boldsymbol{a}_\alpha\times\boldsymbol{a}_\beta))t_2 e^{i\boldsymbol{k}\cdot\boldsymbol{R}_j^w}e^{i\phi}\sqrt{\frac{1-\frac{z}{r}}{2}}\\ sgn(\hat{z}\cdot(\boldsymbol{a}_\alpha\times\boldsymbol{a}_\beta))t_2 e^{i\boldsymbol{k}\cdot\boldsymbol{R}_i^b}e^{i\phi}\sqrt{\frac{1-\frac{z}{r}}{2}}\end{pmatrix}\\
&=-\frac{1}{2} sgn(\hat{z}\cdot(\boldsymbol{a}_\alpha\times\boldsymbol{a}_\beta)) t_2\Bigg[\cos\left(\boldsymbol{k}\cdot\left(\boldsymbol{R}_j^w-\boldsymbol{R}_i^w\right)\right)\left(1-\frac{z}{r}\right)+\cos\left(\boldsymbol{k}\cdot\left(\boldsymbol{R}_j^w-\boldsymbol{R}_i^w\right)\right)\left(1+\frac{z}{r}\right)\\
&+\left(e^{-i\boldsymbol{k}\cdot\left(\boldsymbol{R}_j^w+\boldsymbol{R}_i^w\right)}e^{-2i\phi}+e^{-i\boldsymbol{k}\cdot\left(\boldsymbol{R}_j^w+\boldsymbol{R}_i^w\right)}e^{-2i\phi}+e^{i\boldsymbol{k}\cdot\left(\boldsymbol{R}_j^w+\boldsymbol{R}_i^w\right)}e^{2i\phi}+e^{i\boldsymbol{k}\cdot\left(\boldsymbol{R}_j^w+\boldsymbol{R}_i^w\right)}e^{2i\phi}\right)\frac{\sqrt{1-\frac{z^2}{r^2}}}{2}\Bigg]\\
&=-\frac{1}{2} sgn(\hat{z}\cdot(\boldsymbol{a}_\alpha\times\boldsymbol{a}_\beta)) t_2\Bigg[\cos\left(\boldsymbol{k}\cdot\left(\boldsymbol{R}_j^w-\boldsymbol{R}_i^w\right)\right)\left(1-\frac{z}{r}+1+\frac{z}{r}\right)\\
&+\left(e^{-i\boldsymbol{k}\cdot\left(\boldsymbol{R}_j^w+\boldsymbol{R}_i^w\right)}e^{-2i\phi}+e^{-i\boldsymbol{k}\cdot\left(\boldsymbol{R}_j^w+\boldsymbol{R}_i^w\right)}e^{-2i\phi}+e^{i\boldsymbol{k}\cdot\left(\boldsymbol{R}_j^w+\boldsymbol{R}_i^w\right)}e^{2i\phi}+e^{i\boldsymbol{k}\cdot\left(\boldsymbol{R}_j^w+\boldsymbol{R}_i^w\right)}e^{2i\phi}\right)\frac{\sqrt{1-\frac{z^2}{r^2}}}{2}\Bigg]\\
&=-\frac{1}{2} sgn(\hat{z}\cdot(\boldsymbol{a}_\alpha\times\boldsymbol{a}_\beta)) t_2\left[2\cos\left(\boldsymbol{k}\cdot\left(\boldsymbol{R}_j^w-\boldsymbol{R}_i^w\right)\right)+\left(e^{-i\boldsymbol{k}\cdot\left(\boldsymbol{R}_j^w+\boldsymbol{R}_i^w\right)}e^{-2i\phi}+e^{i\boldsymbol{k}\cdot\left(\boldsymbol{R}_j^w+\boldsymbol{R}_i^w\right)}e^{2i\phi}\right)\sqrt{1-\frac{z^2}{r^2}}\right].
\end{aligned}
\tag{6.44}
$$

$$\left\langle J\left(\boldsymbol{R}_i^w, \boldsymbol{R}_j^w\right)\right\rangle = -sgn(\hat{z}\cdot(\boldsymbol{a}_\alpha \times \boldsymbol{a}_\beta))t_2\left[\cos\left(\boldsymbol{k}\cdot\left(\boldsymbol{R}_j^w - \boldsymbol{R}_i^w\right)\right) + \cos\left(\boldsymbol{k}\cdot\left(\boldsymbol{R}_j^w + \boldsymbol{R}_i^w\right) + 2\phi\right)\sqrt{1-\frac{z^2}{r^2}}\right]. \tag{6.45}$$

The above expression can be further simplified by replacing the parameters such as $\boldsymbol{k}, -\boldsymbol{k}$ by their actual values. We will not show any further simplification but we will discuss how these current look. We plot a lattice with sufficient number of atoms which helps us visualize the current pattern.

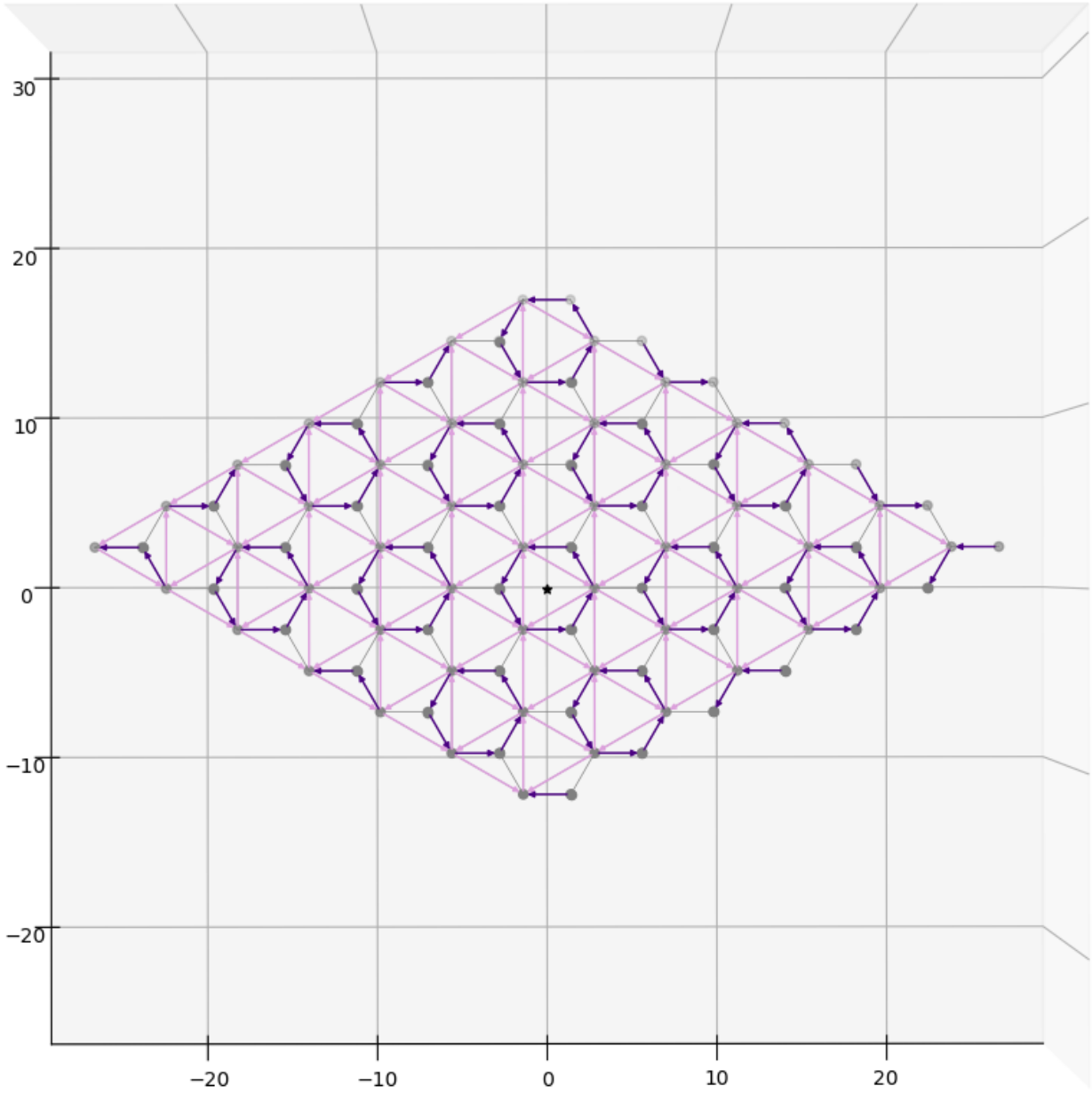

Figure 6.7: Plot of $\langle J_i^{bw}\rangle$ and $\langle J_i^{bb}\rangle$ currents on a large lattice in the R_xR_y plane. The nearest neighbor current flow of valley states is circular and occurring with some periodicity. This is indicated by the dark purple vectors. The second neighbor currents in a lighter purple (in reality an order of magnitude smaller than $\langle J^{bw}\rangle$ are plotted large here) also seem to move in a circular pattern. Here, for reasons of clarity, three out of six second neighbor currents are shown.

In Fig.6.7, the navy blue arrows are the currents produced by the valley states. The dominating nearest neighbor currents flow counter-clockwise in a circular direction along the honeycomb. This pattern creates a superlattice formed out of three hexagons whose lattice vectors are $\boldsymbol{S}_1 = 3a_0(1, \sqrt{3})$ and $\boldsymbol{S}_2 = 3a_0(1, -\sqrt{3})$. The occurrence of this superlattice is a direct result of the phase difference between the orbital states of the wavefunctions. The second neighbor current $\langle J_i^{bb} \rangle$ are small but also flow in loops. In Fig.6.7, the dark vectors are plotted to have the same length as the distance $|\boldsymbol{R}_j^w - \boldsymbol{R}_i^b|$ and the pink vectors are plotted to have the same length as $|\boldsymbol{R}_j^b - \boldsymbol{R}_i^b|$ to emphasize the flow of the current. In reality, $\langle J_i^{bb} \rangle$ is an order of magnitude smaller than $\langle J_i^{bw} \rangle$ and $|\langle J_i^{ww} \rangle| = |\langle J_i^{bb} \rangle|$. Here we show only three out of six $\langle J_i^{bb} \rangle$ for reasons of clarity. The star indicates the origin $\boldsymbol{R} = (R_x, R_y) = (0, 0)$.

The time-reversed states will have current flows in the opposite directions as shown by Eq.6.46. In addition to the symmetry relations from section.6.3, we see $\left\langle J(-\boldsymbol{R}_i^b, -\boldsymbol{R}_j^w) \right\rangle = -\left\langle J(\boldsymbol{R}_i^b, \boldsymbol{R}_j^w) \right\rangle$ for the valley states at the Dirac point in Fig.6.7. This gives the following relation between the states that are related by time-reversal and parity,

$$\left\langle (PT)^\dagger J(\boldsymbol{R}_i^b, \boldsymbol{R}_j^w) PT \right\rangle = -\left\langle P^\dagger J(\boldsymbol{R}_i^b, \boldsymbol{R}_j^w) P \right\rangle = \left\langle J(-\boldsymbol{R}_i^b, -\boldsymbol{R}_j^w) \right\rangle = -\left\langle J(\boldsymbol{R}_i^b, \boldsymbol{R}_j^w) \right\rangle . \tag{6.46}$$

For a quantum dot state, the envelope function will break this regularity by modulating both the dark and the light vectors of Fig.6.7 by the corresponding $F(\boldsymbol{R}_i^b)$ and $F(\boldsymbol{R}_i^w)$ factor. Nonetheless, we may conclude that $\langle J_i^{bw} \rangle$ are the predominant contributions to the orbital part of the g-factor. Smaller corrections will show up with the $\langle J_i^{bb} \rangle$ and $\langle J_i^{ww} \rangle$ contributions. Though smaller by many orders of magnitude they may be significant.

Bibliography

[1] C. Kittel. *Quantum Theory of Solids*. Wiley, 1987. ISBN 9780471624127. URL https://books.google.de/books?id=BcGwQgAACAAJ.

[2] Titus Sandu. Optical matrix elements in tight-binding models with overlap. *Physical Review B*, 72(12), September 2005. ISSN 1550-235X. doi: 10.1103/physrevb.72.125105. URL http://dx.doi.org/10.1103/PhysRevB.72.125105.

[3] Prof. C. Anastasiou. Quantum mechanics ii. URL https://edu.itp.phys.ethz.ch/fs09/qm2/EX08.pdf. exercise 8.1.

[4] Harold U. Baranger, David P. DiVincenzo, Rodolfo A. Jalabert, and A. Douglas Stone. Classical and quantum ballistic-transport anomalies in microjunctions. *Phys. Rev. B*, 44:10637–10675, Nov 1991. doi: 10.1103/PhysRevB.44.10637. URL https://link.aps.org/doi/10.1103/PhysRevB.44.10637.

[5] Timothy B Boykin, Mathieu Luisier, and Gerhard Klimeck. Current density and continuity in discretized models. *European Journal of Physics*, 31(5):1077, jul 2010. doi: 10.1088/0143-0807/31/5/010. URL https://dx.doi.org/10.1088/0143-0807/31/5/010.

[6] The transport problem: Currents from quantum mechanics, 2015. URL https://courses.cit.cornell.edu/mse5470/2015_ece4070_mse5470_primernotes_transport_dj.pdf. page 45, eq.5.25.

[7] D. J. Chadi and Marvin L. Cohen. Tight-binding calculations of the valence bands of diamond and zincblende crystals. *Physica Status Solidi B-basic Solid State Physics*, 68:405–419, 1975. URL https://api.semanticscholar.org/CorpusID:12495144.

[8] Natália Menezes, Van Sergio Alves, EC Marino, Leonardo Nascimento, Leandro O Nascimento, and C Morais Smith. Spin g-factor due to electronic interactions in graphene. *Physical Review B*, 95(24):245138, 2017. URL https://onlinelibrary.wiley.com/doi/full/10.1002/pssb.202300395.

[9] AV Volkov, AA Shylau, and IV Zozoulenko. Interaction-induced enhancement of g factor in graphene. *Physical Review B—Condensed Matter and Materials Physics*, 86(15):155440, 2012. URL https://journals.aps.org/prb/abstract/10.1103/PhysRevB.86.155440.

[10] Pengke Li and Ian Appelbaum. Excitons without effective mass: Biased bilayer graphene. *Phys. Rev. B*, 99:035429, Jan 2019. doi: 10.1103/PhysRevB.99.035429. URL https://link.aps.org/doi/10.1103/PhysRevB.99.035429.

[11] A. Kurzmann, M. Eich, H. Overweg, M. Mangold, F. Herman, P. Rickhaus, R. Pisoni, Y. Lee, R. Garreis, C. Tong, K. Watanabe, T. Taniguchi, K. Ensslin, and T. Ihn. Excited states in bilayer

graphene quantum dots. *Phys. Rev. Lett.*, 123:026803, Jul 2019. doi: 10.1103/PhysRevLett.123.026803. URL https://link.aps.org/doi/10.1103/PhysRevLett.123.026803.

[12] Cheng Shen, Yanbang Chu, QuanSheng Wu, Na Li, Shuopei Wang, Yanchong Zhao, Jian Tang, Jieying Liu, Jinpeng Tian, Kenji Watanabe, et al. Correlated states in twisted double bilayer graphene. *Nature Physics*, 16(5):520–525, 2020. URL https://www.nature.com/articles/s41567-020-0825-9.

[13] C. L. Kane and E. J. Mele. Quantum spin hall effect in graphene. *Phys. Rev. Lett.*, 95:226801, Nov 2005. doi: 10.1103/PhysRevLett.95.226801. URL https://link.aps.org/doi/10.1103/PhysRevLett.95.226801.

Conclusion

As established thus far, the g-factor is an important quantity when it comes to dealing with spin states in external fields. We have shown a theoretical framework that established the deviation of the g-factor from the vacuum value of 2. This deviation can be extremely large (negative) and results from orbital contributions that have origins in the spin-orbit interaction. This involves looking at the momentum matrix elements of the Kramers states of the valence and conduction bands. We also show that the intra-atomic must not be neglected in the orbital contributions.

For semiconductor valence and conduction band states, we illustrate the topology of the g-factors in $\boldsymbol{k}$-space which include surface of maximal spin-orbit interactions. Such surfaces are guaranteed by symmetry. Using group theoretical approaches, we generalize our results to the point groups O, O_h, T, T_d, T_h. These can be easily applied to a large class of materials. We also show that the surfaces where $det(g_{tot}) < 0$ alter in topology as $det(g_{tot}) > 0$. These surfaces are by no means trivial to analyze.

To investigate the source of orbital contributions to the g-factor, we consider an alternative formalism by defining the current flows along bonds connecting two neighboring atoms on a lattice. The conduction band states have a homogeneous current flow throughout the crystal following its symmetries. In the case of silicon, we understand that current flows do occur at the band minimum and it is the net current that has no contribution overall. Graphene is an interesting material as it has different types of orbital contributions coming from its nearest and its second neighbor interactions. The contributions of the second neighbor interactions can be controlled by the t_2 parameter. We see loops of currents emerging across the lattice of Graphene with a periodicity of a superlattice for the first neighbor currents. This is very different from the case of silicon and could make the $det(g)$ surfaces more complex.

The connection between symmetries and the g-factor opens up new ways to exploit both of them in the context of quantum information. We may take this further and apply the envelope approximation to theoretically determine the g-factors of spin states at positions where it is experimentally difficult to probe them. We believe this work might pave the way to further investigation on this topic, in close connection with existing and new experimental platforms.